DESIGN OF A SHAPE MEMORY ALLOY COIL ACTUATED ROBOTIC FINGER WITH COMPLIANT JOINT ANTAGONISTS

ARVIN TANGESTANIAN

A THESIS SUBMITTED TO THE FACULTY OF GRADUATE STUDIES
IN PARTIAL FULFILMENT OF THE REQUIREMENTS
FOR THE DEGREE OF

MASTER OF SCIENCE

GRADUATE PROGRAM IN EARTH AND SPACE SCIENCE
YORK UNIVERSITY
TORONTO, ONTARIO
SEPTEMBER 2022

Abstract

This thesis investigates the development of a compliant 3D-printed robotic finger actuated by a shape memory alloy (SMA) coil actuator. In this work the design, manufacturing, and characterization of the compliant finger mechanism, the SMA coil actuators, and an integrated prototype using both analytical and experimental methods is presented. The compliant finger mechanism is designed via a static wrench analysis to close at a specific force and 3D-printed using commercial filament. The SMA actuator is designed using a static two-state model, based on the required actuation stroke between discrete force-displacement coordinates. SMA coils are manufactured and characterized to obtain the actuator profiles for the SMA in martensite and austenite phases. The experimental profiles for the actuator and structure are used to predict the equilibrium points between the two hysteresis curves. A dynamics model of the complete system is derived and used to predict integrated behaviour. The final robotic finger, with an SMA coil actuating the compliant finger mechanism is tested, and the experimental results show the actuation stroke and bias distance closely match the predictions from the analysis.

This thesis is dedicated to my loving family and friends

Acknowledgements

I would like to sincerely thank my supervisor Dr. Ryan Orszulik, for all of his guidance, wisdom, and support. I am thankful to have had such a knowledgeable mentor throughout my graduate school experience. I also want to thank my lab mates Ariel Tabak, Rafael Toledo, Margarita Khramova, and Morgan O'Dea for all of their friendship and assistance. In particular I am grateful to Rita for all of her help with my early experiments, and to Rafael for his input during our coffee breaks. Thank you to Sarah for listening to my incoherent ramblings, for lifting my spirits when the going was tough, and for celebrating my victories with me.

Last but not least I would like to acknowledge the late night coffee's that truly gave me the energy and confidence needed to finish my research.

Table of Contents

List of Tables

List of Figures

1 Introduction

A shape memory alloy (SMA) is a smart material that demonstrates shape memory behaviour. Through its reversible phase change process between two crystal states, martensite and austenite, an SMA can recover from severe deformations to restore a trained shape. The restoration force generated and the macro-scale shape changes during this process allow for SMAs to be used as actuators. SMAs have some advantages over traditional actuators such as DC motors due to their high energy density, light weight, small volume, large force, and linear motion. This makes them attractive for use in some robotics applications, such as in biologically inspired mechanisms.

SMA actuators are analogous to muscles in organisms. Similar to an organic muscle contracting with an electrical stimulus, an SMA wire can contract from the Joule heating of an electric current. With their high energy density, short SMAs can produce relatively large forces, similar to the energy dense muscles of small animals and insects. This allows for biologically inspired robotics designs where the SMAs

can act as artificial muscles. However SMA actuators have some limitations, one of which is the requirement for an antagonist force. The shape memory effect requires an antagonist to deform the SMA from it's memorized shape. This antagonist force is usually achieved by pairing the SMA with a bias spring, however this requires additional mounting and assembly. This does present an opportunity to design a mechanism so that the stiffness of the structure itself acts as an antagonist to the SMA actuator.

The antagonist force can be achieved by designing the robotic structure as a compliant mechanism. Compliant mechanisms are structures where joint mobility is derived from local flexible regions. These flexible joints have some advantages over rigid body joints, such as reduced friction and ease of manufacture. Compliant joints also reduce assembly requirements, enabling monolithic design. The bending of flexible joints is similar to the bending of torsional springs, where the deflection of the flexible member is opposed by the elastic energy stored within the joint.

Pairing SMA actuators with compliant antagonists enables a smart structure design, where the joint stiffness integrated with the one way shape memory effect enables two-way, repeatable motion. However, SMAs and some flexure joints will exhibit hysteresis profiles in the force-displacement domain, so the actuator and structure must be carefully designed to match each other for effective actuation and biasing.

As an application of this concept, this thesis discusses the design of a robotic finger for grasping tasks that utilizes shape memory alloy coils as artificial muscles, and compliant joints as antagonists. The SMA coil acts as an artificial muscle, contracting and pulling on the finger as it is activated. The flexible joints will bias the SMA, resisting the motion and resetting the finger after actuation. The entire structure is designed to be 3D-printable, enabling rapid prototyping, reducing manufacturing time, and simplifying assembly. This work presents the engineering design process for the finger structure and flexible joint geometry, the design, fabrication, and characterization of SMA coil actuators, the dynamical model of the integrated finger, and the results of the final integrated mechanism.

There are many potential applications for an SMA-compliant gripper such as this finger. The use of compliant joints eliminates the need for external antagonist assemblies, reducing actuator mass and volume, which lends itself well to small scale robotics. The force-displacement trade off of the SMA enables for soft gripping, where the grip force from the SMA and structural design is matched to the resistance of its environment. This has industrial applications such as in agriculture and medicine which require delicate handling tasks. Other soft robotics often use pneumatic actuation systems, which are bulky and expensive, whereas SMA actuators are much smaller, lightweight, and energy dense. The finger design also contributes to the development of SMA actuated prosthetics, which are trending

towards underactuated, simplified designs.

1.1 Shape Memory Alloys

Shape memory alloys are a unique class of smart materials that demonstrate two characteristic properties, super-elasticity (SE) and the shape memory effect (SME) [3, 9–19]. Super-elasticity refers to the materials ability to recover from extreme deformations while in the austenite phase, through the transformation to stress-induced martensite. The shape memory effect is the phenomenon where the material will re-shape itself after deformation to return to a pre-configured configuration. The SME is triggered by external stimuli such as heat. Both the SME and SE are derived from the material's reversible phase transition process between the martensite and austenite phases of the alloy [3, 11–13, 15–17].

The high temperature austenite phase has a cubic crystal lattice structure, whereas the low temperature martensite phase exhibits a tetragonal, or monoclinic structure [3, 11–13, 15–17, 19]. Martensitic SMA can be in either a twinned, or de-twinned state (referring to the symmetry of the crystal lattice) [3, 11–13, 15–17], which can be seen in Figure 1.1 for a reference illustration of the crystal lattice structure at different phases. When below the austenite start temperature (T_{A_s}), the SMA is in it's martensite phase and the crystal lattice shifts to form a twinned pattern [3, 11, 15, 18]. When in this twinned martensite state, applied stress will

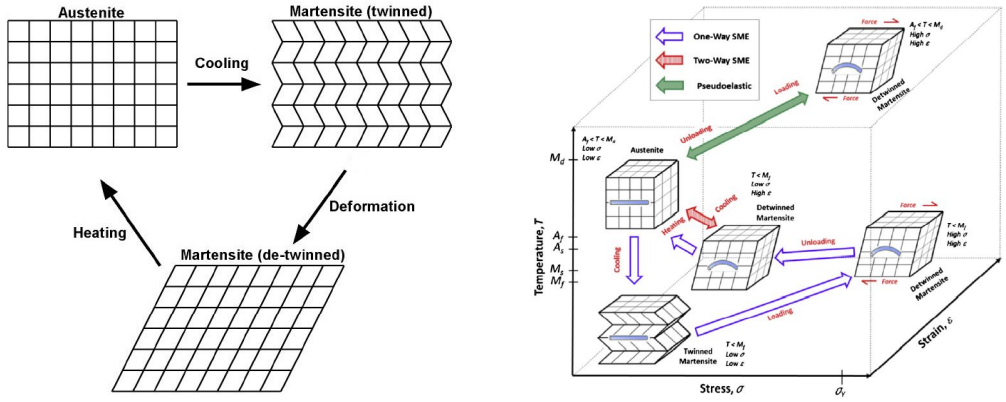

(a) Depiction of the crystal lattice of SMA structure for each phase

(b) Three dimensional representation of the lattice structure

Fig. 1.1 Shape memory alloy crystal lattices throughout the SME cycle [3]

shift the lattice to the de-twinned shape. This stress also creates macro scale displacements in the materials configuration. The shape memory effect occurs when de-twinned martensite SMA transitions to austenite. During this phase transformation, the crystal lattice reorients itself from the tetragonal lattice to the cubic pattern. The changing crystal lattice also causes the macroscopic structure of the SMA to re-shape itself to its remembered state [3, 11–18].

In addition to heating and cooling, the transition process between the two phases can also be induced by stressing the material when already above the austenite finish temperature (T_{A_f}) [3, 11, 15–18]. The application of sufficient stress (sometimes called the critical stress [18]) to an austenitic SMA creates stress-induced marten-

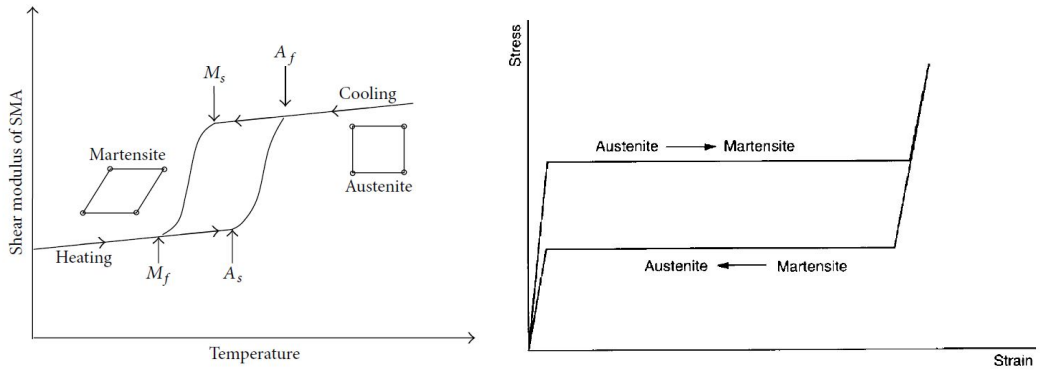

(a) Temperature domain [18] (b) Stress-strain domain [14]

Fig. 1.2 Hysteresis curves for SMA phase changes in different domains

site, and upon unloading, the reverse transformation occurs and the material transitions back to austenite [3, 11, 15, 18]. Straining of the stress-induced martensite will lead to elastic loading, which the material will fully recover from upon transition to austenite [3, 15, 16, 18]. This ability to recover from large induced strain is the SE property. There is a three dimensional relationship between stress, strain, and temperature that influences the crystal lattice, as illustrated in Figure 1.1(b).

The cycle between martensite and austenite can also be seen as a two dimensional relationship, either between temperature and state, or between stress and strain. This planar view reveals a cyclical history-dependent state profile, similar to hysteresis behaviour. The hysteresis curves for an SMA are commonly depicted with illustrations such as Figure 1.2. The temperature hysteresis curve in Figure 1.2(a) indicates the temperature boundaries for the phase transition. T_{A_s} indicates

the temperature where martensite to austenite phase transition starts, T_{A_f} is the austenite finish temperature, meaning that the material is fully austenite above this temperature. T_{M_s} indicates the start of austenite to martensite phase transition, and T_{M_f} is the temperature below which the material is fully martensite.

Although solid-phase transformations and shape memory behaviour was recognized as early as 1932 [20], it was not until the discovery[1] of nitinol by William J. Buehler at the U.S Naval Ordnance Laboratory in 1959 that SMAs became practical to produce and commercially available to researchers and inventors [3, 21, 22]. Buehler continued research into the behaviour of this material alongside the scientist Frederick E. Wang [21]. The material, named nitinol (for Nickel Titanium Naval Ordnance Laboratory) was studied over the subsequent period, and the alloy was tested for suitability in various applications. Wang believed that the material could be used as an energy source, operating as a solid-state heat engine, converting thermal energy to mechanical or electrical energy [23–26]. Many different nitinol engine prototypes were designed, commonly using a temperature gradient across a nitinol belt loop to drive a gear system. These nitinol heat engines worked by warming a segment of the belt under hot water so that it would warm to austenite transition and attempt to straighten itself out, this produced a torque and drove the belt loop [21, 24]. The U. S. Energy Department spent some years investigating

[1] Accidentally discovered by playing with NiTi and a cigar lighter during a project management meeting [21]

nitinol-engine power sources, seeking cost-effective and energy efficient alternatives to nuclear or photo-voltaic power [27]. Although some studies suggested that nitinol engines could be more cost effective per kilowatt than nuclear power [27] the research ultimately did not lead to any use for nitinol engines in the power sector.

The potential of shape memory alloys was recognized and adapted to many diverse applications in the 1970s and 1980s. Nitinol found success in medical applications, such as assisting in mending bone fractures, SMA stents to reinforce arteries and veins, and blood-clot filters [21, 22, 28]. It was also employed in orthodontics, nitinol being used as the expanding wire and mounts in braces to adjust teeth position [21, 28]. For engineering applications, nitinol was put to very effective use as a self-sealing coupler in hydraulic fluid lines for F-14 jets [21, 22]. Several other alloy systems besides nickel-titanium were identified that share shape memory properties with nitinol, significantly copper-zinc-aluminum, gold-cadmium, and some others [3, 19, 21, 22]. In the 1990s, advances were made in the field of shape memory to identify shape memory polymers [3, 17, 19, 29, 30]. Overall, shape memory alloys saw employment in a variety of engineering applications, across many fields. Today they are common in medical applications [28], aerospace [19], automotive, consumer goods, and even civil structures [31]. SMA actuators are especially prominent in novel mechanism designs [32–35] and in robotics applications.

1.1.1 SMA Actuators

The shape memory effect is especially attractive in engineering contexts because it can be exploited as a means for the SMA to act as an actuator. Shape memory alloy actuators can be in different configurations, but linear actuators are typically in the form of wires, or wires that have been coiled to form a helical spring. The operating principle is based on the SME. A simple linear SMA actuator will be trained, through the manufacturing process, to have a certain length or extension in the austenite phase. Deforming the SMA when in martensite phase, such as by elongating a coil along its directional axis, will change the lattice to detwinned martensite. At this point, inducing a phase transformation will cause the actuator to return to its original position through the SME. For wire or coil configurations this creates a true linear actuator, without the need for a conversion from rotational to linear motion.

Using the shape memory effect for actuation requires an external force to deform the SMA from its memorized shape and to de-twin the martensite. This external force is referred to as an antagonist force, or bias. For repeated actuation cycles, the SMA must be repeatedly biased. Typically SMA actuators are paired with an antagonist mechanism. These antagonist mechanisms are arranged such that they constantly pull against the SMA, deforming it from its configured shape. The

antagonist force is overcome during actuation, where the SMA restores itself to its memorized shape, but upon cooling the antagonist will again deform the SMA and allow for the SME to be triggered once again. The bias function is commonly performed by pairing the SMA with a passive mechanical resistance, such as a spring. Instead of external mechanisms, there are examples in the literature of pairing two or more SMAs in an antagonistic configuration, whereby the actuation of one SMA will provide the bias force to deform another [3, 13, 36]. There is also a unique class of shape memory alloys which do not require an antagonist. These utilize the two way shape memory effect (TWSME), in which the alloy exhibits a reversible shape change process during the phase transitions, at the cost of reduced actuation stroke and force [3, 17, 18, 37].

SMA actuators are most commonly found as wires, or as coils. There are examples in the literature of alternative SMA forms, such as sheets or ribbons (SMA lengths with thin, rectangular cross sections) [3, 15, 30], but the overwhelming majority of applications use wires or coils. SMA wire will typically be employed as a unidirectional actuator, extending and contracting along the axis of the straight wire, experiencing deformation in their tensile mode [11]. Wires can have an actuation stroke from 6-8% of their original length [3, 11]. SMA coils are essentially just wires that have been formed into a helical spring pattern, typically with memorized shapes in the contracted state. SMA coils experience deformation in the

shear mode [11], as the local wire segments along the coil are strained. SMA coils have a much greater stroke than wires, and can extend more than 50-100% of their length [11, 36]. It has also been shown that linear SMA actuators oriented in different directions can be superposed, changing the force direction (similar to vector addition) and allowing for more complex actuation motion [38].

Commercially available shape memory alloys are commonly in NiTi, CuAlNi or other alloy mixtures. It is common for researchers to manufacture their own coils from commercially available SMA wire. Manufacturing a SMA coil involves winding the wire in some way to create a helical coil shape. The actuator characteristics of the coil are related to geometric parameters, such as the pitch angle, coil diameter, wire diameter, and number of loops [2, 11, 14, 36, 39, 40]. In order to have the SMA memorize this new coil shape, they are heat treated or annealed. The characteristics of an SMA are dependent on its alloy composition and manufacturing, but they can be further affected by the annealing process. For SMA coils, the annealing profile can alter material properties such as the shear modulus [36].

The shape memory effect requires an external trigger to initiate phase transformation. This is usually achieved by heating the material above T_{A_f}. The most common method of achieving this is through resistive heating [3, 41]. Resistive heating (also known as Joule heating) is the process where a material conducting electric current begins to heat due to the power dissipated by its electrical resis-

tance. SMAs typically have low resistances (nitinol wire can have resistances around 100 $\mu\Omega/cm$ [1]) so they require a higher current to generate the power required for heating. The resistance of the SMA will fluctuate during the phase change process, due to the changing crystal lattice and local transition behaviour [42, 43]. Therefore it is more common to control Joule heating through an applied current, rather than an applied voltage. Although Joule heating can be achieved with a direct current, some research has suggested that pulse width modulation activation leads to a more uniform and steady heating of SMA wires [6, 41, 44], however this is not widely accepted.

Since actuator motion is coupled with the SME, the actuation frequency of an SMA is limited by the duration of the required heating and cooling periods. Heating is generally achieved through the use of Joule heating, so the heating time will depend on the applied current and the materials electrical resistance. Cooling can be achieved through a variety of methods, but in most robotic applications the SMA is left to cool from passive convective heat transfer to the environment. The cooling period depends on the current load, the ambient conditions, how long the SMA was conducting, and the thickness of the wire. Surveys have shown that the fastest actuation period (complete heating-cooling cycle) for a nitinol type actuator is about 2-3 seconds [3]. However, the cooling process can also be expedited through design of the coil geometry to increase exposed surface area, aiding in heat transfer.

Some researchers have shown that designing actuators with a large coil index and pitch angle will reduce cooling times [11, 45]. However designing coils with these parameters may also reduce the maximum force output or stroke [2, 11].

A shape memory alloy based actuator displays several key advantages over traditional actuators. First, they are very lightweight, and do not occupy much volume. This makes them attractive for applications like small scale robotics, where bigger and bulkier actuators (such as a DC motor) hinder performance. Additionally, they have a fantastic energy density. Nitinol has been measured to have work density outputs from 1.2 kJ/kg [3, 36] to 4 kJ/kg [18], or in terms of volume 10 J/cm^3 [3], and it is also known that SMAs can generate forces up to 150 times greater than hydraulics and 400 times greater than magnetic actuators (for the same actuator volume) [46, 47]. Of course, this will depend on many factors, including the specific manufacturing and design of the SMA in question, but overall SMA actuators exhibit incredible energy density compared to traditional actuators of the same size. SMAs are also robust materials, that can endure high stresses, extreme elastic deformations, are resistant to chemical erosion [21, 27], and have high wear resistance [3,17,18,21,27]. Secondary benefits, such as how their self-driving nature can greatly simplify mechanical design, and their silent actuation, give them additional advantages in niche design applications, such as in biologically inspired robotics.

This is not to say, however, that shape memory alloys are without their prob-

lems. The behaviour of this material is history-dependent, and effort must be made to account for hysteresis in control system design for SMAs. This, combined with the non-linear response of SMAs, has presented a unique dynamic modelling challenge. There are established SMA dynamic models, such as Tanaka [9], and Rogers and Liang [10] which present constitutive equations from a thermo-mechanical perspective. Key features of these dynamic models include the representation of the phase transition state through state variables. Liang and Tanaka have been the foundation for numerous other models [16, 17, 29, 37, 48–56]. In engineering applications, researchers are often more concerned with how to adapt these models for designing SMA actuators with desirable characteristics [2, 12–15, 30, 36, 57–60]. For robotics applications, SMA actuator design usually focuses on the required actuation stroke, force outputs, and heat transfer.

Another challenge with designing SMA actuators is parameter uncertainty. In addition to the inherent assumptions and simplifications in the thermo-mechanical models, these models often rely on the use of SMA material properties. These material properties are dependant on the alloying process, manufacturing, actuator design, and annealing. Some of these properties must be experimentally determined for a given sample, through the use of tensile tests or other means. However SMAs also display strain rate dependant behaviour [43, 61] and will respond differently between a quasi-static tensile test and a dynamic activation. Another point of con-

sideration is the state history of a given sample. Rigorous testing on an individual SMA, such as blocked force austenite tests, run the risk of partially resetting the austenite memorized shape configuration.

There are some SMA models which propose for feedback control using state variables such as displacement [13,62], temperature [12,14,15], or output force [13,62] . Typically, SMAs are controlled via micro controllers or other circuits that will pulse the material with high currents (using Joule heating to induce the transformation), and a variety of external sensors will monitor those aforementioned parameters for feedback. More recent research, such as a novel hybrid thermomechanical model proposed by Cortez-Vega et al. [12] simplify the feedback monitoring and also claim very accurate motion and force approximations. Other recent research proposes a novel method of measuring actuator displacement via the inductance of an SMA coil [11, 39]. Although these and other techniques are not yet widespread, the literature in general shows a trend towards streamlining SMA actuator design and control for engineering applications.

1.1.2 SMA in Bio-Inspired Robotics

SMA actuators lend themselves well to applications where scalability, low mass, and small size are prioritized [63,64]. Thus it is of no surprise that SMAs have been used to great advantage in biologically inspired robotics, particularly in designs

based off of small animals or insects. In this application, the SMA is utilized as an artificial muscle (AM) [63, 64]. In operation, a contracting and extending SMA wire or coil is analogous to biological muscles. With this parallel, the anatomy or biological designs of creatures can be replicated with SMA as the substitute for muscle fibres (hence, artificial muscle). Small scale SMA robots are sometimes grouped with a field called "soft robotics", in which smart materials and compliant structures are utilized in the design to mimic biological features. This section will briefly discuss some examples of using SMA as AM in bio-mimetic robotic designs.

A small robot inspired by caterpillar locomotion was developed by Trimmer et al. [65] that utilized SMA coils for the motion of body segments. This group identified the potential for SMA actuators to be used analagous to the muscle fibres in a caterpillars body, for twisting and crawling motion. They bonded nitinol springs to inner body walls, for extension of body segments, and relied on the elasticity of the flexible wall material to bias the individual SMA coils.

A similar crawling robot was developed by Koh and Cho [66], using SMA coils for a soft inchworm robot. This design also used SMAs for discrete actuation of body segments, allowing for crawling locomotion. The SMA coils are paired antagonistically through a four-bar linkage, such that the activation of one side of the body will bias the SMAs on the other side. This design also utilized flexible material for motion, with compliant joint design in the linkage.

A small jumping robot was developed by Noh et al. [38] using SMA springs to mimic the catapult-like jumping motion of a flea. This group used an array of three SMA springs with a bar mechanism to replicate the musculature of a flea leg. This used an antagonistic pairing between the SMAs for the bias mechanism. This design highlights the advantages of SMAs being lightweight and energy dense, like organic muscle. The same research group also developed an insect inspired water jumping robot [67], using nitinol ribbons. This design also took advantage of the superelasticity of SMA, enabling repeated bending without permanent deformation.

1.1.3 SMA Actuated Robotic Hands

The potential for SMA to act as artificial muscles has also been recognized in robotic hand design. The Hitachi Hand was demonstrated in 1984 to use a hybrid of SMA wires and springs to power three anthropomorphic fingers and a thumb [6, 68, 69]. This design claimed to have a load capacity of 4.4 foot-pounds, with 0.02 mm diameter wires, however the hand was not very dexterous and was limited to one DOF grasping capability [6, 69]. The Hitachi model served as a convincing proof of concept, and since its debut there have been many more SMA designs by researchers globally.

There are a variety of intended functions for SMA hands, such as for industrial applications, research demonstrations, or for potential prosthetics uses. These de-

signs commonly utilize underactuation for grasping, which has been recognized as an effective approach for anthropomorphic hand designs [70, 71]. In terms of prosthetics, SMA actuated designs are attractive as potential alternatives for common actuators in bionic hands, such as DC motors [72, 73]. This is mostly due to SMAs low mass, noiseless operation, and biocompatability. Hand designs commonly employ SMA actuators as artificial muscles for actuating individual finger segments, or entire digits. This section will discuss key features of some of these designs, sampling developments over the past few decades. A summary is presented in Table 1.1.

The Rutgers hand [69] identified SMA actuators as attractive alternatives to DC motors in prosthetic hands. This design has bundles of SMA wires operating in parallel to act as AM. It uses internal routing channels to connect SMA actuators to joints. Each finger has four SMA wire bundles, two to the distal joint and two to the proximal joint. Each bundle consists of two distinct SMA wires in an antagonist pair, operating so that one may be used for flexion, and one for recovery. The actuator bundles produce a maximum fingertip force of 6.67 N. The Rutgers hand was a mechanical proof of concept design, meant to validate the then-novel concept of rapid prototyping, and as such it does not discuss problems such as thermal isolation, actuation speed, control, or sensor implementation.

The Price hand [4] (pictured in Figure 1.3) is a three finger design with 9 DOF.

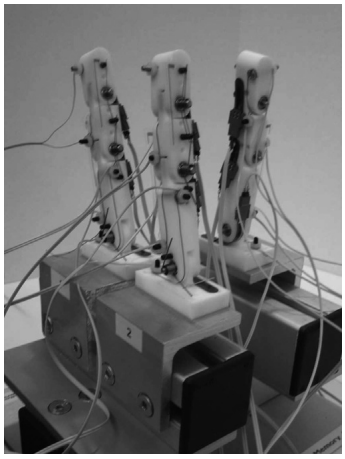

Fig. 1.3 Price SMA hand [4]

It utilizes Flexinol brand nitinol wire from Dynalloy with 0.015" diameter. The wire was annealed at 600°C for 2 hours, in order to relieve residual stress. The wire actuators are mounted to the joints with a 5% pre-strain, such that thermal activation triggers finger contraction. It uses torsion springs on the joints as a biasing force against the SMA. The design of this hand places emphasis on the control systems aspect, and this paper presents a kinematic model that treats the three fingers as serial manipulators working cooperatively. As the design sought to establish better finger position control, it finds that a sigmoidal control signal minimizes overshoot error. This group concluded that steady state error could be reduced by introducing a PWM offset component into the control algorithm.

Bundhoo [44] sought to use SMA actuators as AM to reproduce the full range of motion of a human finger, as well as to develop an accurate kinematic model.

It used off the shelf SMA wire actuators attached to transmission cables, called tendons, for its actuation mechanism. Like the Rutgers hand, it uses a differential pair of actuators for each finger segment, one for extension and another for flexion. The actuators are biased with a spring mounted in series with the SMA. This experimental setup had all of the SMA actuators mounted separately from the finger on an optical table, whilst the extending tendons linked to the finger joints. A single finger was tested, employing a PWM-PD voltage control method. The closed loop tests shows variable current draw as the SMAs activate, with a maximum current of about 1.5 A. There was a slow 20-30 second cooling period for the joints to return to their un-actuated positions. The paper identifies this long cooling time to be exacerbated by the design choice to tightly pack the SMA wires between plastic plates. The paper also comments that this actuator mounting setup resulted in high friction, and in some cases the plastic plates melted and restrained the actuators.

Farias et al. [5] developed an anthropomorphic hand with four fingers and one thumb. It used Flexinol NiTi SMA coils, which were wound onto screws and annealed at 600°C for five minutes, and rapidly cooled with water. The mechanical design of the hand featured magnetic latching mechanisms, such that the SMA coils are not required to exert force to maintain a position. The SMAs were mounted in antagonistic bias pairs, for finger flexion and extension. This design required the use of six individual SMA coils per finger, each with discrete electrical connections

Fig. 1.4 Farias SMA hand [5]

to the controller, as seen in Figure 1.4. This group demonstrated hand grasping for light objects, but further experimental results concerning actuation force and cooling time remain to be seen.

The Andrianesis design [6] sought to develop a functional hand with fast actuation time, suitable for grasping objects. It employed 0.25 mm diameter Flexinol SMA wires in a pulley mechanism, attached to a finger. The SMA coils are routed through a heat sink block to aid in cooling, tied to tendons which connect to the finger. A helical spring was used for biasing, as shown in Figure 1.5. It used voltage PWM activation of the SMAs, as with the Bundhoo design. The actuation time for

Table 1.1 Performance metrics of SMA robotic fingers surveyed

Researchers	SMA Type	Alloy	SMA Force	Activation	Actuation Period
Price et al. [4]	wire	NiTi	10 N	2 A for 10s	x
Bundhoo [44]	coil	NiTi	10 N	1.4 A for 10s	30s
Andrianesis et al. [6]	wire	NiTi	x	x	3s
Kaplanoglu et al. [74]	coil	NiTi	17N	0.8 A for 1.5s	x
Lee et al. [75]	wire	NiTi	2 N	x	24s
Silva et al. [76]	wire	NiTi	10 N	0.9 A for 20s	40s
Deng et al. [8]	coil	NiTi	1.11 N	0.5 A for 4-6 s	8 s

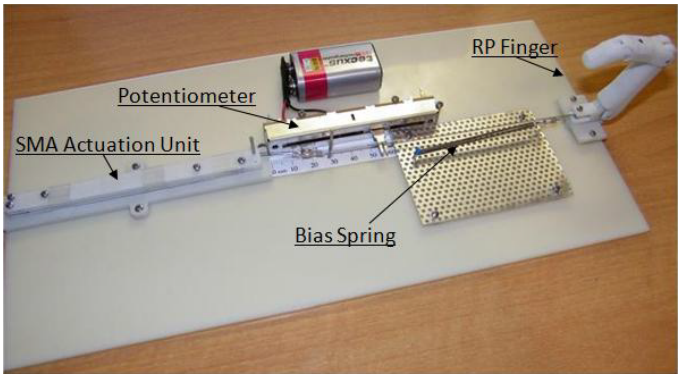

Fig. 1.5 Andrianesis SMA finger test bed [6]

a finger to fully extend from rest is 0.9 seconds, and a 2.5 second period for cooling. The design featured an under actuated approach, whereby the limited number of actuators control a larger number of DOF. For control, it was found that on-off type actuation is more suitable than proportional control. However in this work grasping experimental results remain to be seen.

Kaplanoglu [74] used SMA coils mounted to tendons with an under actuated design. The hand model called for a hybrid utilization of SMA actuators in some

fingers, and a DC motor for the thumb. This design used an antagonist pair of SMA wires, one for flexion and one for extension, each connected to the distal joint. The design uses compliant joints, but had embedded torsional springs for each joint for SMA biasing, in addition to the antagonist pair. The little and ring fingers in this model were found to have a maximum fingertip force of 11 N and 17 N.

The Lee model [75] designed a finger with SMA wires attached to the end points of each link via a tendon pulley mechanism. The tendons were routed through hollow channels in the finger. This design had individual SMA coils for each link (three per finger). The range of motion for each link was limited by contact with physical stoppers. The primary goal of this hand was to achieve grasping motion and force, without consideration to position control or other such dynamic modelling concerns. The antagonist force is achieved with a bias spring connected to each of the joints by a tendon, to pull the finger back into the neutral pose after grasping actuation. The full hand is controlled by an array of coils and tendons for each of the fingers, controlled with DC voltage pulses.

The Silva finger design [76] used SMA wires that were trained to use the two way shape memory effect. This finger uses 'H alloy' commercial NiTi wire from Memory-Metalle inc. The wires were annealed for 20 minutes at 450°C before recieving TWSME training. TWSME behaviour was induced by subjecting the NiTi wire to hundreds of loaded thermal cycles. Although SMA with the TWSME

typically display less actuation strain, the lengths of these wires were quite long ranging from 680 mm to 1065 mm. The SMA wires were attached to the finger links through a pulley and tendon mechanism. Silva et al. reported a better range of motion and stabilization time than De Laurentis and Bundhoo [44, 69] through the use of computer vision feedback, but identifies issues such as high temperature before suitable for use in prosthetics.

The Soriano-Heras hand [7] took some different design approaches. Where the previous research models discussed all attempted to reproduce the serial revolute chain of a human finger, the Soriano-Heras hand uses a multi-bar linkage with a gear mechanism. This design only uses two digits, achieving object grasping between the index finger and thumb (as in Figure 1.6(a)). The actuation mechanism uses Flexinol NiTi wire fixed to a stainless steel beam, shown in Figure 1.6(b). When the SMA is activated, its contraction causes the free end of steel beam to flex, and rise from the base of the mount. A nylon wire is attached from the beam via a pulley to a gear system inside the palm of the hand, which causes the index finger to rotate and approach the thumb. Biasing is achieved through a torsional spring attached to the gear mechanism, in addition to the elasticity of the flexible beam. The hand successfully gripped various objects, however there is no data on power efficiency, actuation time, or grip strength.

Simone et al. [77] present an SMA finger design that uses a bundle of SMA

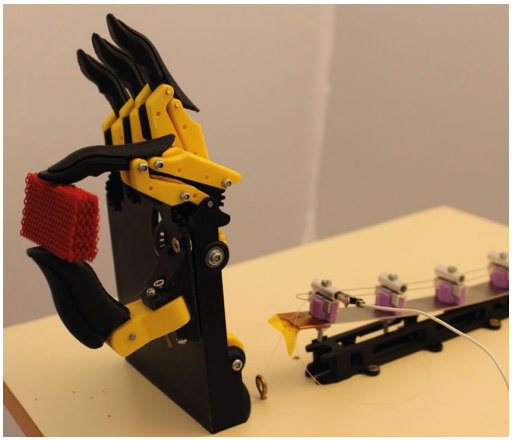

(a) SMA hand gripping an object

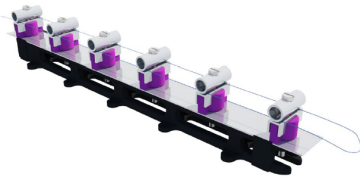

(b) SMA wire actuator mounted to steel beam external from hand

Fig. 1.6 Soriano-Heras SMA finger mechanism [7]

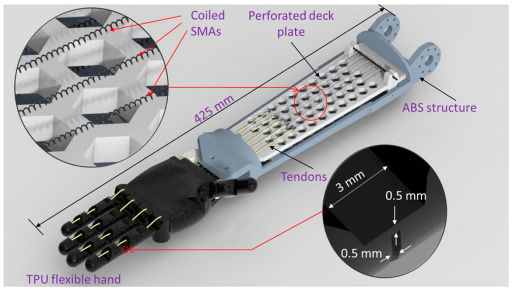

(a) SMA hand assembly

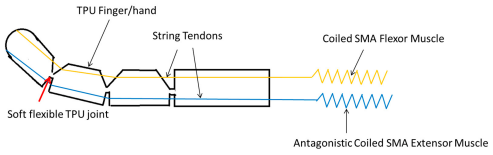

(b) Compliant finger with antagonist SMA pair

Fig. 1.7 Deng and Yang SMA hand [8]

wires. The bias force is provided by a spring mounted in series with the SMA actuator. This research presents the kinematics of the mechanism, and derives dynamic model for the SMAs heating and thermal activation based on the Müller-Achenbach-Seelecke model [51]. With a complete dynamic model for the prototype, they validate the model by comparing experimental trajectories to the simulation,

with some agreement. This group noted that parameter identification is necessary for accurate SMA modelling, and observed that the thermomechanical behaviour for an SMA will also be influenced by the structure it actuates.

Deng and Yonas [8] recently developed a SMA coil actuated hand which utilizes flexible joints. This group identified the advantages of compliant mechanism design for fabrication, including ease of assembly, and rapid prototyping. The hand uses Flexinol 0.2 mm diameter nitinol wire, wound around piano wire into very thin coils. The coils are annealed at 350°C for 45 minutes. The bias force is achieved through an antagonistic pair of SMAs, using one for flexion and one for extension, as shown in Figure 1.7(b). Although this is one of the first examples of a fully compliant SMA hand design in the literature, this work focuses on the manufacturing rather than the engineering design process for the compliant mechanism. This model also shows limited grasping mobility, and uses very long SMA coils for the required actuation strokes.

There have been some developments in SMA actuated robotic hand design over the years, but there are still areas for improvement. Some earlier designs used an overactuated approach, with at least one or more SMAs per finger segment [4, 5, 44]. However it has been shown that underactuation is adequate for grasping [6–8, 70–72, 74, 75, 77]. Some designs use SMA wires with a pulley tendon system, however it has been shown that using SMA coils are more effective than wires due

to their longer actuation strokes. An underactuated approach with a coil-tendon system simplifies design, reduces assembly requirements, and reduces control effort.

It is common in the literature to see researchers manufacture their own coils and proceed to discuss performance, without covering their design methodology for the coils. SMA coil design is included more regularly in the biological robotics literature [36, 66], but isn't as prevalent with SMA hand research. This is a large research gap, where some researchers treat the SMA as an off-the-shelf actuator without designing the coil to meet their functional needs.

This survey also showed that it is quite common for these designs to use antagonist SMA pairs for the flexion and extension motions, however it has been shown that a torsional spring on the finger joints is just as effective. From the insect robot literature, it has also been shown that SMAs can be biased using the stiffness of the mechanism itself, with compliant mechanism design. Although there are some examples of designing an SMA hand with compliant joints [8], there is a potential to use the joints themselves as bias mechanisms, reducing the need for external springs or additional SMAs.

1.2 Compliant Mechanisms

Compliant mechanisms are mechanical systems which exploit the reduced stiffness of structural regions for selective motion in a mechanism [78]. These flex-

ible regions are referred to as compliant joints or flexure joints. Flexure joints have some advantages over rigid body joints, such as reduced friction, no backlash, monolithic design, ease of manufacture, and they are easy to miniaturize [78–81]. This makes flexures preferable to conventional joints in certain use cases, and they have seen a wide range of applications. Flexure-based design is standard in microelectromechanical systems (MEMS), where assembly of micro-scale components would otherwise be very expensive and difficult [80, 81] and compliant joints are also commonplace in soft robotics [81, 82].

1.2.1 Flexure Design

Flexure hinges commonly appear in different morphologies, such as beam, circular notch, elliptical notch, and crossed beam [78–80, 83]. The joint geometry of each flexure hinge type affects its stiffness characteristics and mobility. Thus, flexure hinge design consists of reconciling the geometry parameters with the desired stiffness and range of motion for the joint. There are different design methodologies and equations such as in the form of tabulated parameters based on joint type [80, 83], as well as analyses based on compliance or Castigliano's displacement theorem [79, 84–88].

The pseudo-rigid body model (PRBM) is a method for analyzing compliant mechanisms. The PRBM models the deflection of the flexible members by rep-

resenting them as rigid bodies with equivalent characteristics [78, 79, 89]. Rather than representing the structure as having rigid links connected by flexible members, the PRBM representation reduces each compliant joint to a single pin joint with a torsional spring constant corresponding to the force-deflection relationship of the compliant segment.

The key factors in employing a PRBM representation are the location and stiffness of the pseudo-rigid joint. The position of the pseudo-rigid pin joint along the flexible member is referred to as the characteristic radius [78, 79, 90]. The torsional stiffness of the pseudo-rigid joint is typically equivalent to the bending stiffness of the flexible member.

1.2.2 Compliant Fingers

In recent years there has been a growing interest in designing robotic fingers with flexure hinge joints. Lotti and Vassura [91] put forward the possibility of designing a compliant finger using a kinetostatic analysis of the PRBM. Mutlu et al. [92] investigated the design and performance of 3D-printed elliptical notch flexure hinges for a compliant finger with an anthropomorphic range of motion. Multiple works have also investigated designing compliant finger grasping mechanisms for industrial [93] and prosthetic [94–97] applications, in general without consideration of the actuator forces required. Garcia et al. [98] presented the design for a cross

beam flexure for transmission of grasping force in a compliant hand mechanism. Zhou et al. [99] designed a servo actuated compliant prosthetic hand with embedded sensors and anthropomorphic hand gesture capabilities. Although there has been great interest in designing compliant hands with anthropomorphic characteristics, previous works have not demonstrated how to integrate joint design with actuator force requirements.

Compliant joints can also be exploited to act as passive bias mechanisms for one-way linear actuators, such as shape memory alloy coils. As flexible members, the joints will store elastic potential energy as they are deformed. When the actuation is complete, this elastic potential energy may be used to restore the mechanism to its neutral position. Previous works have indicated in discussion that this property could be used to extend fingers after grasping [95, 96, 99]. The challenge in this case is in designing the joints so that they have the appropriate stiffness for a given linear actuator force-displacement profile. Joints that are too compliant may not be able to bias against the full actuator motion, meaning that they will not be able to restore the mechanism to its initial pose. If the compliant joints are too stiff, then the mechanisms range of motion will be limited and it may not be able to achieve a desired pose.

1.3 Research Objectives and Contributions

This research focuses on the development of a 3D printable SMA actuated robotic finger with compliant joints. Pairing an SMA actuator with a compliant antagonist allows for simplified mechanism design, reducing the need for external antagonist assemblies. The integration of shape memory alloys with the elasticity of the structure itself shall combine two separate one-way processes to produce two-way repeatable motion. Compliant design also enables additive manufacturing techniques, where the structure can be 3D-printed as a monolithic body. Furthermore, SMA coils can achieve longer actuation strokes than wires. This reduces the need for tendon-pulley assemblies or other mechanical amplifiers, which have been seen in other robotic hands using SMA wires.

In addition, this work presents the compliant joint design process from an analytical basis. Although there are other compliant grippers and hands in the literature, there is a lack of documentation showing how to integrate flexure geometry with the intended actuator profiles. In the same vein, the literature for SMA robotic hands does not demonstrate how one may design a coil actuator appropriate for the mechanism. Hence, this thesis will present the engineering design process for designing and matching a SMA coil actuator for a 3D-printed compliant antagonist structure.

With these research gaps in mind, the objectives of this research are as follows:

1. Design a compliant finger mechanism to bias a given actuator at a specified final pose

2. Design, fabricate, and characterize SMA coils for given actuation requirements

3. Investigate the effectiveness of pairing designed SMA actuators with a designed compliant antagonist structure for a robotic finger

1.4 Organization

This thesis is organized into six main parts. Chapter 2 presents the design and validation of the compliant finger mechanism. This begins with a static analysis of the mechanism with a pseudo-rigid body model, discusses the connection to flexure geometry, and validates the design through finite element analyses and force-displacement experiments. Chapter 3 discusses the design, manufacturing, and characterization of the SMA coil actuators. This covers the theory and application of a static two-state actuator model from the literature, and presents the in-house manufacturing and testing of SMA actuators. Chapter 4 derives the dynamics of the finger, defines the activation characteristics of the SMA coil, and integrates them to model the dynamics of the full system. Chapter 5 presents the results of integrated prototype experiments. Finally, the conclusion in Chapter 6 summarizes

the findings of this research and discusses directions for future work.

2 Quasi Static Model and Finger Design

This chapter discusses the design process for the compliant finger structure. Modelled after a human index finger, the design will be a serial chain of three rigid segments connected by three compliant revolute joints. The kinematics of the mechanism are derived, and a static wrench analysis is used to determine the required flexure joint design for a given actuator and desired grip position. This method is then applied to design and 3D print finger mechanisms for different actuator loads, which are then experimentally verified for joint performance.

2.1 Pseudo-Rigid Body Model

The design of the finger employs rectangular beam flexures for the compliant joints. These beam flexures are chosen to have a uniform thickness across their length, with no filleted corners. In general, beam flexure designs will be much simpler to compute than those with more complicated geometry, and can be incorporated into the early design phases of a compliant mechanism. These simple

flexures can then act as a baseline for further design iterations, where the geometry can be modified for more desirable performance. In [90] an analysis for the large nonlinear deflection of beams was proposed based on the PRBM. A similar pseudo rigid representation will be used for the static analysis of this mechanism. The PRBM used here will use a characteristic radius of 0.5. This will reduce the flexible joints to pin joints, such that the position of the pseudo-rigid revolute joint will be located halfway along the flexure beam length. With these assumptions, the design equations for the mechanism can now be derived.

2.2 Kinematics of a 3R Planar Mechanism

The kinematics of a mechanism describes the motion of the mechanism without consideration of the forces and torques that cause the motion. The kinematic description is therefore a geometric one. This section will describe the forward and inverse kinematics for a serial planar chain with three revolute joints (3R). Kinematic derivations for mechanisms such as a 3R chain can be found in standard robotics textbooks [100, 101].

A robot manipulator is composed of a set of links, connected by joints. A serial manipulator with n joints will have $n + 1$ links. The joints are numbered from 1 to n, and the links are numbered from 0 to n, starting from the base. By this convention, joint i connects link $i - 1$ to link i. Each joint J_i has an associated

joint variable, denoted as θ_i. In the case of revolute joints, the joint variable is an angle of rotation. For a 3R mechanism, there will be three angular joint variables, denoted as

$$\theta = \begin{bmatrix} \theta_1 \\ \theta_2 \\ \theta_3 \end{bmatrix} \tag{2.1}$$

The position and orientation of the end effector is denoted as

$$Q = \begin{bmatrix} Q_x \\ Q_y \\ \Theta \end{bmatrix} \tag{2.2}$$

where (Q_x, Q_y) denotes the cartesian coordinates of the end effector with respect to the base frame (as defined below), and Θ denotes the angle between the end effector axis and the base frame axis x_o.

To perform the kinematic analysis, a coordinate frame is attached to each link. In particular the frame $o_i x_i y_i z_y$ is attached to link i. The origin of the frame o_i is located at the base of link i, coincident with J_i. The frame $o_0 x_0 y_0 z_0$ is attached to the robot base, this is referred to as the base frame or inertial frame. The position of any frame $o_i x_i y_i z_y$ can be expressed as the result of a transformation from $o_{i-1} x_{i-1} y_{i-1} z_{i-1}$. Generally, the transformation between frames can be described by a homogeneous transformation matrix, but for a serial revolute chain the use of simple rotation matrices is adequate.

2.2.1 Forward Kinematics

The forward kinematics of a manipulator is concerned with determining the position of the end effector through knowledge of the joint variables. For a 3R planar manipulator, this is achieved by performing consecutive transformations from the inertial frame along the serial chain to the end effector. Each joint is a revolute joint, with one degree of freedom allowing for rotation about a single axis. The revolute joint variable θ_i is the angular displacement from the neutral axis of link $i-1$ to the neutral axis of link i, as depicted in Figure 2.1. The transformation from frame $o_{i-1}x_{i-1}y_{i-1}z_{i-1}$ to $o_ix_iy_iz_i$ is described with the rotation matrix

$$R_i = \begin{bmatrix} \cos(\theta_i) & -\sin(\theta_i) \\ \sin(\theta_i) & \cos(\theta_i) \end{bmatrix} \tag{2.3}$$

For a link of length L, the cartesian coordinates of the next joint in the chain can be described by;

$$\begin{bmatrix} x_i \\ y_i \end{bmatrix} = L_i \begin{bmatrix} \cos(\theta_i) & -\sin(\theta_i) \\ \sin(\theta_i) & \cos(\theta_i) \end{bmatrix} \begin{bmatrix} x_{i-1} \\ y_{i-1} \end{bmatrix} \tag{2.4}$$

The position (Q_x, Q_y) and orientation Θ of the end effector with respect to the base frame are found by chaining together rotations along each link in series

$$\begin{aligned} Q_x &= L_1\cos(\theta_1) + L_2\cos(\theta_1+\theta_2) + L_3\cos(\theta_1+\theta_2+\theta_3) \\ Q_y &= L_1\sin(\theta_1) + L_2\sin(\theta_1+\theta_2) + L_3\sin(\theta_1+\theta_2+\theta_3) \\ \Theta &= \theta_1+\theta_2+\theta_3 \end{aligned} \tag{2.5}$$

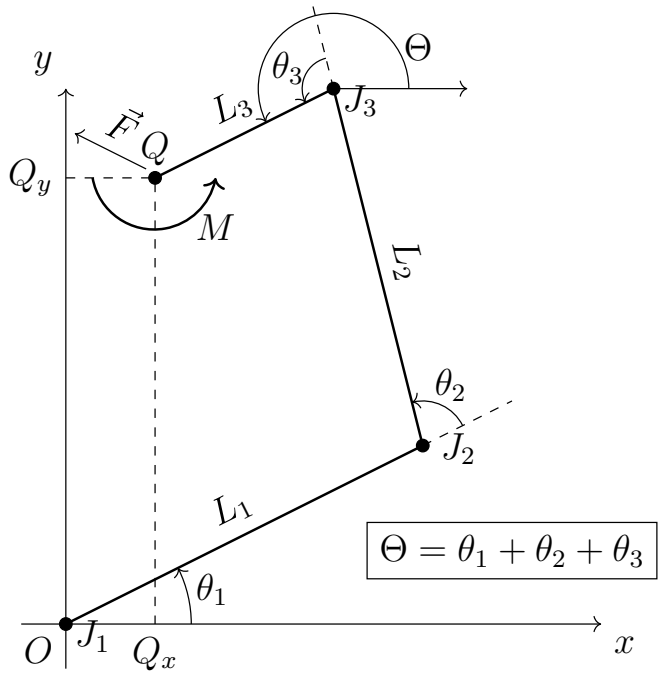

Fig. 2.1 A 3R planar manipulator with static wrench load

2.2.2 Inverse Kinematics

The problem of inverse kinematics is to find the joint variables in terms of the end effectors pose. This is generally more difficult than the forward kinematics problem. The equations are nonlinear and complex, and so the analysis will be more involved than the previous discussion. This section will rely heavily on the use of the trigonometric functions sine and cosine, so we introduce the shorthand notation, where c_{123} denotes $\cos(\theta_1 + \theta_2 + \theta_3)$, s_{123} denotes $\sin(\theta_1 + \theta_2 + \theta_3)$ and similar notation is employed for other subscripts on c and s.

To begin, the solution is derived by examining equation (2.5).The orientation

of the third link is known with respect to the base as $\theta_1 + \theta_2 + \theta_3$ is equal to the orientation of the end effector, Θ. Thus the variable θ_3 can be eliminated from equation (2.5).

$$\begin{aligned} Q_x &= L_1 \cos(\theta_1) + L_2 \cos(\theta_1 + \theta_2) + L_3 \cos(\Theta) \\ Q_y &= L_1 \sin(\theta_1) + L_2 \sin(\theta_1 + \theta_2) + L_3 \sin(\Theta) \end{aligned} \tag{2.6}$$

The position of joint 3 will be denoted as P, with components P_x and P_y. Assuming rigid links for this analysis, since P and Q are separated by a distance equal to the length of link 3 at an angle of Θ, the position of point P is determined through simple trigonometry. Point P is also found from the forward kinematic analysis.

$$\begin{aligned} P_x = L_1 \cos(\theta_1) + L_2 \cos(\theta_1 + \theta_2) &= Q_x - L_3 \cos(\Theta) \\ P_y = L_1 \sin(\theta_1) + L_2 \sin(\theta_1 + \theta_2) &= Q_y - L_3 \sin(\Theta) \end{aligned} \tag{2.7}$$

The components of equation (2.7) are squared and summed to simplify and reduce the system

$$\begin{aligned} P_x^2 &= L_1^2 c_1^2 + 2L_1 L_2 c_1 c_{12} + L_2^2 c_{12}^2 \\ P_y^2 &= L_1^2 s_1^2 + 2L_1 L_2 s_1 s_{12} + L_2^2 s_{12}^2 \end{aligned} \tag{2.8}$$

$$P_x^2 + P_y^2 = L_1^2(c_1^2 + s_1^2) + L_2^2(c_{12}^2 + s_{12}^2) + 2L_1 L_2(c_1 c_{12} + s_1 s_{12}) \tag{2.9}$$

$$P_x^2 + P_y^2 = L_1^2 + L_2^2 + 2L_1 L_2(c_1 c_{12} + s_1 s_{12}) \tag{2.10}$$

At this point, the trigonometric angle-sum identity is introduced to further simplify

$$\cos(\alpha)\cos(\beta) + \sin(\alpha)\sin(\beta) = \cos(\alpha - \beta) \tag{2.11}$$

$$\cos(\theta_1 + \theta_2)\cos(\theta_1) + \sin(\theta_1 + \theta_2)\sin(\theta_1) = \cos(\theta_1 + \theta_2 - \theta_1) = \cos(\theta_2) \tag{2.12}$$

Substituting equation (2.11) into equation (2.10) yields

$$P_x^2 + P_y^2 = L_1^2 + L_2^2 + 2L_1L_2c_2 \tag{2.13}$$

The system has been reducedto a single equation with only one unknown. This can be easily rearranged to isolate for the $\cos(\theta_2)$ term, and solve for the angle.

$$\theta_2^{(a,b)} = \cos^{-1}\left(\frac{P_x^2 + P_y^2 - L_1^2 - L_2^2}{2L_1L_2}\right) \tag{2.14}$$

The revolute joint variable for joint 2 has been obtained, however it is important to keep in mind that there are two solutions for this angle. The same pose of a 3R mechanism can be achieved with a set of two manipulator configurations. These two solutions will have different joint variables for joints 1 and 2, denoted as $\theta_1^{(a,b)}$ and $\theta_2^{(a,b)}$. The primary solution to (2.14) would be in quadrants 1 or 2 of the cartesian plane, while the secondary solution is the angle within quadrants 3 or 4. Since cosine is an even function, the two solutions are related with

$$\theta_2^b = -\theta_2^a \tag{2.15}$$

These correspond to the so-called "elbow up" and "elbow down" configurations for the manipulator. This analysis shall always asssume the elbow up solution.

Now, the identity in equation (2.11) may be employed into equation (2.7) to

obtain an expression for $\theta_1^{(a,b)}$ in terms of $\theta_2^{(a,b)}$.

$$\begin{aligned} P_x &= L_1 c_1 + L_2 c_{12} \\ P_y &= L_1 s_1 + L_2 s_{12} \end{aligned} \tag{2.16}$$

$$\begin{aligned} P_x &= L_1 c_1 + L_2 (c_1 c_2 - s_1 s_2) \\ P_y &= L_1 s_1 + L_2 (s_1 c_2 + c_1 s_2) \end{aligned} \tag{2.17}$$

$$\begin{aligned} P_x &= (L_1 + L_2 c_2)\cos(\theta_1) - (L_2 s_2)\sin(\theta_1) \\ P_y &= (L_2 s_2)\cos(\theta_1) + (L_1 + L_2 c_2)\sin(\theta_1) \end{aligned} \tag{2.18}$$

Equation (2.18) is of the following form

$$\begin{aligned} E &= A\cos(\alpha) - B\sin(\alpha) \\ F &= B\cos(\alpha) + A\sin(\alpha) \end{aligned} \tag{2.19}$$

Which is solved by a single angle α that satisfies both equations. These simultaneous equations can be re-arranged and solved as follows

$$\cos(\alpha) = \frac{AE + BF}{A^2 + B^2} \tag{2.20}$$

$$\sin(\alpha) = \frac{AF - BE}{A^2 + B^2}$$

$$\tan(\alpha) = \frac{AF - BE}{AE + BF} \tag{2.21}$$

Substituting the corresponding terms in equation (2.18) for A, B, E and F, equation (2.21) is used to solve for $\theta_1^{(a,b)}$.

$$\tan(\theta_1^{(a,b)}) = \frac{(L_1 + L_2\cos(\theta_2^{(a,b)}))P_y - (L_2\sin(\theta_2^{(a,b)}))P_x}{(L_1 + L_2\cos(\theta_2^{(a,b)}))P_x + (L_2\sin(\theta_2^{(a,b)}))P_y} \tag{2.22}$$

Where the $\tan(\theta_1^a)$ solution corresponds to a θ_1^a input on the right hand side, and vice versa. Finally, with the joint 1 and 2 variable sets, the final joint variable is found from the definition of the end effector orientation Θ in equation (2.5)

$$\theta_3^{(a,b)} = \Theta - \theta_1^{(a,b)} - \theta_2^{(a,b)} \tag{2.23}$$

Equation (2.23) concludes the inverse kinematic analysis of a 3R mechanism. This presents a complete description of the mechanism configuration, from the basis of end effector position and orientation.

2.2.3 Instantaneous Kinematics

An expression for the end effector velocity components can be found from the time derivative of the forward kinematics in equation (2.5). This is assuming that all joint angles are changing in time, with unchanging link lengths.

$$\begin{aligned} \dot{Q}_x &= -L_1\dot{\theta}_1 s_1 - L_2(\dot{\theta}_1 + \dot{\theta}_2)s_{12} - L_3(\dot{\theta}_1 + \dot{\theta}_2 + \dot{\theta}_3)s_{123} \\ \dot{Q}_y &= L_1\dot{\theta}_1 c_1 + L_2(\dot{\theta}_1 + \dot{\theta}_2)c_{12} + L_3(\dot{\theta}_1 + \dot{\theta}_2 + \dot{\theta}_3)c_{123} \\ \dot{\Theta} &= \dot{\theta}_1 + \dot{\theta}_2 + \dot{\theta}_3 \end{aligned} \tag{2.24}$$

The expressions in equation (2.24) can be expressed in matrix form as

$$\begin{bmatrix} \dot{Q}_x \\ \dot{Q}_y \\ \dot{\Theta} \end{bmatrix} = \begin{bmatrix} -L_1 s_1 - L_2 s_{12} - L_3 s_{123} & -L_2 s_{12} - L_3 s_{123} & -L_3 s_{123} \\ L_1 c_1 + L_2 c_{12} + L_3 c_{123} & L_2 c_{12} + L_3 c_{123} & L_3 c_{123} \\ 1 & 1 & 1 \end{bmatrix} \begin{bmatrix} \dot{\theta}_1 \\ \dot{\theta}_2 \\ \dot{\theta}_3 \end{bmatrix} \tag{2.25}$$

The 3×3 matrix in equation (2.25) is the Jacobian, where the elements of the matrix express the partial rates of change of the end effector coordinates with respect to

the joint parameters.

$$J = \frac{\delta Q}{\delta \theta} = \begin{bmatrix} -L_1 s_1 - L_2 s_{12} - L_3 s_{123} & -L_2 s_{12} - L_3 s_{123} & -L_3 s_{123} \\ L_1 c_1 + L_2 c_{12} + L_3 c_{123} & L_2 c_{12} + L_3 c_{123} & L_3 c_{123} \\ 1 & 1 & 1 \end{bmatrix} \tag{2.26}$$

The column vector in equation (2.25) represents the joint angular velocities

$$\dot{\theta} = \begin{bmatrix} \dot{\theta}_1 \\ \dot{\theta}_2 \\ \dot{\theta}_3 \end{bmatrix} \tag{2.27}$$

As shown in equation (2.25), the product of the Jacobian and the joint angular velocities yields the end effector velocities. This relationship is put simply as

$$\dot{Q} = J\dot{\theta} \tag{2.28}$$

If the Jacobian matrix is non-singular, equation (2.28) can be re-written to obtain an expression for the joint velocities in terms of the end effector velocities.

$$\dot{\theta} = J^{-1}\dot{Q} \tag{2.29}$$

However, this is only true when the Jacobian is non-singular. The Jacobian may be singular if the determinant is equal to zero or if the matrix is non invertible. The conditions under which the Jacobian is singular should be examined. To begin, the determinant of the Jacobian matrix

$$\begin{aligned} |J| = {} & (-L_1 s_1 - L_2 s_{12} - L_3 s_{123})((L_2 c_{12} + L_3 c_{123}) \cdot 1 - (L_3 c_{123}) \cdot 1) \\ & - (-L_2 s_{12} - L_3 s_{123})((L_1 c_1 + L_2 c_{12} + L_3 c_{123}) \cdot 1 - (L_3 c_{123}) \cdot 1) \\ & + (-L_3 s_{123})((L_1 c_1 + L_2 c_{12} + L_3 c_{123}) \cdot 1 - (L_2 c_{12} + L_3 c_{123}) \cdot 1) \end{aligned} \tag{2.30}$$

Cancelling out some like terms, it simplifies slightly

$$\begin{aligned} |J| &= (-L_1 s_1 - L_2 s_{12} - L_3 s_{123})(L_2 c_{12}) \\ &\quad - (-L_2 s_{12} - L_3 s_{123})(L_1 c_1 + L_2 c_{12}) \\ &\quad + (-L_3 s_{123})(L_1 c_1) \end{aligned} \tag{2.31}$$

Expanding all factors

$$\begin{aligned} |J| &= -L_1 L_2 s_1 c_{12} - L_2^2 s_{12} c_{12} - L_2 L_3 s_{123} c_{12} \\ &\quad + L_1 L_2 s_{12} c_1 + L_2^2 s_{12} c_{12} + L_1 L_3 s_{123} c_1 + L_2 L_3 s_{123} c_{12} \\ &\quad - L_1 L_3 s_{123} c_1 \end{aligned} \tag{2.32}$$

This can be simplified greatly to

$$= L_1 L_2 (s_{12} c_1 - s_1 c_{12}) \tag{2.33}$$

This can be simplified further with the following trigonometric angle sum identity

$$\sin(\alpha)\cos(\beta) - \sin(\beta)\cos(\alpha) = \sin(\alpha - \beta) \tag{2.34}$$

Employing this identity into equation (2.33) yields

$$|J| = L_1 L_2 \sin(\theta_2) \tag{2.35}$$

Thus it is clear that the determinant of the Jacobian is a function of the second joint angle alone. The matrix will be singular when this angle is either 0 or 180 degrees. This is physically represented as the second joint being either fully

extended or fully flexed. The implications of this for kinematic analysis are that the manipulator can follow a desired end effector velocity as long as it avoids going through this configuration. When the manipulator is fully extended, such as in a rest state, the kinematic relation in equation (2.29) can not be used to find the joint angular velocities.

2.2.4 Static Analysis of a 3R Serial Chain

The end effector will be under some load that consists of in-plane forces and moments, as depicted in Figure 2.1. All external loads can be expressed by orthogonal force components F_x, F_y, and moment M.

$$F = \begin{bmatrix} F_x \\ F_y \\ M \end{bmatrix} \tag{2.36}$$

This load can be generalized to a single force and moment, sometimes referred to as a wrench. This end effector wrench will apply torques to each joint in the system. As the external load displaces the end effector, it causes infinitesimal torques and displacements throughout the system. The total work done by the sum of these infinitesimal loads is denoted as the virtual work. The virtual work can be calculated by considering the infinitesimal torques on each joint, as well as the total force and moment on the end effector. For a three jointed manipulator

this is given by

$$\delta W_j = \tau_1 \delta\theta_1 + \tau_2 \delta\theta_2 + \tau_3 \delta\theta_3 \tag{2.37}$$

$$\delta W_Q = F_x \delta Q_x + F_y \delta Q_y + M_Q \delta\Theta \tag{2.38}$$

$$\delta W = \delta W_j + \delta W_Q \tag{2.39}$$

Where δW_j is the virtual work on each joint, δW_Q is the virtual work on the end effector, and δW is the total virtual work in the system. Reorganizing terms into matrix containers, the virtual work is

$$\delta W = \tau^T \delta\theta - F^T \delta Q \tag{2.40}$$

where τ, $\delta\theta$, δQ are 3×1 vectors containing the joint torques, infinitesimal joint angular displacements, and infinitesimal end effector displacements, respectively.

The differential relationship between finite joint displacements and finite end effector displacements is given by the jacobian.

$$\delta Q = J\delta\theta \tag{2.41}$$

Which was derived in equation (2.26). It is desired for the joint torques to be in static equilibrium with the external load from the actuator at the desired pose. Hence, the equilibrium condition is imposed on equation (2.40). The Jacobian relation from equation (2.41) can also be substituted in for simplification.

$$0 = \tau^T \delta\theta - F^T J \delta\theta \tag{2.42}$$

$$0 = (\tau^T - F^T J)\delta\theta \tag{2.43}$$

For all end effector displacements, this gives the final result

$$\begin{gathered} \tau = J^T F \\ \begin{bmatrix} \tau_1 \\ \tau_2 \\ \tau_3 \end{bmatrix} = J^T \begin{bmatrix} F_x \\ F_y \\ M_z \end{bmatrix} \end{gathered} \tag{2.44}$$

Equation (2.44) allows for the equivalent joint torque τ_i on each joint to be calculated using only the desired end effector pose and the known actuator load.

2.2.5 Determining Equivalent Joint Stiffnesses

In Eq. (2.44) the equivalent joint torques necessary to balance the system for a given end effector load are given. It is desired to design the flexure joints so that they have the appropriate stiffness for the known end effector load. The equivalent joint stiffnesses associated with these equivalent torques can be found with the torsional stiffness relation

$$K_i = \frac{\tau_i}{\theta_i} \tag{2.45}$$

where K_i gives the stiffness for the i^{th} joint. The flexure joints are beams, so their torsional stiffnesses can also be approximated via the PRBM

$$K_i = \frac{E_i I_i}{L_{f_i}} \tag{2.46}$$

where K_i is the beams bending stiffness, E_i is the flexure material's elastic modulus, I_i is the bending moment of inertia and L_{f_i} is the length of the beam. For a

rectangular cross section the bending moment of inertia is

$$I_i = \frac{w_i t_i^3}{12} \tag{2.47}$$

where w_i and t_i are the width and thickness of the i^{th} cross section. By substituting the expressions for joint stiffness Eq. (2.45), and the beam inertia of Eq. (2.47) into Eq. (2.46), the relationship between flexure beam geometry and equivalent joint torques can now be established as

$$\frac{\tau_i}{\theta_i} = \frac{E_i w_i t_i^3}{12 L_{f_i}} \tag{2.48}$$

where τ_i is determined by Eq. (2.44) through the jacobian and applied loads. With the assumption that there is a fixed flexure length and width, this can be expressed in terms of flexure thickness.

$$t_i = \sqrt[3]{\frac{12 L_{f_i}}{E_i w_i} \frac{\tau_i}{\theta_i}} \tag{2.49}$$

The flexure thickness equation given by Eq. (2.49) allows for the flexure design to be driven directly by design space requirements, such as the required manipulators size, shape, actuator load, and end pose.

2.2.6 Investigating PRBM Accuracy Over Varying Flexure Lengths

This approach has some simplifications, including the PRBM's assumption of midpoint characteristic radius. As such it is expected to see the joints performance under load deviate from the analytical basis. The PRBM also reduces each flexure

to a pin joint, so it is expected that there will be larger errors with longer flexures. It is desired to investigate how well this simple joint design performs over a range of flexure lengths, to approximate the range of valid inputs. Using the method described above, several 3R mechanisms were designed for the same pose and load, but with decreasing flexure lengths. The flexure length L_f ranges from a long flexure of 20 millimetres, to a small flexure length of 0.2 millimetres approximating a pin joint. For each model, the link lengths were changed accordingly to maintain a constant mechanism length. A finite element analysis (FEA) was performed using Abaqus to determine the response of these designs to the intended load. The FE models for the varying flexure lengths are displayed in Figure 2.2.

The joint stiffnesses and end effector position were measured from the FEA results and used to calculate relative error in the analytical model. The position and stiffness errors for decreasing flexure lengths are presented in Figure 2.3. As expected, long flexure lengths lead to larger end effector position errors. The effect of flexure length on position error can also be seen in Figure 2.2, as the shorter flexures allow for a better approximation of a 3R pose. Note that self contact was not considered for this analysis, and in reality the joint angles would be limited by links in contact. For all cases the measured stiffness has a slight error, but even for the longest flexures the stiffnesses are within a 0.5% error margin.

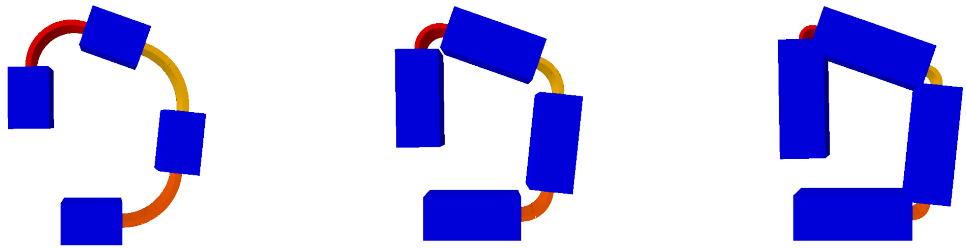

(a) $L_f = 20mm$ (b) $L_f = 10mm$ (c) $L_f = 5mm$

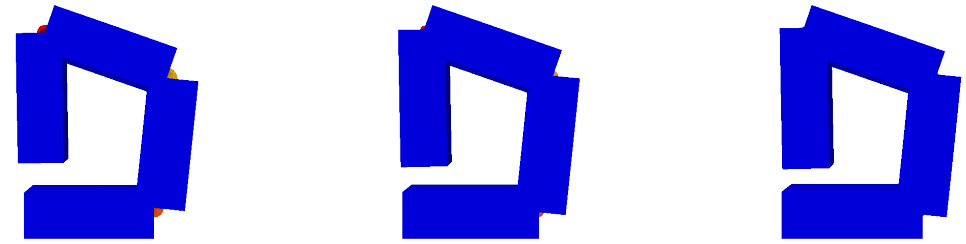

(d) $L_f = 2.5mm$ (e) $L_f = 1mm$ (f) $L_f = 0.2mm$

Fig. 2.2 Compliant joint performance for decreasing different lengths

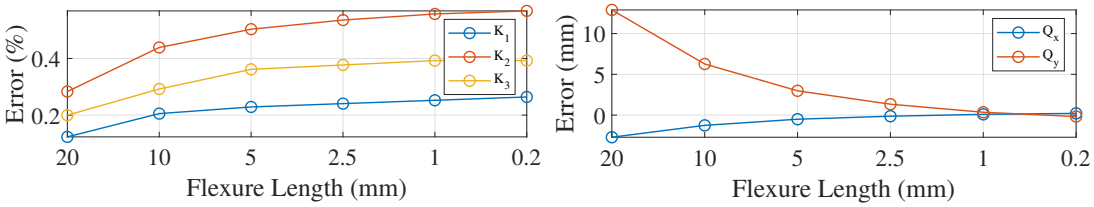

(a) Joint stiffness relative error (b) End effector position error

Fig. 2.3 FEA results of simple beam PRBM accuracy over varying flexure lengths for the 3R mechanism

2.3 Prototype Design

The prototype fingers are actuated by a linear actuator, the SMA coil, which is attached to a tendon which is routed through the links via a routing hole, and attached to the end effector. A displacement at the end of the tendon will induce a moment on each of the joints and cause rotation of the compliant joint, as shown in Figure 2.4. As the tendon is run parallel to the length dimension of the finger the end effector load is a pure moment M, with $F_x = F_y = 0$. Since the tendon is restricted by the routing hole, the moment arm will be from the height of the routing hole H_r to the midpoint of the flexures in the thickness direction. As the equivalent moment is dependent on thickness, and the thickness is dependent on the load, there is a recursive relationship. Similar coupling exists between the joint angles, minimum flexure lengths, and flexure thicknesses. Without restricting one or more parameters, an iterative calculation process can be employed to determine the required parameters for a given set of design parameters such as end effector position, load, and link sizes.

1. *Compute the inverse kinematics*
2. *Assume an initial thickness t_o for each joint $t_i = t_o$*
3. *From the expected linear actuator force, compute the load vector*

$$\begin{bmatrix} F_x \\ F_y \\ M \end{bmatrix} = \begin{bmatrix} 0 \\ 0 \\ F_{actuator}(H_r - t_o/2) \end{bmatrix}$$

4. The minimum flexure lengths are dependent on the required joint angles, and the arc segment caused by two links in contact

$$\begin{bmatrix} L_{f1} \\ L_{f2} \\ L_{f3} \end{bmatrix} = \begin{bmatrix} (H - t_1)\theta_1 \\ (H - t_2)\theta_2 \\ (H - t_3)\theta_3 \end{bmatrix}$$

5. Calculate the equivalent joint torques

$$\begin{bmatrix} \tau_1 \\ \tau_2 \\ \tau_3 \end{bmatrix} = J^T \begin{bmatrix} 0 \\ 0 \\ M \end{bmatrix}$$

6. Determine the required joint thicknesses for this iteration

$$t_i = \sqrt[3]{\frac{12L_{f_i}}{Ew}\frac{\tau_i}{\theta_i}}$$

7. Repeat steps 3 through 6 until the flexure thickness and flexure length converge

Using the algorithm described above, two prototypes were designed for a 10 N and 15 N linear actuator load respectively. In this implementation of the design algorithm the flexure thicknesses were constrained to produce a single thickness parameter for each joint, with corresponding flexure lengths. For the flexure material, commercial TPU 95A filament from Ultimaker was selected due to its excellent flexibility, with a flexural modulus of 78.7 MPa [102]. The flexure design parameters for the prototypes are tabulated in Table 2.1.

It is also necessary to consider how the physical 3D prints differ from the design parameters. The accuracy of the part dimensions is limited by the resolution of the printer. The 3D printer used for manufacturing these prototypes was an Ultimaker

S5, which has a nominal layer height of 100 microns for TPU 95A. Hence, the 3D-printed flexures for the prototypes can only be printed to a layer height of 100 microns, which can lead to discrepancies between the required thicknesses and the prints. The measured dimensions of the printed parts are given in Table 2.2.

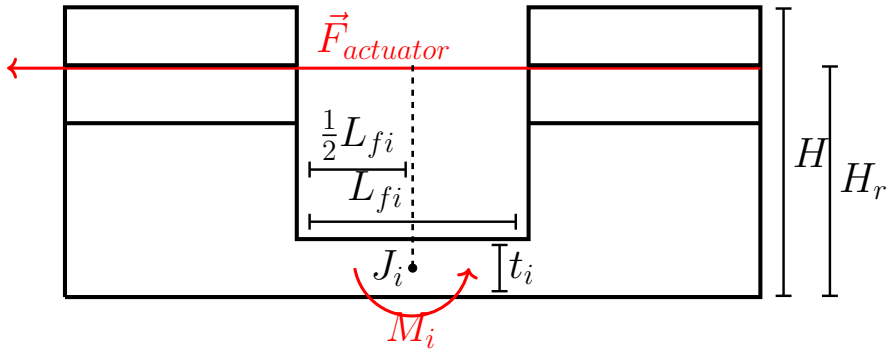

Fig. 2.4 Tendon induced moment on the PRBM joint

2.4 Experimental Results

2.4.1 Experimental Setup

A linear displacement test is conducted to see the prototype fingers performance under load. Figure 2.5 shows the experimental setup for the test. A coated copper wire acts as the tendon, routed through the links and attached to the end effector with a stopper. The finger base is fixed to a mount, while a Thor Labs LT1/M linear displacement stage pulls the muscle tendon. The tensile force of the wire is measured with a Transducer Techniques MDB-25 high precision load cell, while

Table 2.1 Calculated design parameters for the fingers

Parameter	Design 1	Design 2
F (N)	10	15
Q_x (mm)	15	15
Q_y (mm)	6	6
Θ (deg)	270	270
t (mm)	1.8807	2.1208
L_{f_1} (mm)	12.281	11.918
L_{f_2} (mm)	15.118	14.670
L_{f_3} (mm)	10.863	10.542

Table 2.2 3D-printed finger measurements

Dimension	10N Print	15N Print
t_1 (mm)	1.85±0.016	2.21±0.004
t_2 (mm)	1.84±0.013	2.20±0.009
t_3 (mm)	1.84±0.011	2.20±0.012
L_0 (mm)	33.76±0.009	33.87±0.070
L_1 (mm)	18.69±0.029	19.07±0.010
L_2 (mm)	14.71±0.009	15.01±0.022
L_3 (mm)	14.53±0.020	14.67±0.017
L_{f_1} (mm)	12.30±0.044	11.97±0.048
L_{f_2} (mm)	15.04±0.018	14.66±0.037
L_{f_3} (mm)	10.84±0.017	10.56±0.031

the stage's displacement is measured with a Keyence LK-H082 optical laser sensor. The sensor data is acquired using Speedgoat hardware with an IO133 DAQ module, using Matlab version R2021b. A video recording of each experiment is combined with a motion tracking program to measure the link motions during displacement

as well as the final pose. Figure 2.6 shows the camera view of the finger during a displacement test.

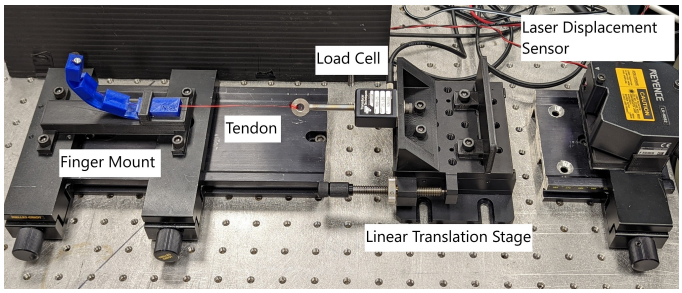

Fig. 2.5 Displacement test experimental setup

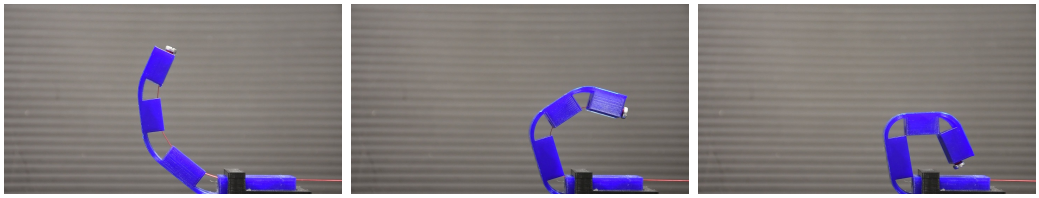

(a) Pose at $d = 18.72$ mm, $F = 2.8$ N (b) Pose at $d = 31.91$ mm, $F = 5.56$ N (c) Pose at $d = 40.52$ mm, $F = 9.31$ N

Fig. 2.6 10 N finger during the linear displacement test

2.4.2 Displacement Test Results

The average close force and end effector positions are given in Table 2.3. The two finger designs consistently achieve their final pose around 8.9 N and 14.2 N, slightly less than their designed-for actuator forces of 10 and 15 N. The two fingers show

an end effector position error of less than 10 millimetres for both Q_x and Q_y, which also affects the end effector orientation. This corresponds with the position error predictions in Figure 2.3 for flexure lengths in the range of 10 to 15 millimetres. The force and position data from the sensors was used to create the force-displacement (F-D) plots in Figs. 2.7(a) and 2.7(b). These show a substantial hysteresis curve, with distinct profiles for the pull, the motion from neutral to curled, and return segments of the motion.

During the pull segment, the F-D curve is approximately linear for the majority of the motion, but the force per millimetre increases nonlinearly as the finger approaches the final position. There is a steep decrease in force as the return segment begins due to energy loss in the flexure material. After the initial drop the F-D relationship again becomes approximately linear, with a more gradual slope than before. The experiments also showed that during the return segment, some deformation in the joints keep the end effector slightly raised as the finger approaches its neutral position. This results in the tendons tensile force reaching zero before the linear translation stage fully returns to its initial position. This can also be seen in the motion tracked trajectory plot in Figure 2.8.

The motion tracking of the finger was performed using the MATLAB computer vision toolbox to track eigenfeatures on the link edges. As can be seen in the trajectory plot in Figure 2.8, the pull and return segments display asymmetric tra-

Table 2.3 Summary of displacement test results

Average Measurement	10 N	15 N
$\bar{F} \pm \sigma$	8.927 ± 0.554 N	14.177 ± 0.631 N
$\bar{Q}_x \pm \sigma$	13.01 ± 1.03 mm	11.19 ± 1.88 mm
$\bar{Q}_y \pm \sigma$	10.43 ± 1.29 mm	13.62 ± 1.90 mm

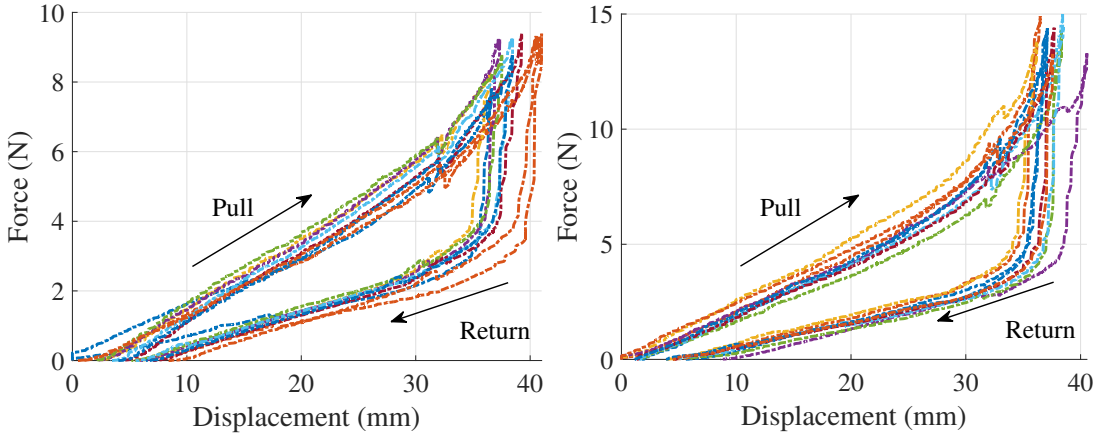

(a) 10 N finger

(b) 15 N finger

Fig. 2.7 Experimental force-displacement profiles for the finger designs

jectories. This path deviation is most pronounced in the end effector. The end effector's trajectory is heavily influenced by the behaviour of all previous joints in the serial chain. The trajectory plot shows that the end of the first rigid link (shown in yellow) has little to no path deviation, thus it is joint 2 and joint 3 which experience different bending motions during the pull and return segments, affecting the trajectory of the second and third links. The motion tracking also displays a slight

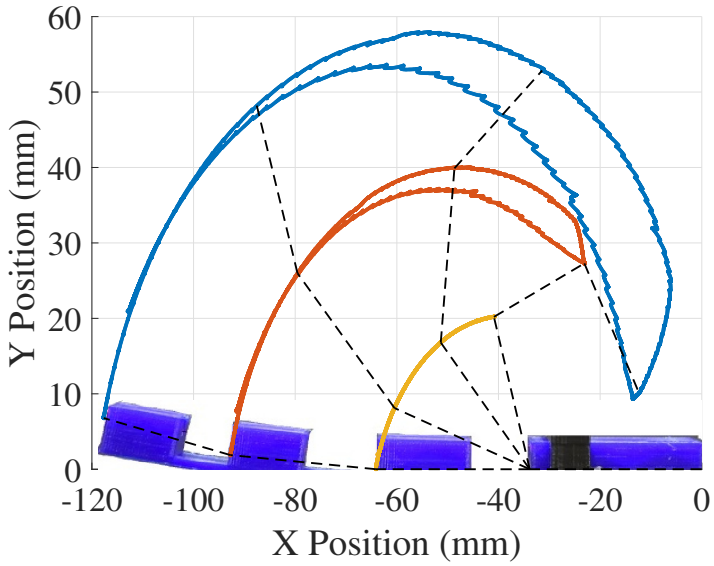

Fig. 2.8 Motion tracking of finger links during the linear displacement test

cyclic motion in the link positions through time, due to the incremental adjustment of the translation stage. However this reveals that the joints are displaying a relaxation effect. As previously observed, the finger structure experiences some deformation at the end of the return segment which slowly decays over time, and does not appear to affect the close force or F-D profile.

The deformation and force drop in the return segment indicates some energy loss in the flexure joints. The joints did not have the expected restoration forces expected due to the hysteresis of the flexure material. This energy loss would impact the effectiveness of the bias mechanism against a linear actuator like the shape memory alloy coil, as it lacks the required restoration force to fully return an

actuator to its initial position. This can be resolved by designing the joints for a larger force than normally desired, or by careful selection of a material with smaller hysteresis behaviour.

The experimental results show that the mechanism design is able to balance a known actuator load near the desired force and position. This indicates that the flexure joints have the appropriate stiffnesses as designed to balance the end effector load. The validity of the PRBM assumptions and joint design equations were also confirmed via FEA. The energy loss observed in the flexures may affect the bias distance for the actuator, however this may be improved through design. These results indicate that a compliant structure will functionally work as an antagonist mechanism to an SMA actuator.

3 SMA Modelling, Design, and Characterization

In this chapter, the methodology for designing, fabricating, and testing a shape memory alloy coil actuator is discussed. Unlike using off the shelf actuator components, it is necessary to determine the actuation characteristics of the SMA coil. This is because the actuator profile will be affected by the coil geometry and the annealing process. Some of characteristics of interest are the coil's force-displacement (F-D) profile, current to force (activation) time, and cooling times.

3.1 Designing an SMA Coil Actuator

Many models of SMA behaviour are based on the work by Tanaka et al. [9]. The Tanaka model presents a thermomechanical description for materials in the process of solid to solid phase transition. It introduces the use of internal state variables to describe the unidirectional strain, temperature, and extent of phase transition. This model was expanded and modified by subsequent studies, such as Rogers and Liang [10]. Some works looked at modelling the micromechanical behaviour of SMA

and its effect on macro-scale motion [42,48,103,104]. Building on these constitutive thermomechanical models, many researchers have incorporated state-based models into the design of SMA wire or coil actuators [11,14,15,36,45,53,66,105–108].

3.1.1 Cho Static Two State Model

Cho et al. [2] presented design methodology for SMA coil actuators using a static two state model. This model utilizes the SMA thermomechanical constitutive equations established by previous studies, such as Tanaka [9] and Rogers & Liang [10]. This design methodology establishes different force-deflection relationships for the SMA at full martensite, and full austenite. From an analysis of shear stress-strain behaviour within a coil, this model puts forward relationships between the geometry and the axial force of the coil, for each phase. An important aspect of this model is that it relies on experimental characterization of the material to determine some physical parameters, such as critical stresses and residual strain. The Cho model design method does not consider interphase behaviour and focuses only on the force and deflection requirements for the endpoints of a stroke, as shown in Figure 3.1. This is meant to simplify coil design for use as actuators [2]. This section will briefly outline the key points of the Cho model, before applying it to design the required SMA coil actuators for this work.

Cho [2] identifies four major coil design parameters. They are the wire diameter

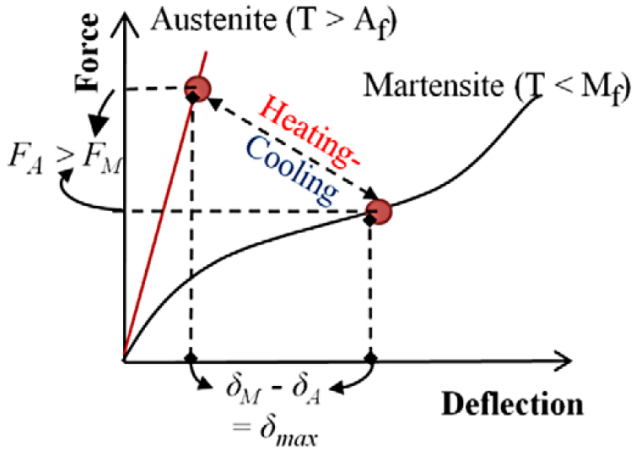

Fig. 3.1 SMA stroke between required martensite and austenite forces on two-state FD curves [2]

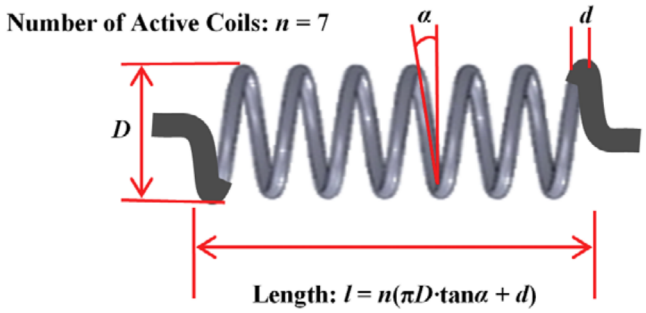

Fig. 3.2 SMA coil design parameters [2]

d, the coil diameter D, the pitch angle α, and the number of active coils n. The design parameters are shown in Figure 3.2. The pitch angle refers to the half angle between two loops of the coil. The coil diameter is taken across the coil between the midpoints of the wire thickness. It is assumed that the pitch angle is consistent across the active coil length. However it is important to note that some

of these parameters are not static. The pitch angle and diameter are related to the displacement δ (or deflection) of the coil, which means the coil length displacement with respect to the austenite trained length, l_i. As the coil is stretched out, the pitch angle between two coil loops will increase, and the coil diameter will contract. So the following notation is introduced, where α_i denotes the initial pitch angle (i.e at $\delta = 0$) and α_f denotes the pitch angle at some displacement δ.

The force profiles for each state are given by

$$\begin{aligned} F_A &= \frac{G_A d^4}{8D^3 n} \frac{\cos^3(\alpha_i)}{\cos^2(\alpha_{A_f})\left(\cos^2(\alpha_{A_f}) + \dfrac{\sin^2(\alpha_{A_f})}{1+\nu}\right)} \times \delta \\ F_M &= \frac{G_M d^4}{8D^3 n} \frac{\cos^3(\alpha_i)}{\cos^2(\alpha_{M_f})\left(\cos^2(\alpha_{M_f}) + \dfrac{\sin^2(\alpha_{M_f})}{1+\nu}\right)} \times \delta - \frac{\pi d^3 G_M \gamma_L \xi}{8D} \end{aligned} \tag{3.1}$$

It is important to note that the martensite force profile contains a term not present in the austenite profile, $\dfrac{\pi d^3 G_M \gamma_L \xi}{8D}$. This term is meant to model the martensite crystal lattice shifting from a twinned state to a detwinned state. This detwinning term includes the detwinned martensitic volume fraction, ξ. This represents the volume ratio of detwinned martensite to the total volume of SMA.

$$\xi = \begin{cases} 0, & \text{for } \tau < \tau_s^{cr} \\ \frac{1}{2}\cos\left(\frac{\pi(\tau - \tau_f^{cr})}{\tau_s^{cr} - \tau_s^{cr}}\right) + \frac{1}{2}, & \text{for } \tau_s^{cr} \leq \tau \leq \tau_f^{cr} \\ 1, & \text{for } \tau > \tau_f^{cr} \end{cases} \tag{3.2}$$

Here the detwinning behaviour is modelled using a sinusoidal pattern. The detwinning process occurs between the starting detwin critical stress τ_s^{cr} and the final detwin critical stress τ_f^{cr}. The detwinning behaviour can be seen in the martensite stress strain relationship shown in Figure 3.3, as well as in the martensite force profile in Figure 3.1. The detwinned volume fraction also depends on the shear stress, τ.

$$\begin{aligned} \tau_A &= G_A\gamma \\ \tau_M &= G_M\gamma - G_M\gamma_L\xi \end{aligned} \tag{3.3}$$

Where γ is the shear strain for the coil at this deflection, and γ_L is the maximum residual strain. The shear strain can be described in terms of the pitch angle

$$\gamma = \frac{d}{D}\frac{\cos^2(\alpha_i)(\sin\alpha_f - \sin\alpha_i)}{\cos^2(\alpha_f)(\cos^2(\alpha_f) + \sin^2(\alpha_f)/(1+\nu))} \tag{3.4}$$

where the pitch angle α_f for a deflection δ is given by

$$\alpha_f = \sin^{-1}\left(\delta\frac{\cos\alpha_i}{\pi n D} + \sin\alpha_i\right) \tag{3.5}$$

3.1.2 Application of the Static Two State Model

There is a complex nonlinear relationship between the equations for this design methodology. Thus it is important to note that rather than predicting SMA behaviour, the purpose of this model is to output the required coil geometry for given

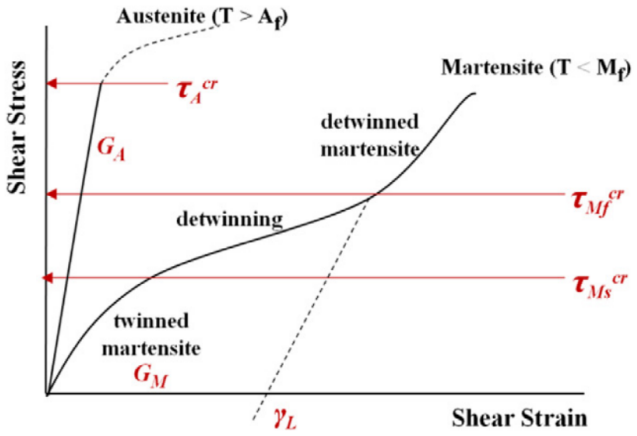

Fig. 3.3 Stress strain behaviour of two states, austenite and martensite, with key parameters [2]

force and stroke requirements. The design process flow is as follows. First, the user inputs the minimum required forces for the actuator at both ends of the stroke, at full austenite F_A and at full martensite F_M. The ratio between the required forces and the critical stress for that state are calculated and compared between the two states, to determine the greater of the two.

$$(F_r, \tau_r) = \max\left(F_A/\tau_A^{cr}, F_M/\tau_M^{cr}\right) \tag{3.6}$$

After determining the required force, at least two design parameters must be pre-selected from the set of (d, D, α_i, n). After pre-selecting two design parameters, the remaining parameters are calculated. For example, the coil diameter can be found from the conventional force output of a spring, equation (3.7). However

in practical terms, most of these parameters are not completely free. The wire diameter and coil diameter are limited by the availability of commercial wire, and the winding tools used to create the coil. The pitch angle is also quite difficult to accurately control, so it can be assumed to be some small angle. This typically leaves only the coil length to be determined once other selections are made.

$$D = \tau_r \pi \frac{d^3}{8F_r} \tag{3.7}$$

Once the two state FD equations are solved to determine the corresponding pitch angle to the required stroke forces. These are found by re-expressing the FD equations in terms of pitch angle alone, eliminating δ from the equation.

$$\begin{aligned} F_A &= \frac{G_A d^4 \pi}{8D^2} \frac{\cos^2(\alpha_i)(\sin(\alpha_{A_f}) - \sin(\alpha_i))}{\cos^2(\alpha_{A_f}) \left(\cos^2(\alpha_{A_f}) + \dfrac{\sin^2(\alpha_{A_f})}{1+\nu} \right)} \\ F_M &= \frac{G_M d^4 \pi}{8D^2} \frac{\cos^2(\alpha_i)(\sin(\alpha_{M_f}) - \sin(\alpha_i))}{\cos^2(\alpha_{M_f}) \left(\cos^2(\alpha_{M_f}) + \dfrac{\sin^2(\alpha_{M_f})}{1+\nu} \right)} - \frac{\pi d^3 G_M \gamma_L \xi}{8D} \end{aligned} \tag{3.8}$$

Solving these equations for α_{A_f} and α_{M_f} gives the pitch angles corresponding to the required forces F_A and F_M. The pitch angles are related to the displacement δ from the initial pitch angle α_i

$$\delta = \frac{\pi n D}{\cos \alpha_i} (\sin \alpha_f - \sin \alpha_i) \tag{3.9}$$

Therefore the actuation stroke of the coil can be expressed as the displacement

between the pitch angles at 100% martensite and 100% austenite

$$\delta_{stroke} = \frac{\pi n D}{\cos \alpha_i}(\sin \alpha_{M_f} - \sin \alpha_{A_f}) \tag{3.10}$$

For a given stroke requirement, and the pitch angles at the required force endpoints, this allows for the number of coil loops n to be isolated

$$n = \frac{\cos \alpha_i}{\pi D(\sin \alpha_{M_f} - \sin \alpha_{A_f})}\delta_{stroke} \tag{3.11}$$

The coil loop number is easily translated into coil length, with the knowledge of other geometric parameters

$$l_i = n(\pi D \tan \alpha_i + d) \tag{3.12}$$

It should also be noted that for a given coil, the length l will vary as the coil is extended. Thus the following notation is introduced, where l_i indicates the austenite coil length with corresponding pitch angle α_i. This completes the set of equations required to determine the geometric parameters for a coil.

3.1.3 Coil Designs

The shape memory alloy used for this research is commercially available 0.015" (391μm) diameter NiTi (50%/50%) wires from Dynalloy (branded as Flexinol). In order to use the Cho static two state design methodology, it is required to obtain material properties for the alloy. The manufacturer data [1] does not supply all the

required information, so the material characterization requires specialized tensile test equipment. However there are examples in the literature of characterization data for NiTi coils [2, 11, 14]. The characterization data from [2] will be used, as shown in Table 3.1

For the purposes of this thesis, coils were designed using the Cho methodology as follows. These coils are intended to match with the compliant finger. We select the maximum austenite force to be 15N ($F_A = 15N$), this will be the force required to pull the compliant finger mechanism to its closed position. The martensite force requirement is low, as seen from the finger F-D characterization (see Figure 2.7(b)), the initial force to deform the finger mechanism is near zero. However, as the force output is related to the coils shear strain, having a very low force requirement at a large deformation required the coil length to be quite long. In order to keep the coil length relatively short, a martensite force requirement such as 5N ($F_M = 5N$)

Table 3.1 NiTi flexinol coil material properties [1, 2]

Parameter	Value	Units	Description
d	381	μm	wire diameter
G_A	18.26	GPa	austenite shear modulus
G_M	6.98	GPa	martensite shear modulus
ν	0.33		poissons ratio
γ_L	5	%	residual strain
τ_A^{cr}	183	MPa	austenite critical stress,
$\tau_{M_s}^{cr}$	72.4	MPa	martensite detwinning start stress
$\tau_{M_f}^{cr}$	114	MPa	martensite detwinning finish stress

can be selected. Now with the maximum forces for each state selected, the ratios between the required force and critical stress for each state (from Table 3.1) are compared to determine the larger of the two.

$$\begin{aligned} \max(F_A/\tau_A^{cr}, F_M/\tau_M^{cr}) &= \max\left(\frac{15\text{ N}}{183\cdot 10^6\text{ Pa}}, \frac{5\text{ N}}{114\cdot 10^6\text{ Pa}}\right) \\ &= \frac{15\text{ N}}{183\cdot 10^6\text{ Pa}} \\ \rightarrow (F_r, \tau_r) &= (15\text{ N}, 183\cdot 10^6\text{ Pa}) \end{aligned} \tag{3.13}$$

The austenite ratio is greater than martensite, which sets the austenite parameters as the required force and shear stress.

The coil diameter D will be determined by the wire diameter d and the diameter of the winding rod used. From inspection of simple coil force relation (3.7) it is clear that a lower spring index (D/d) will increase force output. Thus it is desirable to wind on a small diameter rod. However during the winding process, rods that are too thin are liable to bend or break (see Section 3.2). As a middle ground, 1/16" winding rods are selected. This gives a coil diameter of

$$D = d + 1/16'' = 0.391\text{ mm} + 1.58\text{ mm} = 1.961\text{ mm} \tag{3.14}$$

During winding there is no way to maintain a precise pitch angle, hence it is chosen to be packed in as tight as can be. From manufacturing tests, the pitch angle was calculated from measuring the coil length of n consecutive loops from equation (3.12). With this winding technique the pitch angle is usually around 0.10°. Thus

with the design parameters d, D, and α_i pre selected, the required coil length can be determined. It is also important to note here that instead of mounting the SMA coil in line with the tendon, the coil will be doubled back. Therefore instead of finding the full length of the actuator, it is necessary to find the length for each half to supply half the required force. From the F-D equations in (3.8) the corresponding pitch angles to the required forces were found

$$\begin{aligned} F_A = 15 \text{ N}/2 = 7.5 \text{ N} \rightarrow \alpha_{A_f} = 10.7^\circ \\ F_M = 5 \text{ N}/2 = 2.5 \text{ N} \rightarrow \alpha_{M_f} = 21.1^\circ \end{aligned} \tag{3.15}$$

The function of the SMA coil is to pull on the compliant finger such that the links fully close down in a gripped state. The required stroke length for this is dependent on the flexure geometry. As described in Chapter 2, the range of motion of the joints will be dependent on the arc segment created by the flexures bending and two links coming into contact. Designing the coil actuator to match the 15 N finger, a stroke length of 37 mm is desired ($\delta_{stroke} = 37$ mm). Therefore, equations (3.11) and (3.12) can be used to find the required number of loops and the corresponding coil length as

$$\begin{aligned} n &= \frac{\cos \alpha_i}{\pi D(\sin \alpha_{M_f} - \sin \alpha_{A_f})} \delta_{stroke} \\ &= \frac{\cos(0.10^\circ)}{\pi 1.961 \cdot 10^{-3} \text{ m } (\sin(21.1^\circ) - \sin(10.7^\circ))} 37 \cdot 10^{-3} \text{ m} \\ &= 34 \rightarrow l_i = 13.5 \cdot 10^{-3} \text{ m} \end{aligned} \tag{3.16}$$

This result shows that the half coil must have an austenite trained length of 13.5 mm in order to provide a 37 mm stroke from 2.5 N to 7.5 N. Thus this gives the full coil length requirement of 27 mm. This design methodology gives the required coil geometry to match the actuator for the 15 N finger. The graphic in Figure 3.4 shows the theoretical FD coil profile (from equation (3.1)) matching the hysteresis of the 15N finger.

3.2 SMA Coil Manufacturing

Multiple coil samples were fabricated according to these specifications. The SMA is commercially purchased in wire configuration, so they must be manually wound into coils with the desired geometry. After winding, the coils are trained to remember this configuration as their memorized shape.

3.2.1 Winding

First the coil is wound using a drill and rod. The winding rod used is a 0.16" steel rod (4140 alloy). As the SMA displays superelastic behaviour, it is in fact quite difficult to work with. Even after severe deformation and bending, the SMA will elastically attempt to restore its straight wire shape. So to hold the SMA into place, two washers are clasped tightly onto the rod to hold the SMA down. They are held together with a nut and bolt. The SMA wire is fed through a custom tensioner

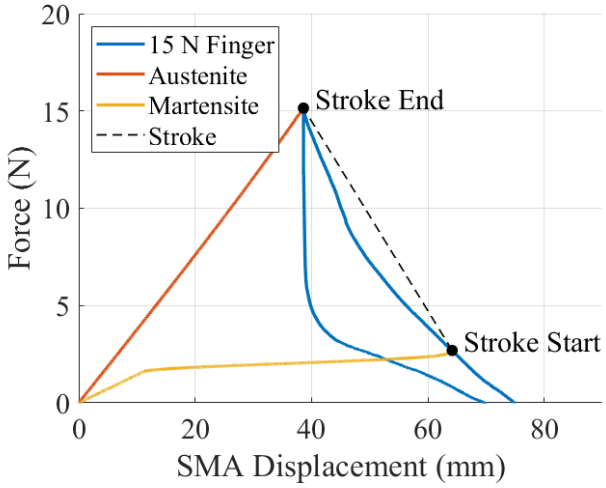

Fig. 3.4 Theoretical F-D curves for actuator design to match finger profile

tool and onto the rod, where it is initially wound by hand. Using the handheld drill, and maintaining tension on the wire, the wire is slowly wound around the rod. This technique does not allow for precise control of the pitch angle, but by maintaining tension and careful movement of the tensioner tool, the coil can be packed tightly. After winding to the desired length, the final coil loops are fixed with a second washer clip. A sample wound SMA coil is shown in Figure 3.5.

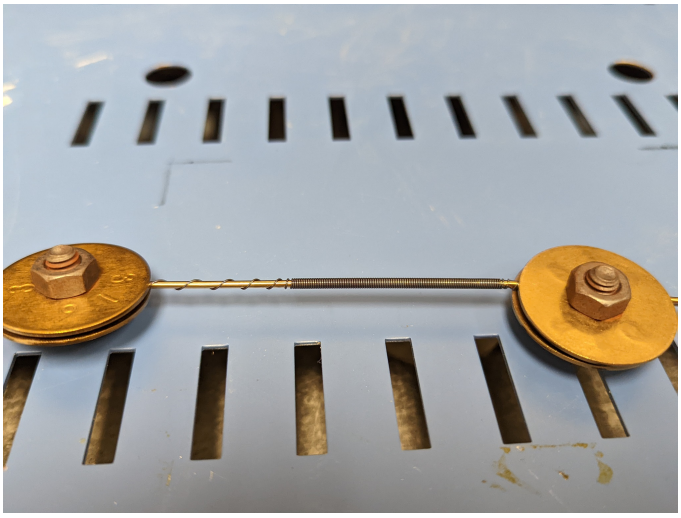

Fig. 3.5 Custom SMA coil wound on rod

3.2.2 Annealing

With the coil held in the desired shape, it is necessary to train the SMA so that it remembers this configuration. This requires transitioning the SMA to austenite phase while restricting movement. As the SMA fully transitions to austenite and is held in this configuration for some time, the crystal lattice will shift to the cubic structure. This effectively resets the shape memory, so that when the SME is triggered the coil will now attempt to restore this shape, instead of the manufactured straight wire configuration.

To accomplish this, the coil is annealed in a high temperature furnace. The austenite finish temperature for this alloy is listed at 90°C, but to ensure complete

phase transition and effective training it must be annealed at a higher temperature. These coils were heated to 400°C for annealing. Using a programmable furnace (Figure 3.6), the coils were heated from room temperature to 400°C over 30 minutes, and held at 400°C for one hour.

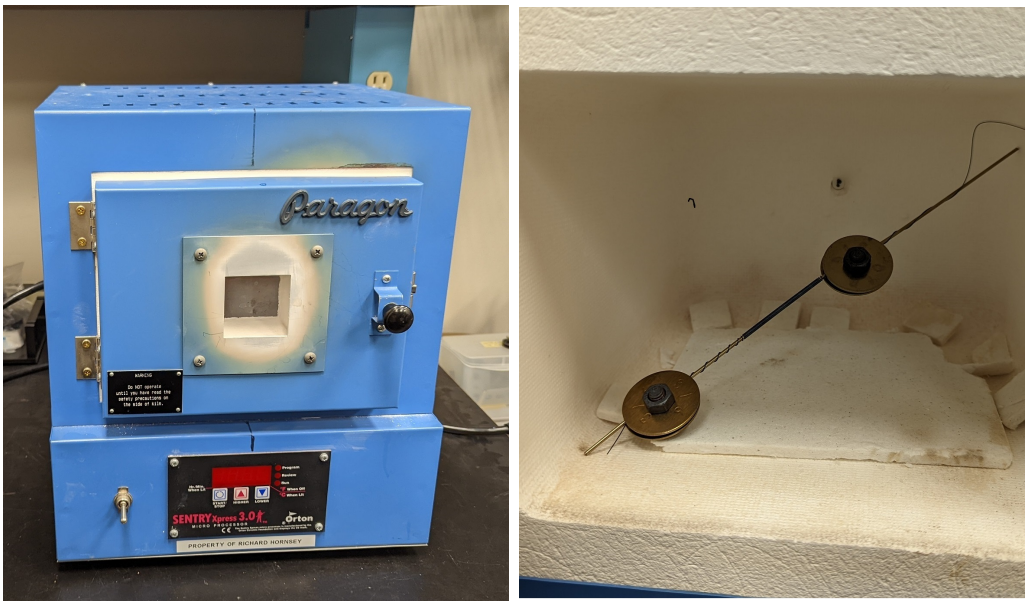

(a) Furnace view (b) SMA coil ready for annealing

Fig. 3.6 The SMA coil in the programmable high temperature furnace used for annealing

3.2.3 Cutting and crimping

As the winding process determines the coils pitch angle α and coil diameter D, and the wire diameter d is fixed, then the last step is to cut the coil to length. The wires were wound in coils much longer than required, so that multiple samples could be collected from one manufacturing batch. From a trained coil rod, the desired length was measured and then cut using wire cutters. This gives a fully functional SMA coil actuator.

The coil end points will be inserted into electrical terminals for the experimental setup. For a more secure connection, metal crimps were attached to the coil ends. This is achieved by straightening out the end loops as much as possible, inserting into the open crimp, and using a crimping tool to secure the coil within the crimp mounts. Commercial 1.25 mm crimps were used for this. It was found during blocked force experiments that the SMA could generate enough force to break free of the mount, if it is not crimped properly. Hence, it is important to ensure that there are at least three points of contact between the crimp bands and the coil, as shown in Figure 3.7(a), on the fully manufactured coil that is shown in Figure 3.7(b).

(a) Microscope view of crimp placement (b) SMA coil with crimps

Fig. 3.7 The SMA coil after all manufacturing steps

Several coils were fabricated in this way. The coil samples used for the characterization tests are listed in Table 3.2. Although all three of these samples are meant to follow the design derived in Section 3.1.3, they have slightly different designs due to small errors in fabrication. The pitch angles for each coil are calculated using the coiled length measurement and the number of coil loops, according to equation (3.12).

Table 3.2 Coil samples manufactured

Parameter	Coil 1	Coil 2	Coil 3
$d\ (\mu m)$	391	391	391
$D\ (mm)$	1.961	1.961	1.961
$\alpha_i\ (deg)$	0.11	0.06	0.31
$l_i\ (mm)$	25	27	28
n	62	68	66

3.3 Characterization Test Setup

3.3.1 Voltage to Current Circuit

The alloy being used is commercial NiTi from Dynalloy. The datasheet for this material lists T_{A_f} as 90°C. The phase transition from martensite to austenite will be thermally activated through Joule heating, meaning that the SMA will warm from room temperature to T_{A_f} and beyond due to the resistive heating of the current.

Although some examples in the literature describe controlling the SMA in terms of an input voltage, it is more accurate to control the input current. As shown in later results (see Figure 3.17) the phase change process will affect the electrical resistance of the SMA. Thus it is preferable to heat the SMA through Joule heating with a controlled input current. For this purpose, a voltage to current (V-to-I) circuit was designed and manufactured. A voltage to current converter allows for better control of the SMA current, using a voltage control signal to drive the input current.

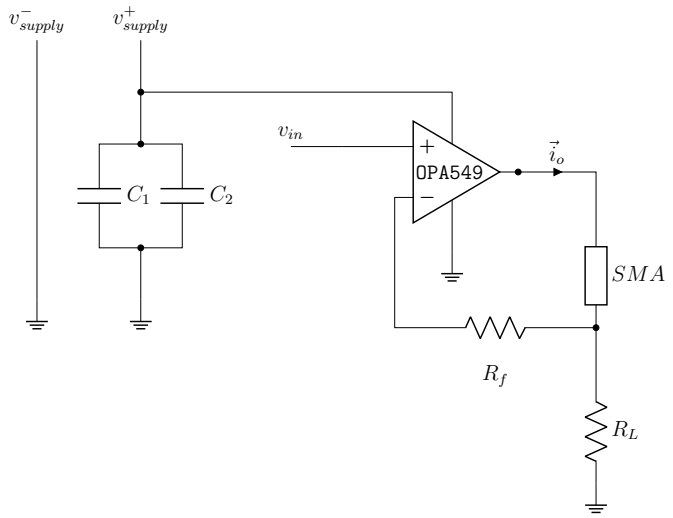

Fig. 3.8 Voltage to current circuit schematic

The V-to-I circuit is used as an interface between the control signal source and the SMA coil. The circuit takes the control signal voltage, and utilizes a high performance op-amp (TI OPA549) to drive the SMA with the corresponding current. An electrical schematic of the circuit is shown in Figure 3.8. This is a non inverting op-amp configuration, where the output current i_o is determined by the load resistor R_L.

$$i_o = \frac{v_{in}}{R_L} \tag{3.17}$$

The load resistor is a low impedance power resistor, which carries the op-amp output current to ground. During experiments a few different resistors were used, before settling on a 1Ω power resistor. This gives a 1:1 input voltage to output current ratio. The feedback resistor is selected as a high impedance component,

for this setup a standard $10k\Omega$ resistor is used. The op-amp is powered by a power supply unit, with bypass capacitors in place to help suppress supply noise.

With this schematic a printed circuit board (PCB) was designed and manufactured. A major design consideration for the PCB was component heating. The op-amp and the power resistor are mounted on opposite ends of the board with large heatsinks (shown in Figure 3.12). For the op-amp especially, prolonged operation at high current levels runs the risk of thermal damage, so multiple heatsinks were stacked onto each other and bonded with thermal epoxy. The PCB has connection terminals for the op-amp power supply, the control signal voltage, and for external wiring to the SMA . There are also two voltage monitor terminals, for the SMA and the load resistor.

The PCB is mounted to an optical table through a custom made mount, with bottom surface coverings for electrical isolation (Figure 3.9(b)). The op-amp is powered with a high power benchtop power supply unit (BK Precision 9103). The op-amp input voltage is connected to the Speedgoat IO133 module, which serves as the control signal for the SMA. The voltage monitors are also connected to the Speedgoat IO module and read in against time.

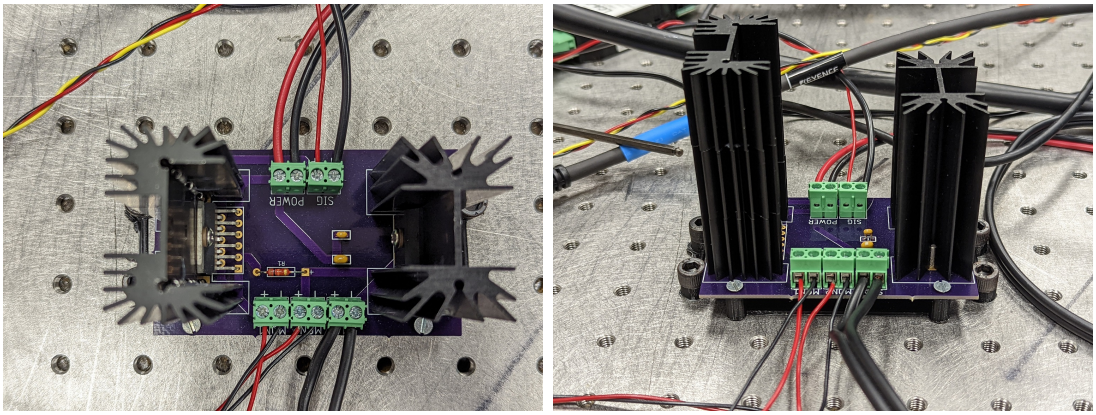

(a) Top view of the circuit board (b) Side view

Fig. 3.9 Populated voltage to current PCB

3.3.2 Mounting

For these characterization experiments, the crimps on the SMA coil ends are inserted into binding posts on the mounting block. Banana sockets on top of the binding posts are connected to the SMA terminal on the V-to-I PCB through 8 AWG wires. The mounting block is placed on a ThorLabs NRT 100/M linear translation stage, which is controlled with a BSC201 benchtop stepper motor controller. With the end points mounted, the coil is connected to a Transducer Techniques MDB-25 load cell. As shown in Figure 3.10, the coil is looped around through a bolt on an isolation block, which keeps the load cell electrically and thermally isolated from the SMA.

Initially, the SMA is mounted such that there is no displacement of the coil.

This configuration is the zero deflection, $\delta = 0$ for the experiment. From here, movement of the translation stage will cause the SMA coil to deform. The load cell measures the tension force of the SMA coil pulling on the isolation block.

3.4 Characterization Experimental Results

The manufactured coils were tested to obtain their force-displacement characteristics in both the martensite and austenite phases. The austenite F-D profile was obtained by performing static blocked force activation tests at discrete displacements. At each position the force output of the SMA was measured as it transitioned from martensite to austenite. These blocked force tests were repeated multiple times in each position. The average maximum force of the SMA for each displacement was used to create the force-displacement profile.

For the martensite F-D profile, the force output from the coil was measured as the coil was slowly displaced to a maximum of $\delta = 90$ mm. The analytical model used for the coil design is static, and it is known that SMA behaviour is strain-rate dependent, so these tensile tests were performed at a slow rate of 0.5 mm/s using the motorized stage.

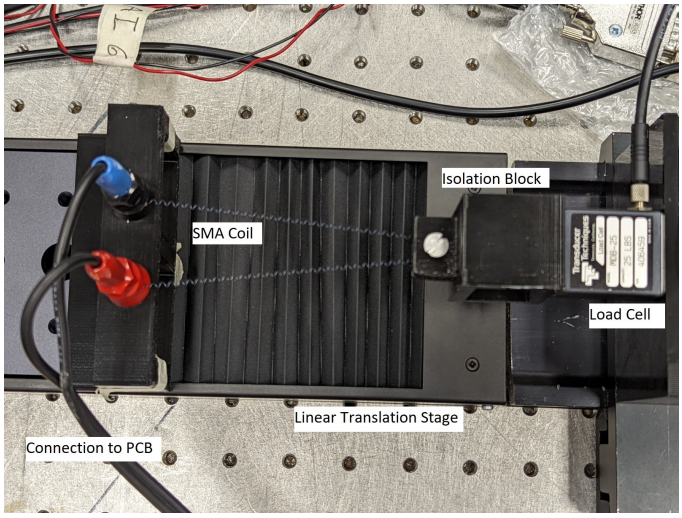

Fig. 3.10 SMA characterization experimental setup

3.4.1 Coil 1 Profile

The martensite experimental F-D profile is shown in Figure 3.12(b), with an overlay from the analytical model predictions. This curve is an average of several experimental runs. The shaded area around the curve indicates the standard deviation of the multiple data sets, for that displacement index. The individual martensite experiments showed some severe force drops, as the SMA occasionally deformed around the bolt attachment. This is due to coil loops slipping on the pin as the coil is strained and the pitch angles increase. However this only occurs sporadically, and does not affect the average profile.

The austenite force profile was obtained by performing blocked force tests starting at $\delta = 0$ mm up to $\delta = 90$ mm. At each displacement, multiple tests are

conducted to determine the required current and load time for the SMA to fully transition. For this coil, activation was achieved with a constant 2 A input current for 6 seconds. However at larger displacements of $\delta \geq 77.5$ mm, this conduction time was not long enough for the SMA to fully transition, so conduction time was increased to 8 seconds. One set of experimental data from a single run for coil 1 is shown in Figure 3.11. These plots show the measurements for the SMA generated force, as well as the SMA voltage and the input control voltage. The resulting austenite F-D profile is presented in Figure 3.12(a), alongside the analytical model predictions and markers indicating discrete test results. The shaded area for the austenite curve also indicates the standard deviation between experimental results.

These tests put the shape memory alloy through considerable stress, as it is attempting to recover its memorized shape but is restricted from movement. There was some concern that too many of these tests at larger displacements would begin to "burn out" the SMA. In other words the intense thermomechanical loading would partially retrain the material to remember a new shape, as the temperature of the SMA is not directly controlled. This turned out to be true, as after going through the characterization tests it was found that the coil sample had memorized a slightly deformed shape and was no longer able to retract all the way to its initial fabricated length. This prevented further testing with the same coil sample.

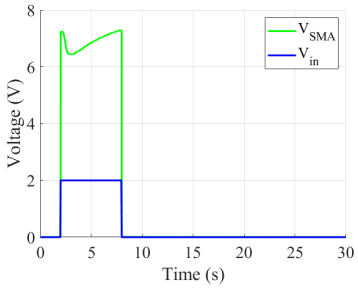

(a) Voltage at $\delta = 22.5mm$

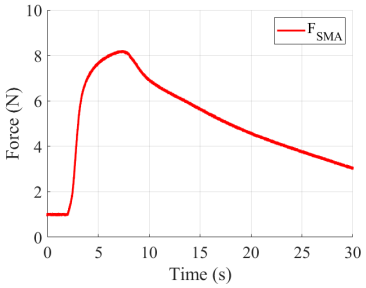

(b) Force at $\delta = 22.5mm$

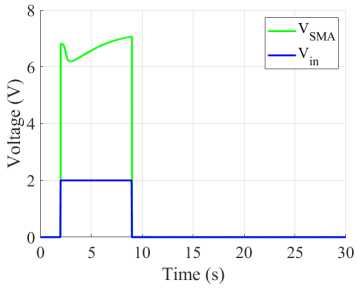

(c) Voltage at $\delta = 55mm$

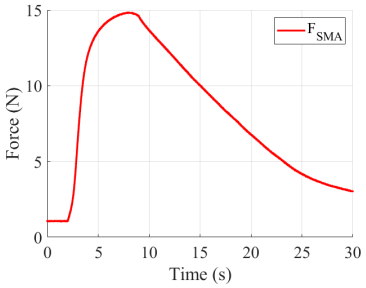

(d) Force at $\delta = 55mm$

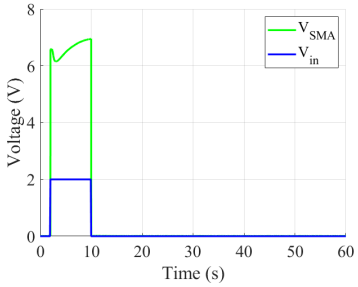

(e) Voltage at $\delta = 77.5mm$

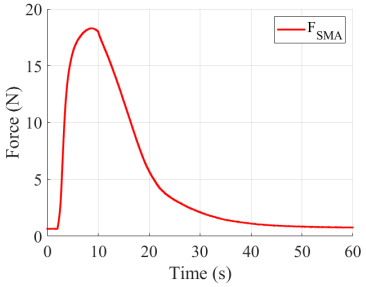

(f) Force at $\delta = 77.5mm$

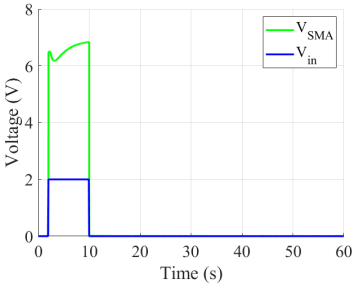

(g) Voltage at $\delta = 90mm$

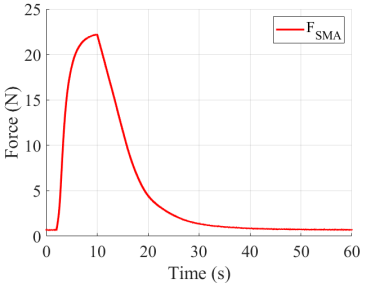

(h) Force at $\delta = 90mm$

Fig. 3.11 One set of experiments for coil sample 1 austenite characterization data

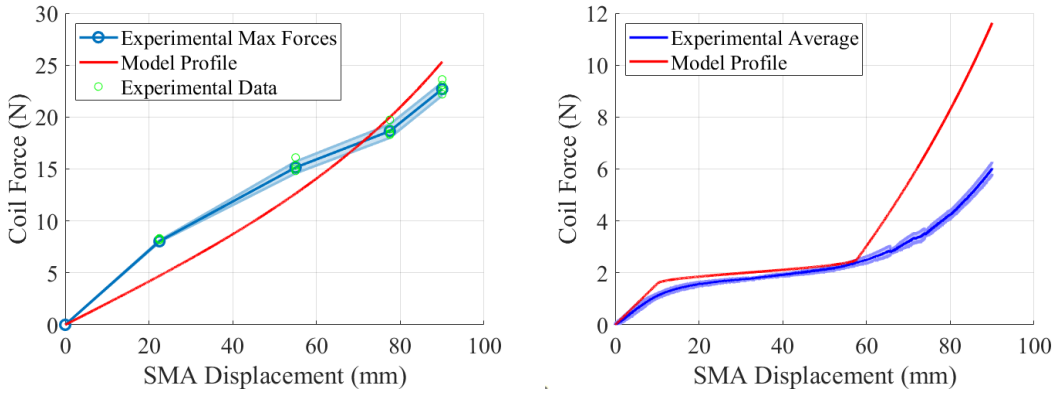

(a) Austenite (b) Martensite

Fig. 3.12 Coil sample 1 force-displacement profiles

3.4.2 Coil 2 Profile

Austenite test data for the second coil sample is shown in Figure 3.13. After observing from coil 1 that the austenite tests lead to SMA burn out, it was decided to test this coil with the extreme deformations first, to be confident in the force data for the largest displacements. That is to say, these static tests began at $\delta = 90$ mm, and then moved to lower displacements. Also building on the data from the first coil tests, austenite activation was achieved with a lower current for a longer period. This was estimated to accomplish phase transition without grossly exceeding the transformation temperature T_{A_s}. These tests were performed with 1.7A for conduction periods of 12 to 14 seconds.

It was found after $\delta = 55$ mm that the SMA had already begun to have it's

shape reset, and was no longer able to retract. The resulting F-D curve is presented in Figure 3.14. The partial reset of coil 2 also impacted the martensite data. The martensite tests were planned to be conducted after concluding the austenite tests. However a martensite profile could not be obtained after the SMA had been partially reset and re-trained to an extended shape. Therefore there is no martensite profile available for coil sample 2.

Although this occurred, the austenite data collected for coil 2 is kept for a number of reasons. Of the three coils tested, this is the only dataset which begins with the extreme deflection. This gives higher confidence that no burnout is occurring in the force measurement at $\delta = 90$ mm. The data also shows a high correlation with the model profile at $\delta = 90$ mm and $\delta = 77.5$ mm. The individual experimental runs also show little deviation between tests, as illustrated in Figure 3.14 by the overlapping data points for each displacement. For these reasons, the coil 2 data is presented alongside coil 1 and 3 to contribute to the austenite characterization.

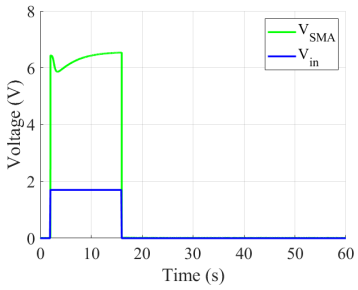

(a) Voltage at $\delta = 55mm$

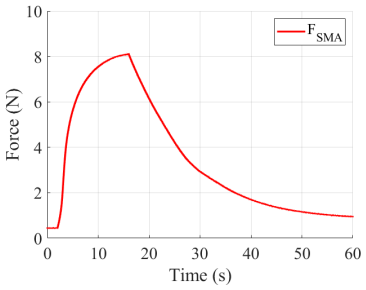

(b) Force at $\delta = 55mm$

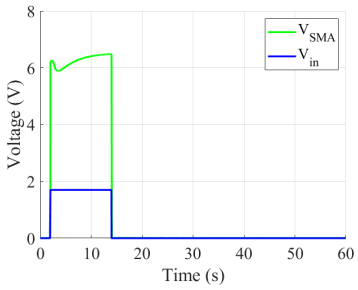

(c) Voltage at $\delta = 77.5mm$

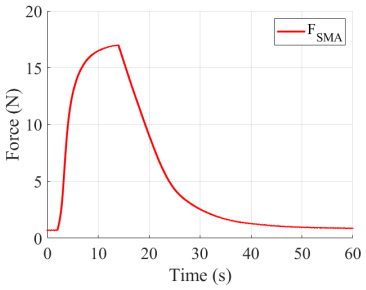

(d) Force at $\delta = 77.5mm$

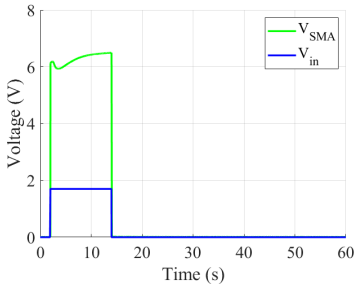

(e) Voltage at $\delta = 90mm$

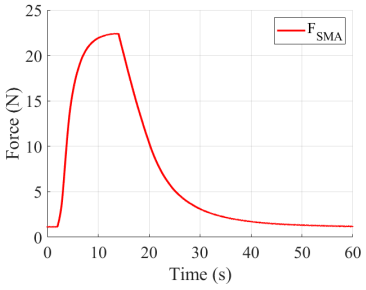

(f) Force at $\delta = 90mm$

Fig. 3.13 One set of experiments for coil sample 2 austenite characterization data

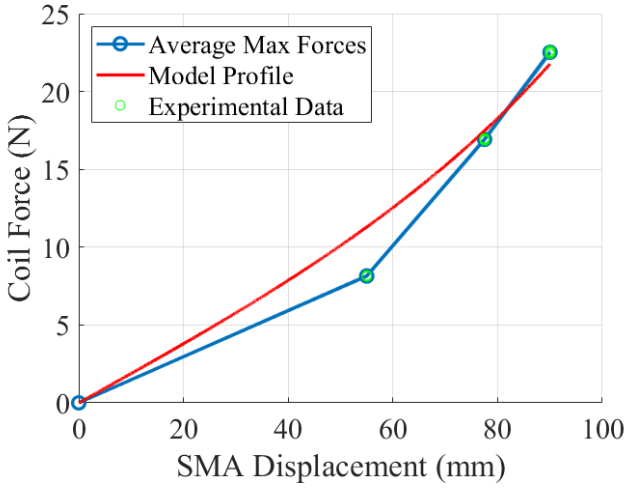

Fig. 3.14 Coil sample 2 austenite F-D characteristic

3.4.3 Coil 3 Profile

The third SMA coil test sample was tested for the martensite profile first. This martensite characteristic curve is shown in Figure 3.16(b). After obtaining the martensite data, the blocked force tests were conducted. It was decided to again start at $\delta = 0$ mm and work up towards $\delta = 90$ mm for this coil. For these tests, the input current was 1.7 A, with conduction periods of 8 to 10 seconds. The austenite test data for the third coil sample is shown in Figure 3.15, with the corresponding F-D curve in Figure 3.16(a).

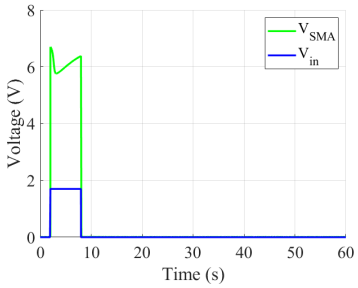

(a) Voltage at $\delta = 22.5mm$

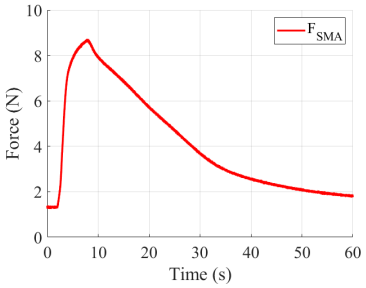

(b) Force at $\delta = 22.5mm$

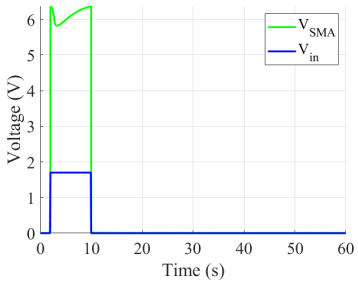

(c) Voltage at $\delta = 55mm$

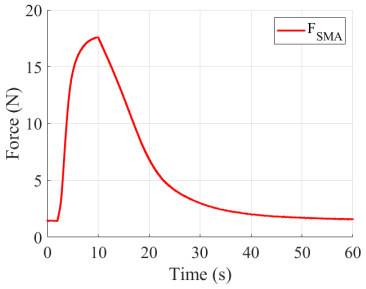

(d) Force at $\delta = 55mm$

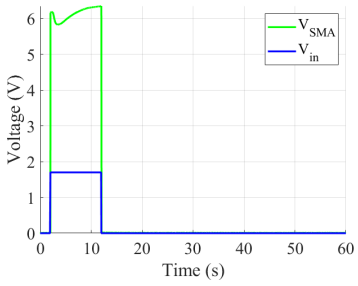

(e) Voltage at $\delta = 77.5mm$

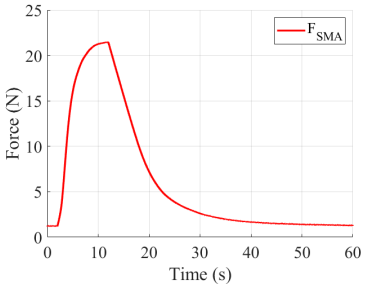

(f) Force at $\delta = 77.5mm$

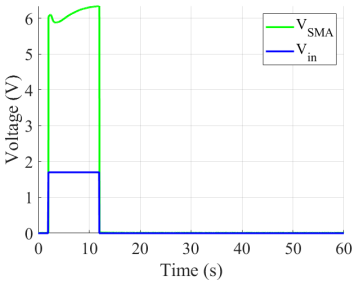

(g) Voltage at $\delta = 90mm$

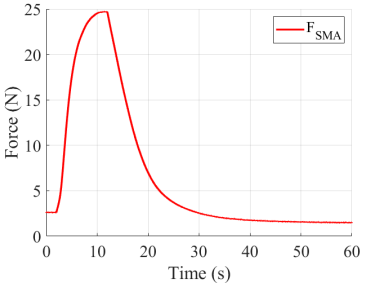

(h) Force at $\delta = 90mm$

Fig. 3.15 One set of experiments for coil sample 3 austenite characterization data

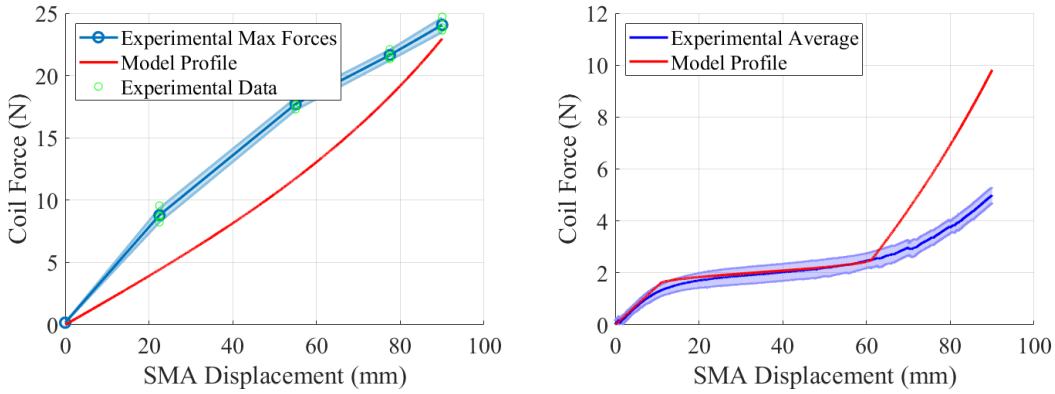

(a) Austenite (b) Martensite

Fig. 3.16 Coil sample 3 force-displacement profiles

3.5 SMA Coil Characterization Discussion

The experimental data from these characterization tests show some interesting SMA behaviour. The martensite force profiles have a sinusoidal shape, this is likely to be evidence of the detwinning process. In the literature, martensite detwinning is often represented mathematically as a sinusoidal function [2, 9, 10]. Within the framework of the Cho coil design model [2], the detwinning fraction ξ is represented as having a cosine region between two linear regions, bounded by the martensite critical stresses. The martensite profiles in Figures 3.12(b) and 3.16(b) show some agreement with this model, however they consistently deviate when the model exceeds the detwinning finish stress $\tau_{M_f}^{cr}$. It appears from inspection that the actual

SMA is still in the detwinning process up until around $\delta = 80$ mm. This is a clear indicator that there is a mismatch between the assumed nitinol coil material properties, and the actual properties of the coil samples.

As stated before, the mechanical properties of the SMA coils were not obtained during these experiments, but were taken from other sources with the same SMA wire and annealing technique [2]. It can be seen that the SMA design equations rely on knowledge of some of these parameters, mostly G_M and G_A, but is then mostly focused on coil geometry. Also for the austenite profile, inspection of F_A in equation 3.1 shows that the only material properties required for a force profile are G_A and Poissons ratio. In contrast, the martensite profile relies heavily on knowledge of material properties. In particular the coupling between ξ and τ_M is complex, and depends on the martensite critical stresses $\tau_{M_s}^{cr}$, $\tau_{M_f}^{cr}$, and residual strain γ_L. The investigation in [109] also found that the Liang model, which these F-D equations derive from, is very sensitive to parameter uncertainty. A thermomechanical investigation by Grandi et al. [43] found the relationship between material phase and shear stress to be more complex, with local martensite volume wavefronts that manifest and travel along the length of an SMA wire, rather than a homogeneous detwinning.

It is also known that SMA demonstrates strain rate dependant behaviour [43, 52, 61]. The Cho model used for design [2] is a static model, and does not consider

these strain rate effects. So it may not be fully appropriate to expect this model to match the quasi-static martensite data. Another aspect of this model is that the F-D curves are for 100% martensite and 100% austenite volumes. However, it is possible that the SMA coils during these austenite tests may have had local volumes of stress-induced martensite [43].

The blocked force data clearly shows the coil's force output dropping as the input current is halted, for example in Figure 3.15(h). This is due to the phase transition back to martensite as the SMA cools. The temperature of the SMA at this point depends on the current, and how long it was applied for, which varied slightly between tests. It can also be seen that the SMA cools faster at larger displacements, which is likely due to the increase in exposed surface area as the coil loops are stretched apart, which assists the ambient convective heat transfer. These observations can be used to assist in the derivation of the heat transfer dynamics described in Section 4.2.

The phase change behaviour from martensite to austenite can be observed through the SMA's changing voltage. During the austenite static tests the SMA voltage monitor shows some fluctuation during a constant current load, as shown in Figure 3.17. This indicates a change in the SMA electrical resistance, likely due to the solid phase change transformation. The local minimum in resistance at 3.6 seconds appears to coincide with an inflection point in the force profile at the same

time. This may indicate a second order relationship between the electrical resistance and the phase state. Similar to the detwinning observed in the martensite profile, it is very common to see a phase change state variable represented with a sinusoidal function. While the changing resistance does show this waveform, it is interesting to note the apparent change in wave amplitude and frequency, which is a more complex function than the common cosine representation. The voltage also appears to level off asymptotically with the coil force, indicating phase change completion.

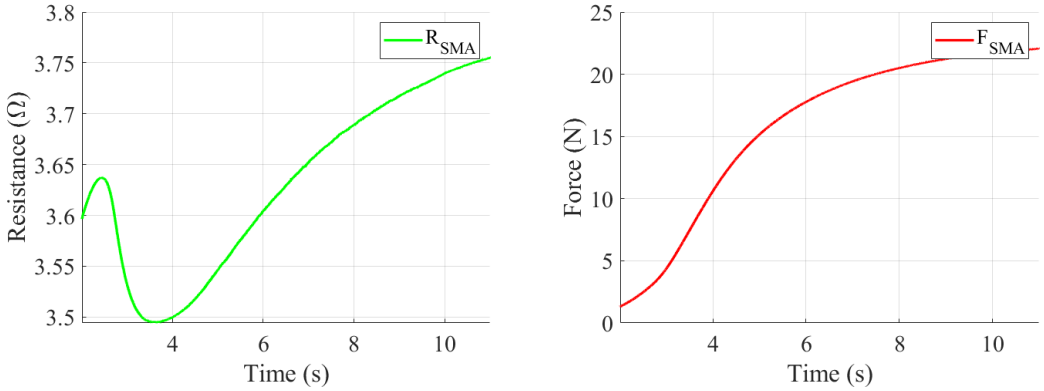

(a) SMA resistance during phase change (b) SMA force during phase change

Fig. 3.17 SMA during martensite to austenite phase transition

In summary, SMA behaviour is quite complex, and all actuator models come with inherent assumptions and simplifications. It is not expected for the experimental results to completely match the model predictions. However the experimental

data obtained is more than enough to form an actuator profile for the coil. This characterization allows for an integration with the F-D profiles already obtained for the compliant antagonist design. In addition, although there is slight deviation in the martensite force profiles, the coil design process relies on the austenite profile for the required force. The martensite F-D represents the passive profile, which affects the start point for the actuation stroke.

The austenite F-D profiles are not linear, but a linear approximation can be used to determine the coils active stiffness, or force-displacement trade off. This can be used for dynamic modelling of the actuator, and for establishing the force output of the SMA as it contracts and pulls on the finger. The martensite data can be used to determine the initial tension exerted by the SMA on the finger, as well as the equilibrium point after actuation as the finger biases the martensite coil.

4 Dynamic Modelling

This chapter discusses the dynamics of the compliant structure driven by the thermal activation of a SMA coil actuator. First the dynamics of the finger itself are derived from the Lagrangrian of the system. The SMA actuator dynamic model is derived from the heat transfer dynamics, phase transition, and the coil characterization data measured in Section 3.4. Simulations of the full system dynamics are used to predict the behaviour of the SMA integrated with its compliant antagonist.

4.1 Dynamics of a Serial 3R Chain With Elastic Joints

4.1.1 Lagrangian Dynamics Derivation

This section will derive the dynamics of a revolute serial chain subject to an end effector load. The same PRBM as in Chapter 2 is employed, with the flexible joints reduced to revolute pin joints located at the midpoint of the flexure length. The stiffness of the flexures is represented by assigning a torsional stiffness to each joint. The dynamics will be derived from a Lagrangian basis [110]. The Lagrangian

$\mathcal{L}$ is defined as

$$\mathcal{L} = T - \mathcal{P} \tag{4.1}$$

where T denotes the total kinetic energy of the system, and $\mathcal{P}$ denotes the total potential energy. For n generalized coordinates q_i the Lagrangian equations of motion are

$$\tau_i = \frac{d}{dt}\frac{\partial \mathcal{L}}{\partial \dot{q}_i} - \frac{\partial \mathcal{L}}{\partial q_i} \tag{4.2}$$

where τ_i denotes the i^{th} element of the $n \times 1$ vector containing the generalized forces and torques in the system. For a serial chain with three revolute joints, there are $n = 3$ generalized coordinates. The generalized coordinates for this system are defined here as the total angle between each link and the x axis of the base frame, as shown in Figure 4.1.

$$\begin{bmatrix} q_1 \\ q_2 \\ q_3 \end{bmatrix} = \begin{bmatrix} \theta_1 \\ \theta_1 + \theta_2 \\ \theta_1 + \theta_2 + \theta_3 \end{bmatrix} \tag{4.3}$$

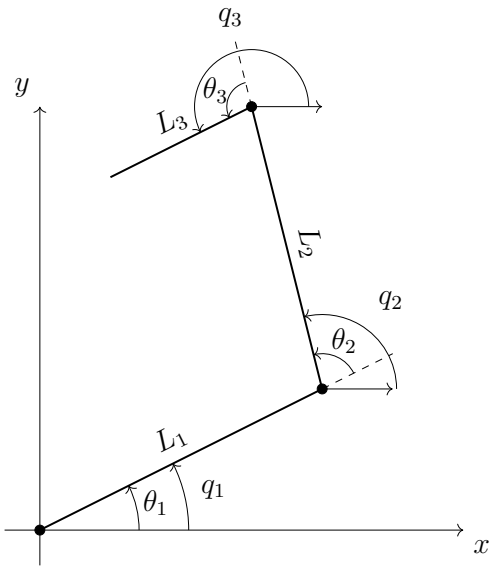

Fig. 4.1 Generalized coordinates for 3R dynamics

The center of mass (COM) of each link i is assumed to be at the midpoint of the link length L_i. Beginning with the forward kinematics, as derived in Section 2.2.1, the cartesian coordinates with respect to the inertial frame for each COM are

$$\begin{aligned} x_1 &= \frac{1}{2} L_1 \cos(q_1) \\ y_1 &= \frac{1}{2} L_1 \sin(q_1) \end{aligned} \tag{4.4}$$

$$\begin{aligned} x_2 &= L_1 \cos(q_1) + \frac{1}{2} L_2 \cos(q_2) \\ y_2 &= L_1 \sin(q_1) + \frac{1}{2} L_2 \sin(q_2) \end{aligned} \tag{4.5}$$

$$\begin{aligned} x_3 &= L_1 \cos(q_1) + L_2 \cos(q_2) + \frac{1}{2} L_3 \cos(q_3) \\ y_3 &= L_1 \sin(q_1) + L_2 \sin(q_2) + \frac{1}{2} L_3 \sin(q_3) \end{aligned} \tag{4.6}$$

The linear velocities for each of these components are

$$V_i = \sqrt{\dot{x}_i^2 + \dot{y}_i^2} \tag{4.7}$$

and the angular velocities are simply

$$\omega_i = \frac{d}{dt} q_i = \dot{q}_i \tag{4.8}$$

The kinetic energy for each link is the sum of the linear and angular kinetic energies

$$T_i = \frac{1}{2} m_i V_i^2 + \frac{1}{2} J_i \dot{q}_i^2 \tag{4.9}$$

where J_i indicates the mass moment of inertia for link L_i. Each link is rotating about the revolute joint at the link base. Thus, the rotating axis is at a distance of $\frac{L_i}{2}$ from the COM for each link. From the parallel axis theorem, the mass moment of inertia for short beams rotating at this distance is

$$J_i = \frac{m_i}{12}(L_i^2 + H^2) + \frac{1}{4} m_i L_i^2 \tag{4.10}$$

where H indicates the height of each link, as defined in Chapter 2, which is constant for all links.

The potential energy for the system consists of elastic potential energy terms U_e, as well as gravitational potential U_g

$$\mathcal{P} = U_e + U_g \tag{4.11}$$

The gravitational potential energies are defined with respect to the x axis of the base frame. Hence, the potential height for each COM is simply its vertical coordinate y_i

$$U_{g_i} = m_i g y_i \tag{4.12}$$

The elastic potential energy terms consider the joints as torsional springs, with stiffness K_i resisting the angular displacement between two links

$$U_{e_i} = \frac{1}{2} K_i (q_i - q_{i-1})^2 \tag{4.13}$$

where in the case of the first link, $q_1 - q_0 = q_1 - 0 = q_1$.

The Lagrangian can be assembled by first obtaining the linear velocities from the instantaneous rate of change of the cartesian coordinates. Beginning with the first link

$$\begin{aligned} V_1^2 &= \dot{x}_1^2 + \dot{y}_1^2 \\ &= \left(-\frac{1}{2} L_1 \sin(q_1) \dot{q}_1 \right)^2 + \left(\frac{1}{2} L_1 \cos(q_1) \dot{q}_1 \right)^2 \\ &= \frac{1}{4} L_1^2 \dot{q}_1^2 \end{aligned} \tag{4.14}$$

With the linear velocity expressed as such, the relation from equation (4.9) can be used to find the total kinetic energy of the first link

$$\begin{aligned} T_1 &= \frac{1}{2} \left(m_1 \frac{1}{4} L_1^2 \dot{q}_1^2 + J_1 \dot{q}_1^2 \right) \\ &= \frac{1}{2} \left(\frac{m_1}{4} L_1^2 + J_1 \right) \dot{q}_1^2 \end{aligned} \tag{4.15}$$

The gravitational potential energy for the first link is

$$U_{g_1} = m_1 g y_1 = m_1 g \frac{1}{2} L_1 \sin(q_1) \tag{4.16}$$

and the elastic potential energy is

$$U_{e_1} = \frac{1}{2} K_1 (q_1)^2 \tag{4.17}$$

so that the total potential energy is

$$\mathcal{P}_1 = \frac{1}{2} \left(K_1 q_1^2 + m_1 g L_1 \sin(q_1) \right) \tag{4.18}$$

This process is repeated for the second and third links. The intermediate calculations are tedious and will not be shown explicitly, but after much simplification the resulting energy terms for the second link are

$$T_2 = \frac{1}{2} \left(m_2 \left(L_1^2 \dot{q}_1^2 + \frac{1}{4} L_2^2 \dot{q}_2^2 + L_1 L_2 \dot{q}_1 \dot{q}_2 \cos(q_2 - q_1) \right) + J_2 \dot{q}_2^2 \right) \tag{4.19}$$

$$\mathcal{P}_2 = \frac{1}{2} K_2 \left(q_2 - q_1 \right)^2 + m_2 g \left(L_1 \sin(q_1) + \frac{1}{2} L_2 \sin(q_2) \right) \tag{4.20}$$

and for the third link are

$$\begin{aligned} T_3 = \frac{1}{2} \Bigg(m_3 \Bigg(& L_1^2 \dot{q}_1^2 + L_2^2 \dot{q}_2^2 + \frac{1}{4} L_3^2 \dot{q}_3^2 + 2 L_1 L_2 \dot{q}_1 \dot{q}_2 \cos(q_2 - q_1) \\ & + L_2 L_3 \dot{q}_2 \dot{q}_3 \cos(q_3 - q_2) + L_1 L_3 \dot{q}_1 \dot{q}_3 \cos(q_3 - q_1) \Bigg) + J_3 \dot{q}_3^2 \Bigg) \end{aligned} \tag{4.21}$$

$$\mathcal{P}_3 = \frac{1}{2} K_3 (q_3 - q_2)^2 + m_3 g \left(L_1 \sin(q_1) + L_2 \sin(q_2) + \frac{1}{2} L_3 \sin(q_3) \right) \tag{4.22}$$

Substituting the above energy terms into the Lagrangian from equation (4.1) gives

$$\begin{aligned}
\mathcal{L} &= (T_1 + T_2 + T_3) - (\mathcal{P}_1 + \mathcal{P}_2 + \mathcal{P}_3) \\
&= \frac{1}{2}\Bigg(\dot{q}_1^2\left(\frac{1}{4}m_1L_1^2 + J_1\right) + \dot{q}_1^2(m_2L_1^2) + \dot{q}_2^2\left(\frac{1}{4}m_2L_2^2 + J_2\right) \\
&+ m_2L_1L_2\dot{q}_1\dot{q}_2\cos(q_2 - q_1) + \dot{q}_1^2(m_3L_1^2) + \dot{q}_2^2(m_3L_2^2) \\
&+ \dot{q}_3^3\left(\frac{1}{4}m_3L_3^2 + J_3\right) + m_3L_2L_3\dot{q}_2\dot{q}_3\cos(q_3 - q_2) \\
&+ m_3L_1L_3\dot{q}_1\dot{q}_3\cos(q_3 - q_1) + 2m_3L_1L_2\dot{q}_1\dot{q}_2\cos(q_2 - q_1)\Bigg) \\
&- \frac{1}{2}\left(K_1q_1^2 + m_1gL_1\sin(q_1)\right) - \left(\frac{1}{2}K_2(q_2 - q_1)^2 + m_2g\left(L_1\sin(q_1) + \frac{1}{2}L_2\sin(q_2)\right)\right) \\
&- \left(\frac{1}{2}K_3(q_3 - q_2)^2 + m_3g\left(L_1\sin(q_1) + L_2\sin(q_2) + \frac{1}{2}L_3\sin(q_3)\right)\right)
\end{aligned} \tag{4.23}$$

At this point, the equations of motion can be derived from equation (4.2). The first equation is given by

$$\begin{aligned}
\tau_1 &= \frac{d}{dt}\frac{\partial\mathcal{L}}{\partial\dot{q}_1} - \frac{\partial\mathcal{L}}{\partial q_1} \\
&= \ddot{q}_1\left(J_1 + L_1^2\left(\frac{m_1}{4} + m_2 + m_3\right)\right) + \ddot{q}_2\left(L_1L_2\cos(q_2 - q_1)\left(\frac{m_2}{2} + m_3\right)\right) \\
&+ \ddot{q}_3\left(L_1L_3\cos(q_3 - q_1)m_3\right) \\
&+ \dot{q}_2^2\left(L_1L_2\sin(q_2 - q_1)\left(\frac{m_2}{2} + m_3\right)\right) + \dot{q}_3^2\left(L_1L_3\sin(q_3 - q_1)\frac{m_3}{2}\right) \\
&+ L_1g\cos(q_1)\left(\frac{1}{2}m_1 + m_2 + m_3\right) + K_1q_1 + K_2(q_2 - q_1)
\end{aligned} \tag{4.24}$$

The second equation of motion is given by

$$\begin{aligned}
\tau_2 &= \frac{d}{dt}\frac{\partial \mathcal{L}}{\partial \dot{q}_2} - \frac{\partial \mathcal{L}}{\partial q_2} \\
&= \ddot{q}_1\left(L_1 L_2 \cos(q_2 - q_1)\left(\frac{m_2}{2} + m_3\right)\right) + \ddot{q}_2\left(J_2 + L_2^2(\frac{m_2}{4} + m_3)\right) \\
&+ \ddot{q}_3\left(L_2 L_3 \cos(q_3 - q_2)\left(\frac{m_3}{2}\right)\right) \\
&+ \dot{q}_1^2\left(-L_1 L_2 \sin(q_2 - q_1)\left(\frac{m_2}{2} + m_3\right)\right) + \dot{q}_3^2\left(L_2 L_3 \sin(q_3 - q_2) m_3\right) \\
&+ L_2 g \cos(q_2)\left(\frac{m_2}{2} + m_3\right) + K_2(q_2 - q_1) + K_3(q_2 - q_3)
\end{aligned} \tag{4.25}$$

The third equation of motion is given by

$$\begin{aligned}
\tau_3 &= \frac{d}{dt}\frac{\partial \mathcal{L}}{\partial \dot{q}_3} - \frac{\partial \mathcal{L}}{\partial q_3} \\
&= \ddot{q}_1\left(L_1 L_3 \cos(q_3 - q_1) m_3\right) + \ddot{q}_2\left(L_2 L_3 \cos(q_3 - q_2)\left(\frac{m_3}{2}\right)\right) \\
&+ \ddot{q}_3\left(J_3 + L_3^2 \frac{m_3}{4}\right) \\
&+ \dot{q}_1^2\left(-L_1 L_3 \sin(q_3 - q_1)\left(\frac{m_3}{2}\right)\right) + \dot{q}_2^2\left(-L_2 L_3 \sin(q_3 - q_2)\left(\frac{m_3}{2}\right)\right) \\
&+ L_3 g \cos(q_3)\left(\frac{m_3}{2}\right) + K_3(q_3 - q_2)
\end{aligned} \tag{4.26}$$

The set of equations (4.24 - 4.26) describe the dynamics of the serial revolute chain. The three equations describe the resulting motion in terms of the angles q_i for the input torques τ_i. These can be sorted into the following matrix containers.

The mass matrix $\left[M\right]$ is of size $n \times n$, thus for an $n = 3$ system it is of size 3×3. The mass matrix contains the terms that have linear relations to the joint

accelerations $\ddot{q}_i$. This includes terms related to the link masses and inertias.

$$\big[M\big] = \begin{bmatrix} J_1 + L_1^2\left(\frac{m_1}{4} + m_2 + m_3\right) & L_1L_2\cos(q_1 - q_2)\left(\frac{m_2}{2} + m_3\right) & L_1L_3\cos(q_1 - q_3)\frac{m_3}{3} \\ L_1L_2\cos(q_1 - q_2)\left(\frac{m_2}{2} + m_3\right) & J_2 + L_2^2\left(\frac{m_2}{4} + m_3\right) & L_2L_3\cos(q_2 - q_3)\frac{m_3}{2} \\ L_1L_3\cos(q_1 - q_3)\frac{m_3}{2} & L_2L_3\cos(q_2 - q_3)\frac{m_3}{2} & J_3 + L_3^2\frac{m_3}{4} \end{bmatrix} \tag{4.27}$$

The stiffness matrix $\big[K\big]$ is also of size 3×3, and it contains the terms which have a linear relation to the joint angles q_i. These will be the terms related to the torsional stiffness of the joints.

$$\big[K\big] = \begin{bmatrix} K_1 + K_2 & -K_2 & 0 \\ -K_2 & K_2 + K_3 & -K_3 \\ 0 & -K_3 & K_3 \end{bmatrix} \tag{4.28}$$

The gravity matrix $\big[G\big]$, is of size 3×1 and contains the terms related to the gravitational potential energy of the system. These have no linear relation to the joint angles q.

$$\big[G\big] = \begin{bmatrix} L_1\cos(q_1)(\frac{m_1}{2} + m_2 + m_3) \\ L_2\cos(q_2)(\frac{m_2}{2} + m_3) \\ L_3\cos(q_3)\frac{m_3}{2} \end{bmatrix} \tag{4.29}$$

The matrix $\big[C\big]$ is called the centrifugal, or coriolos matrix. This 3×1 matrix contains the terms with joint velocity products, such as $\dot{q}_1\dot{q}_2$. These terms also have no linear relation to the joint angles.

$$\big[C\big] = \begin{bmatrix} -\dot{q}_2^2\left(L_1L_2\sin(q_2 - q_1)\left(\frac{m_2}{2} + m_3\right)\right) - \dot{q}_3^2\left(L_1L_3\sin(q_3 - q_1)\frac{m_3}{2}\right) \\ \dot{q}_1^2\left(L_1L_2\sin(q_2 - q_1)\left(\frac{m_2}{2} + m_3\right)\right) - \dot{q}_3^2L_2L_3\sin(q_3 - q_2)\frac{m_3}{2} \\ \dot{q}_1^2(L_1L_3\sin(q_3 - q_1)\frac{m_3}{2}) + \dot{q}_2^2(L_2L_3\sin(q_3 - q_2)\frac{m_3}{2}) \end{bmatrix} \tag{4.30}$$

With the above definitions, the dynamics can be expressed as

$$\begin{bmatrix} \tau_1 \\ \tau_2 \\ \tau_3 \end{bmatrix} = \big[M\big] \begin{bmatrix} \ddot{q}_1 \\ \ddot{q}_2 \\ \ddot{q}_3 \end{bmatrix} + \big[K\big] \begin{bmatrix} q_1 \\ q_2 \\ q_3 \end{bmatrix} + \big[C\big] + g\,\big[G\big] \tag{4.31}$$

4.1.2 Damping

The dynamics relation in equation (4.31) has no damping component. The undamped system will have free oscillation, with no energy dissipation. In reality there will be internal structural damping effects which attenuate the energy within the system. This can be modelled by introducing a Rayleigh damping term. Rayleigh damping is a form of viscous damping, which is proportional to the mass and stiffness of the system. Using a classical Rayleigh damping formulation, this is given by

$$\left[B\right] = \alpha \left[M\right] + \beta \left[K\right] \tag{4.32}$$

Where the damping matrix $\left[B\right]$ is related to the mass and stiffness matrices through the chosen coefficients α and β. These coefficients are related to the modal damping of the system ζ and the modal frequency ω.

$$\zeta = \frac{1}{2}\left(\frac{\alpha}{\omega} + \beta\omega\right) \tag{4.33}$$

The modal frequencies can be determined from a modal analysis of the mechanism, using finite element analysis tools such as Abaqus. For two given modes ω_1, ω_2, with corresponding damping conditions ζ_1, ζ_2, the corresponding damping

coefficients can be found by solving the following system

$$\begin{aligned} \zeta_1 &= \frac{1}{2}\left(\frac{\alpha}{\omega_1} + \beta\omega_1\right) \\ \zeta_2 &= \frac{1}{2}\left(\frac{\alpha}{\omega_2} + \beta\omega_2\right) \end{aligned} \tag{4.34}$$

For equal damping conditions, $\zeta_1 = \zeta_2$, this system reduces to

$$\begin{aligned} \frac{1}{2}\left(\frac{\alpha}{\omega_1} + \beta\omega_1\right) &= \frac{1}{2}\left(\frac{\alpha}{\omega_2} + \beta\omega_2\right) \\ \zeta_1 &= \frac{1}{2}\left(\frac{\alpha}{\omega_1} + \beta\omega_1\right) \end{aligned} \tag{4.35}$$

which allows for the damping coefficients to be computed for a given damping ratio. With the damping matrix formulated, the full equations of motion for the 3R finger mechanism are

$$\tau = M\ddot{q} + B\dot{q} + Kq + C + gG \tag{4.36}$$

4.1.3 Simulation

As detailed in Chapter 2, the joints in the structure are designed with an appropriate stiffness to hold equilibrium for a specified pose and load. The quasi-static analysis and experiments from that chapter validated these joint stiffnesses. Now the derived dynamic representation can be investigated to see if it shows similar results.

The dynamics of the 3R mechanism is simulated using MATLAB/Simulink. A forward dynamics function is used to calculate the joint accelerations $\ddot{q}(t)$ for the

input torque vector $\tau(t)$ and state feedback for $q(t)$ and $\dot{q}(t)$. The block diagram for this model is shown in Figure 4.3. The equations of motion stated in equation (4.36) was populated with the properties for the 15 N finger design from Section 2.3. The damping properties were obtained for a critically damped condition using Abaqus, as summarized in Table 4.1. This damping analysis was conducted with the finger in an unflexed, neutral state. As such, in the forward dynamics function the damping matrix B is defined with respect to M at $q = 0$, and is not updated dynamically.

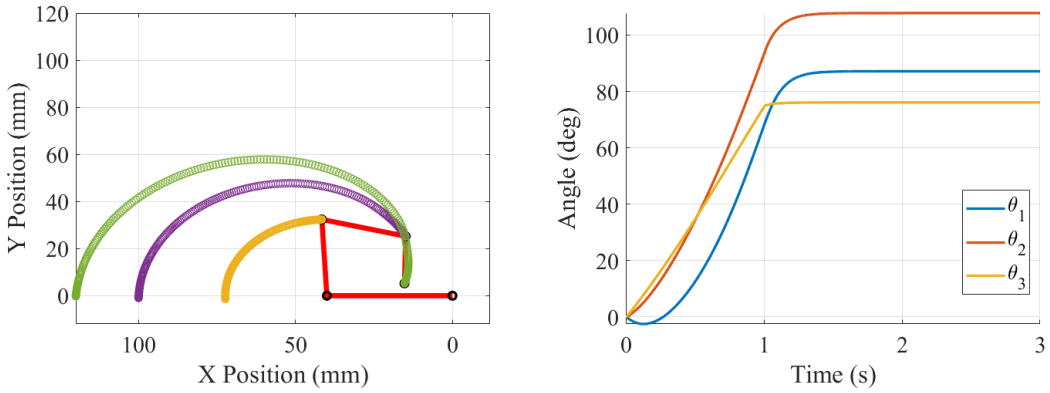

(a) Motion of finger in XY-plane

(b) Joint space

Fig. 4.2 Simulated trajectory for 15 N finger

Table 4.1 Finger damping parameters with Ultimaker TPU 95A

Parameter	Value
α	396.49
β	$1.893 \cdot 10^{-3}$
ζ	1

The simulation applies an input torque to the third joint with an equivalent moment to a 15 N load applied to the end effector, ramping from zero to the full load in one second. The simulated trajectory is shown in Figure 4.2(a), with the motion of the individual joint angles shown in Figure 4.2(b). The mechanism is in static equilibrium with the end effector coordinates (15.25 mm, 5.27 mm), with respect to the base frame. There is some slight deviation from the static model, in which these stiffnesses are designed to hold the end effector at $(15, 6)$ mm. The end effector coordinates between the static and dynamic model are quite close. This is not surprising, since the PRBM representation is identical to the one used for the flexure design in the static analysis.

Now that the dynamics of the mechanism has been defined, the dynamics of the actuator can be included to identify its effect on the system.

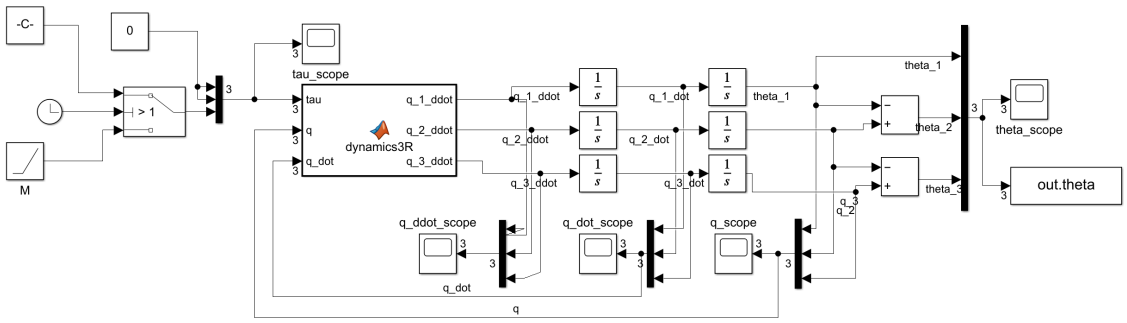

Fig. 4.3 Simulink model for finger dynamics

4.2 SMA Dynamics

The SMA coil is heated from the Joule heating of the current conducted along its wire length. The power generated by the resistance of the wire, in the form of thermal energy per unit time is

$$P = i^2(t)R \tag{4.37}$$

this power is dissipated via convection to the surrounding environment through the exposed surface area A of the wire, with the temperature gradient between the wire T and the environment T_{amb}

$$Q = Ah(T - T_{amb}) \tag{4.38}$$

where h is the convective heat transfer coefficient. Treating the wire as a cylindrical body with diameter d_o and length L_o, the lateral surface area is given by

$$A = \pi d_o L_o \tag{4.39}$$

The net heat flow will be the difference between the power generated by Joule heating, and the heat dissipated to the environment

$$\begin{aligned} \Phi &= P - Q \\ \Phi &= i^2(t)R - \pi d_o L_o h(T - T_{amb}) \end{aligned} \tag{4.40}$$

The thermal energy from the net heat flow will affect the temperature of the wire, according to its mass m and specific heat c.

$$\Phi = mc\dot{T} \tag{4.41}$$

the mass can be re-expressed in terms of the wires density ρ and cylinder geometry

$$m = \rho\frac{\pi d_o^2 L_o}{4} \tag{4.42}$$

which can now be substituted into equation (4.41) to get the expression for wire heating

$$\Phi = \frac{1}{4}\rho c\pi d_o^2 L_o\dot{T} \tag{4.43}$$

Now the net heat flow from equation (4.40) and the wire heating from equation (4.42) can be equated to give the heat transfer relationship

$$\frac{1}{4}\rho c\pi d_o^2 L_o\dot{T} = i^2(t)R - \pi d_o L_o h(T - T_{amb}) \tag{4.44}$$

Some of these parameters can be determined from the design of the SMA coil, and from its characterization data. For example the heat transfer coefficient h can be estimated from the cooling times observed in Section 3.4. Other values, such as the heat capacity, are given by the alloy manufacturer [1]. The values used for these parameters in the simulation are listed in Table 4.2

The solid to solid phase transition between martensite and austenite will be triggered through heating of the SMA. Considering the phase change from martensite to austenite, the process will begin once the SMA temperature reaches the

Table 4.2 Heat transfer parameters for the SMA

Parameter	Value	Units
T_{amb}	293	K
R	3.8	Ω
h	100	$W/m^2 \cdot K$
c	836.8	$J/kg \cdot K$
ρ	6450	kg/m^3
T_{As}	70	K
T_{Af}	90	K

austenite start temperature T_{As}, and will be complete as the temperature reaches the austenite finish temperature T_{Af}.

Similar to the Liang model, an austenite activation parameter ϵ_a is introduced. This indicates the transformation state of the SMA, where $\epsilon_a = 0$ indicates full martensite and $\epsilon_a = 1$ indicates full austenite. This activation parameter follows a cosine function during the phase change process, as in [10]

$$\epsilon_a = \begin{cases} 0, & \text{for } T < T_{As} \\ \frac{1}{2}\left(1 - \cos\left(\pi \frac{T - T_{As}}{T_{Af} - T_{As}}\right)\right), & \text{for } T_{As} \leq T \leq T_{Af} \\ 1, & \text{for } T > T_{Af} \end{cases} \tag{4.45}$$

The force output of the SMA depends on a number of factors. The maximum actuator force will depend on the phase state of the material. For a given displacement, the SMA will generate a minimum force at full martensite, and a maximum force at full austenite. A linear relationship can be assumed between the force

output and the phase, using the activation parameter ϵ_a

$$F = \epsilon_a F_{Au} \tag{4.46}$$

where F_{Au} is the maximum austenite force of the SMA for a given displacement.

There is a force-displacement trade off in the actuator profile. As discussed in Chapter 3, the austenite force output of the SMA drops as it recovers from deformation and approaches its memorized length. This is also experimentally shown in the SMA characterization tests, for example the coil 2 austenite profile in Figure 3.14. Therefore the actual force output of the SMA actuator will be a function of its displacement as well as the extent of phase transition. The force-displacement trade off can be modelled by introducing an active stiffness term $k\Delta\delta$ that describes the force-displacement curve of the SMA coil actuator

$$F = \epsilon_a F_{Au} - k\Delta\delta = \epsilon_a F_{Au} - k(\delta_{max} - \delta) \tag{4.47}$$

where k is the active stiffness of the SMA coil, and $\Delta\delta$ represents the extent of the actuation stroke from a maximum deflection δ_{max}. Therefore this model takes the maximum austenite force F_{Au} as the force at deflection $\delta = \delta_{max}$.

The active stiffness can be identified from the austenite force-displacement profile as the slope of a first order line. Taking the characterization data from Section 3.4 an average linear F-D curve can be found, as shown in Figure 4.4. The average

maximum force at $\delta = 90$ mm is $F_{Au} = 23.0886$ N. This gives an active stiffness of

$$k = \frac{23.0886N}{90 \cdot 10^{-3}m} = 256.54N/m \tag{4.48}$$

Thus, the actuator dynamics of the SMA coil are described. The input current $i(t)$ heats the SMA according to the heat transfer relationship in equation (4.44), where the temperature of the SMA will induce phase transition according to equation (4.45), which controls the SMA force output according to (4.47).

4.3 Dynamics of The Complete Integrated Mechanism

The activated SMA will pull on the end effector as it attempts to restore its memorized contracted length. This linear force is transmitted along the tendon to the mounting point on the end effector. Due to the tendon being mounted at a distance away from the neutral axis of the third link, this creates a moment arm from the line of action of the SMA to the third joint. Thus the output force of the SMA is applied to the mechanism as a torque

$$\begin{bmatrix} \tau_1 \\ \tau_2 \\ \tau_3 \end{bmatrix} = \begin{bmatrix} 0 \\ 0 \\ Fd \end{bmatrix} \tag{4.49}$$

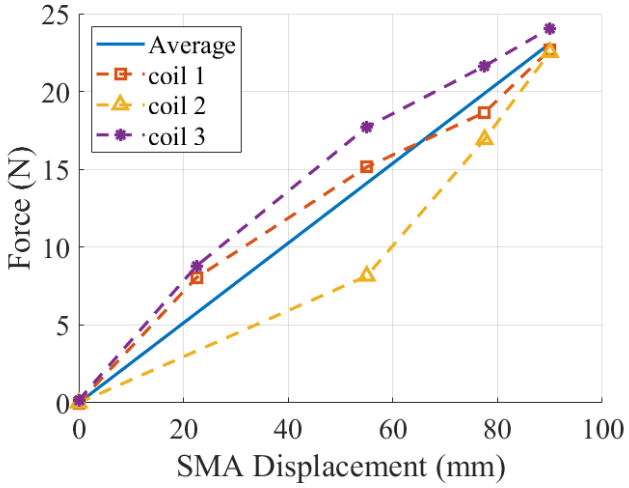

Fig. 4.4 Coil austenite F-D trade offs, with average profile

From the geometry of the structure, this moment arm distance d will run from the height of the routing hole to the midpoint of the flexure thickness.

$$\begin{bmatrix} \tau_1 \\ \tau_2 \\ \tau_3 \end{bmatrix} = \begin{bmatrix} 0 \\ 0 \\ F\left(H_r - \frac{t}{2}\right) \end{bmatrix} \tag{4.50}$$

where H_r is the height of the routing hole, and t indicates the beam flexure thickness, as illustrated in Figure 2.4.

This joint torque vector is what will drive the equations of motion for the finger mechanism in equation (4.36). This allows for the dynamics of the SMA actuator to couple into the motion of the finger mechanism, for a complete integrated dynamic model.

4.3.1 Simulated Results

A model of the full dynamics is created using Matlab/Simulink. The input to this model is the current $i(t)$ which will be conducted along the SMA coil. As the Simulink block diagram in Figure 4.5 shows, separate dynamics functions are used for the SMA heating and force output. The force output of the SMA is fed into the dynamics of the 3R mechanism, according to equation (4.50). The joint angle states are used to calculate the extent of SMA stroke, based on the bending of each flexure joint, which feeds back into the SMA force. The dynamic parameters of the 3R finger mechanism was populated with the 15 N finger design from Table 2.1, and the SMA actuator dynamics is based on the characterization data, as described in Section 4.2. It is assumed that the SMA is mounted in a fully martensite state that has been stretched out to the maximum with an initial displacement of $\delta_{max} = 90mm$.

The simulation is run with an input current step of 2 A, applied for eight seconds. During this time the SMA heats rapidly, as shown in Figure 4.7(b). Once the SMA

Table 4.3 End effector equilibrium positions

Model	Q_x (mm)	Q_y (mm)
3R Quasi-Static	15	6
3R Dynamic	15.26	5.27
SMA Integrated Dynamic	10.25	16.35

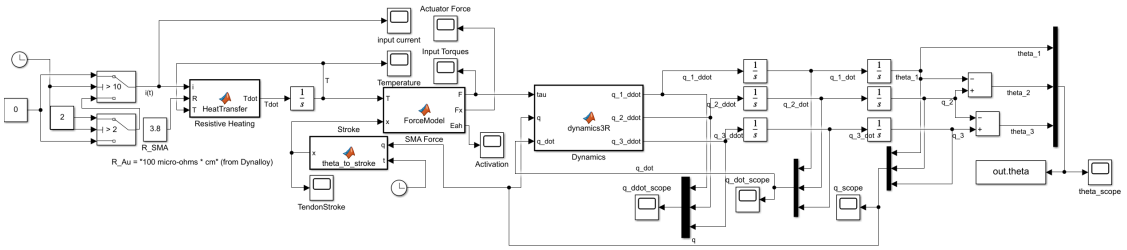

Fig. 4.5 Simulink model for complete system dynamics

temperature exceeds the T_{A_s} threshold the phase change process begins, as shown more closely in Figure 4.8(b). The SMA force increases with the phase transition to austenite, actuating the finger and driving the joint angles in Figure 4.7(f). It can be seen that the output force of the SMA rapidly increases until it peaks, and then decreases until settling. This is shown more closely in Figure 4.8(c). This is due to both the active stiffness of the SMA causing a force dropoff, and the increase in finger resistance as it is pulled beyond the designed-for equilibrium point. The effect of pulling beyond equilibrium can also be clearly seen in Figure 4.8(d), as the θ_3 profile resembles an overshoot before settling at steady state.

As shown in Figure 4.6(a), the system reaches equilibrium when the resistance of the finger joints balance with the SMA output force. The position of the end effector here is (10.25 mm, 16.35 mm) mm. This is very different than the dynamic results of the 3R mechanism alone. The different end effector equilibrium positions for these models are summarized in Table 4.3. This is because the system reaches equilibrium at an SMA force of $F = 13.32$ N. This is the point where, due the

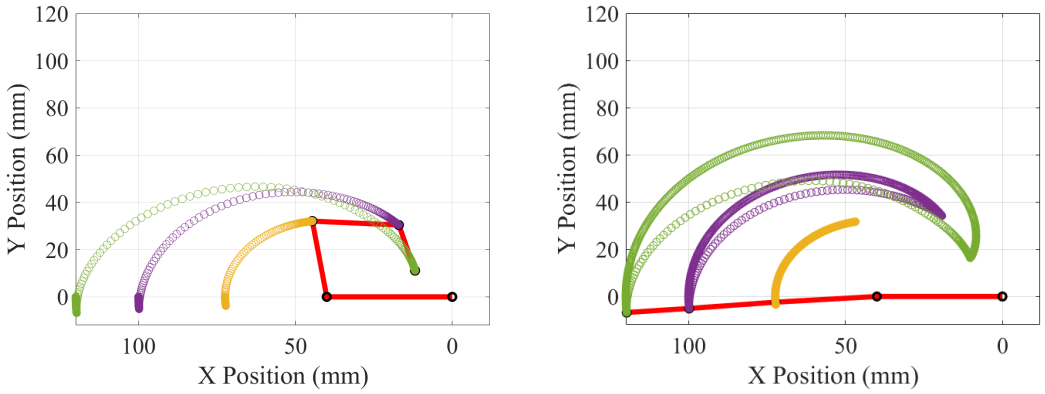

(a) At equilibrium (b) After biasing

Fig. 4.6 Simulated trajectory for thermally activated SMA pulling finger

actuator force-displacement trade off, the SMA is not able to output quite enough force at this deflection to pull the finger any further.

The simulation shows the SMA temperature is saturated beyond T_{A_f}, and so it takes several seconds for the SMA to begin transitioning back to martensite after the input current is stopped. The SMA gradually cools through radiation to the environment. As the SMA transitions to martensite, the force output also rapidly drops, and the resistance of the joints in the finger mechanism become dominant. The trajectory of the finger as it biases the SMA is shown in Figure 4.6(b).

The dynamic model results show that the integration of the SMA with the finger structure will lead to different behaviour than was seen with the static model. This allows us to predict the behaviour of an integrated test, and plan accordingly.

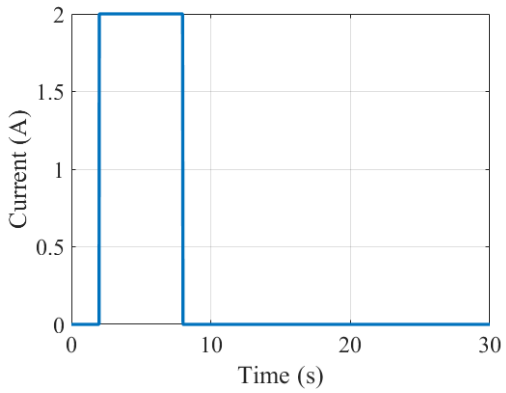

(a) Input current

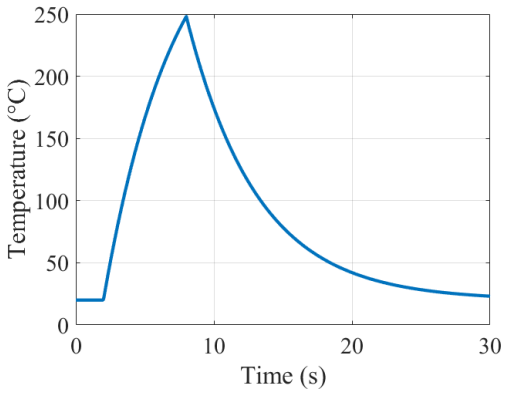

(b) SMA temperature

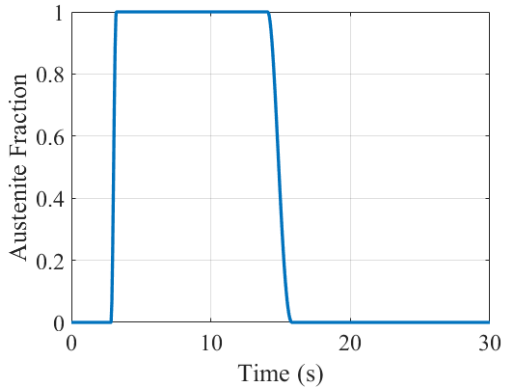

(c) Activation parameter

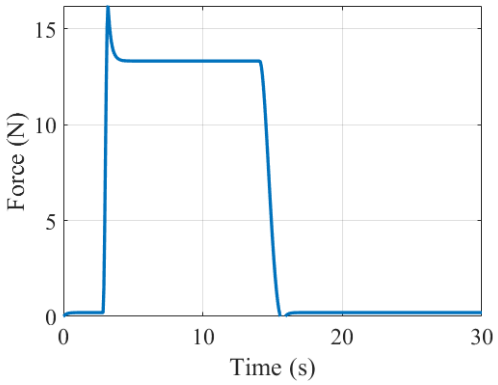

(d) SMA output force

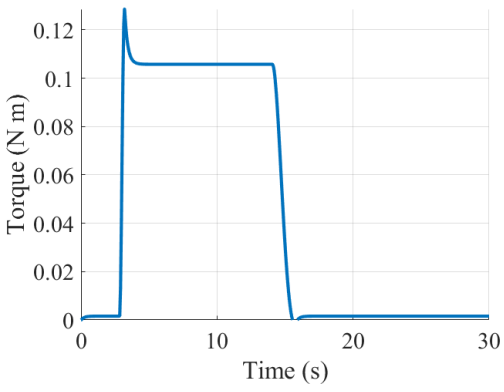

(e) Applied torque by SMA

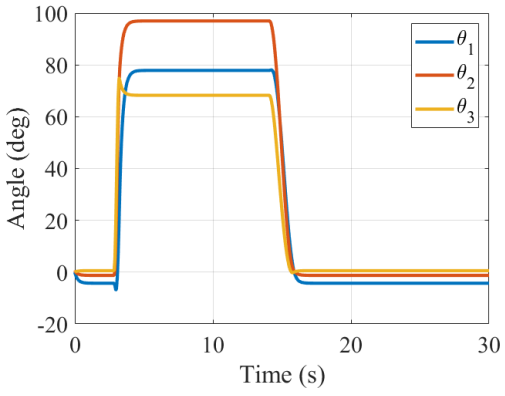

(f) Joint angles

Fig. 4.7 Integrated SMA-finger dynamic simulation results

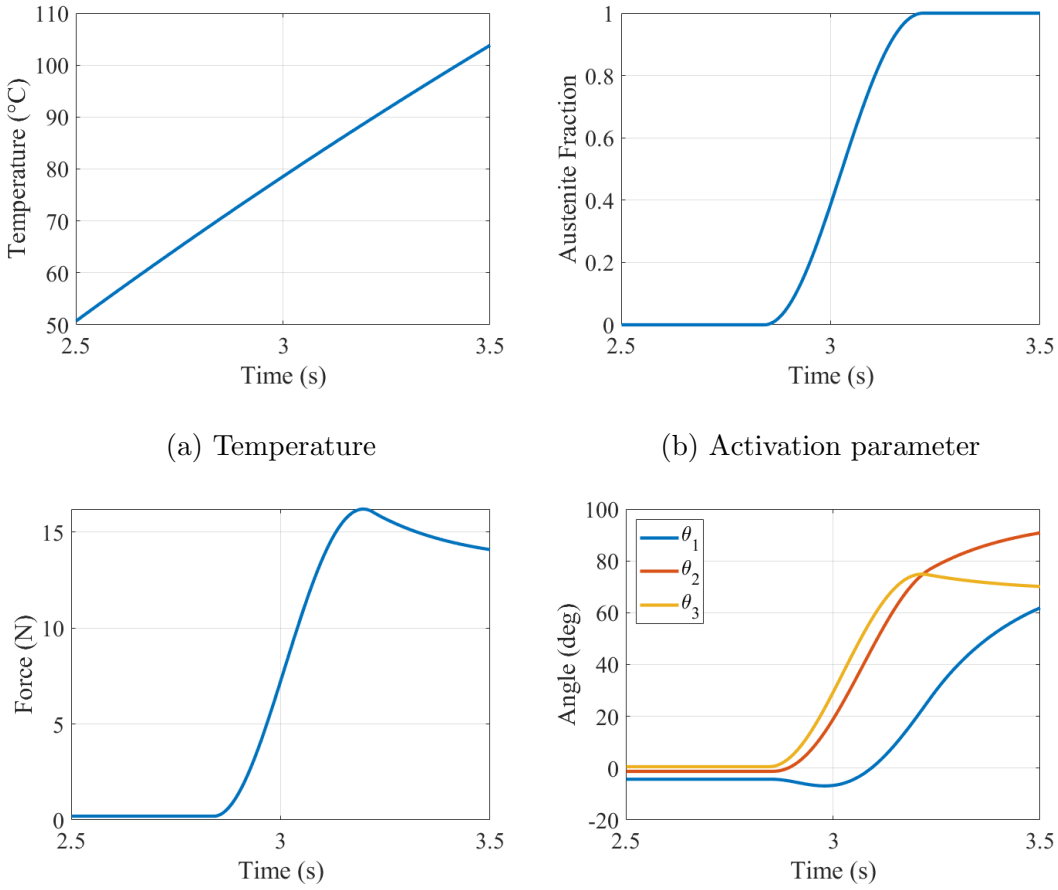

(a) Temperature

(b) Activation parameter

(c) SMA output force

(d) Joint angles

Fig. 4.8 Simulation results during SMA activation period

Rather than attempting to re-design the actuator, it will be much simpler to use these results to re-design the finger structure. That is to say, we can use the static model developed in Chapter 2 to re-design to passive structure to match the actuator. Of course this simulation has some major assumptions and simplifications, for example this model takes the resistance of the SMA to be static, rather than a

changing resistance which would affect the heat transfer behaviour. Also the SMA force in this simulation does not account for the martensite force component, which will change the biasing distance. In addition, this model uses a PRBM representation, and of course the physical mechanism will have long flexible joints, which may lead to some different end effector positions. In any case, these results shall act as a baseline for the final design iterations of the final assembly.

5 Integration of the SMA Actuator and Compliant Finger

This chapter discusses the integration of the SMA coil actuator with the compliant antagonist robotic finger mechanism. The design of the finger is revisited to improve performance, to incorporate the actuator profile of the SMA coil, and to accommodate for the predicted behaviour shown in the dynamic model simulations. The final design is manufactured and assembled with the SMA acting as an artificial muscle. High-speed camera footage of the robotic finger is used to evaluate the performance of the final design.

5.1 Final Compliant Finger Design

The finger designs from Chapter 2 acted as a baseline design. Now with knowledge of the SMA actuator profile from Chapter 3, and the predictions of the integrated system dynamics from Chapter 4, the passive structure can be redesigned to better match the actuator.

First, looking at the actuator force output in Figure 4.7(d), it is observed that the SMA actuator balances with the joint stiffnesses at 13.1 N. This simulation was run with the 15 N finger design, but the end effector is not quite closed down at the desired position as the austenite SMA can not produce high enough forces at that displacement to pull the tendon the remaining amount. Therefore the finger can be re-designed for a 13 N end effector load at close, to account for the F-D tradeoff of the actuator.

In addition, it may be desirable to increase the flexure lengths of the finger. Where previously the flexure lengths were calculated for the minimum required joint angles, observations during additional testing has shown how the 3D print resolutions may reduce the actual flexure length. Link boundaries coming into contact too soon lock down the mechanism and prevent further flexure bending. In addition, having increased flexure length allows for the possibility of increased bending curl. As a gripper, it is beneficial to have additional bending available for the manipulator to adapt to different objects. The additional flexure length is achieved by adding a static flexure length offset to the algorithm described in Section 2.3. However, as explored in Section 2.2.6, the flexible members being too long may impact the desired pose approximation. Therefore a small length offset such as 0.5 mm is chosen for each flexure

$$L_{f_i} = (H - t_i) \cdot \theta_i + 0.5mm \tag{5.1}$$

It is also necessary to consider the joint stresses during bending. The stress σ in a beam bending with a moment load is given by

$$\sigma = \frac{My}{I} \tag{5.2}$$

where M is the bending moment about the beams neutral axis, I is the moment of inertia for the beam cross section about the neutral axis, and y is the distance from the neutral axis to a point on the beam. From this formula, the maximum stresses in the flexures will be at the top and bottom flexure faces, where the beam is in full compression or tension. For these beam flexures, the moment arm can be expressed as half of the flexure thickness $y = t/2$. The beam moment can also be expressed in terms of the end effector actuator force and the distance from the routing hole to flexure midpoint $M = F(H_r - t/2)$. This gives the maximum flexure stress as

$$\sigma_{max} = \frac{6Ft(H_r - t/2)}{wt^3} \tag{5.3}$$

The material used for this compliant mechanism will again be TPU 95A from Ultimaker. The manufacturer specifies the yield stress for this material as 8.6 MPa. Therefore it is desirable to design the finger such that the maximum joint stresses remain below this yield point. Considering the stress relation in equation (5.3), it

is seen that for a given flexure thickness and actuator force the beam stress can be reduced by decreasing the routing hole height or increasing the width of the beam.

However, this design process is iterative. As discussed in Chapter 2, there is a recursive relationship between many of these parameters. Altering the routing hole height or beam width according to equation 5.3, or the flexure length according to equation (5.1) will all affect the joint stiffnesses and other design parameters. In addition, the design of the finger for aesthetic reasons is still desired to be relatively anthropomorphic, which restricts the design from being overly wide or tall.

With all of these additional design considerations, the compliant finger design was tweaked several times before settling on a final design. This design slightly increased the width of the entire mechanism to reduce the joint stresses, and in proportion it slightly increased the height of the links and routing hole to avoid overly long flexures. This is meant to balance a 13 N load from the SMA in a closed down end effector position. The parameters for the final design are listed in Table 5.1. The model was printed using an Ultimaker S5 3D-printer, with measurements of the manufactured part presented in Table 5.2.

5.1.1 Compliant Antagonist Profile

The force-displacement profile of the redesigned finger mechanism was obtained using a similar experimental setup to that described in Chapter 2. The resulting

Table 5.1 Design parameters for compliant finger

Parameter	Value
F	13 N
Q_x	15 mm
Q_y	6 mm
Θ	270 deg
H	11 mm
w	18 mm
t_1	2.088747 mm
t_2	2.084393 mm
t_3	2.091766 mm
L_{f_1}	13.978551 mm
L_{f_2}	17.100158 mm
L_{f_3}	12.418647 mm

Table 5.2 3D-printed finger measurements

Dimension	Measurement
t_1	2.068 $\pm$ 0.0075 mm
t_2	2.077 $\pm$ 0.0225 mm
t_3	2.055 $\pm$ 0.0138 mm
L_{f_1}	14.098 $\pm$ 0.1586 mm
L_{f_2}	17.103 $\pm$ 0.1804 mm
L_{f_3}	12.668 $\pm$ 0.1895 mm

F-D curve for this design is presented in Figure 5.1(a). The experimental results show that the finger consistently closes down at 12.71 N. The F-D profile still shows the same hysteresis behaviour, with a significant drop in force during the return segment.

The integration of the compliant finger and the SMA coil is designed with the hysteresis profiles of both the actuator and the antagonist in mind. As shown in

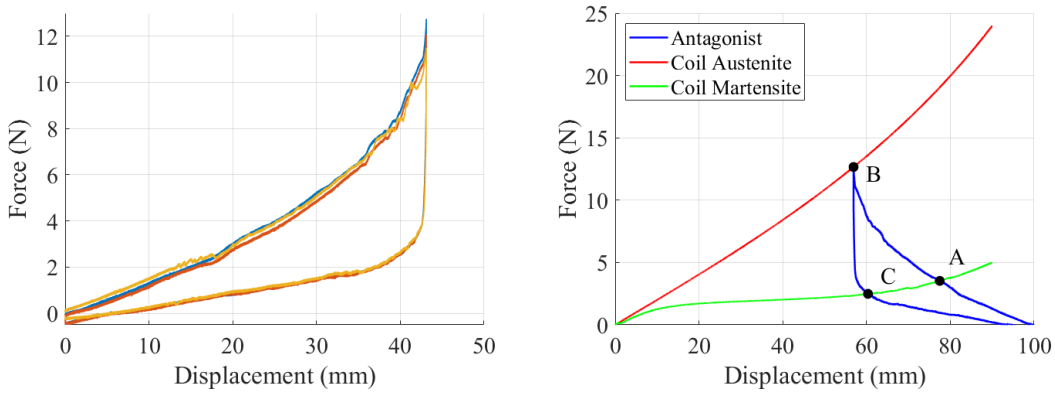

(a) Experimental force-displacement profile for final finger design

(b) Hysteresis matching of antagonist profile with experimental SMA F-D profiles

Fig. 5.1 Antagonist F-D characteristic and expected hysteresis matching

Figure 5.1(b), there will be three distinct equilibrium points during the actuation cycle, labelled as A, B, and C. The initial state before actuation is marked as A, where the martensite force is expected to be dominant and pull on the finger until the actuator and antagonist are in equilibrium at point A. The phase change of the SMA to austenite will actuate the finger to point B, where the antagonist and actuator are again at an equal force-displacement point. After actuation is complete and the SMA cools back to martensite, the hysteresis in the antagonist will result in a different intersection point with the martensite curve. This point C will be the mechanism state after biasing is completed.

5.2 Experimental Setup

The integration test is conducted with the SMA coil actuator mounted to the robotic finger. The SMA coil is connected to the tendon through a floating isolation mount, as shown in Figure 5.2(a). The coil loops through a short aluminum tube in the mount, which keeps the tendon electrically isolated from the SMA, and prevents the SMA from melting into the mount casing. The end of the SMA are connected to binding posts on a ThorLabs NRT 100/M motorized stage. The compliant finger is mounted in line with the stage, with the tendon running from the SMA connection to the end effector. The connections are done with no displacement of the SMA coil while maintaining tension in the tendon. Using the motorized stage the SMA is displaced to $\delta = 90$ mm, with the finger constrained to ensure SMA deflection and prevent motion in the finger as shown in Figure 5.2(b).

Similar to the experimental setup described in Chapter 3, the input current to the SMA is controlled by the Speedgoat IO133 module via a custom made voltage to current circuit board. Voltage monitors on the PCB measure the voltage across the SMA during the experiment. A Chronos 2.1 high-speed camera from Krontech is mounted parallel to the experimental setup, as seen in Figure 5.3. The high-speed camera is controlled by the Speedgoat, such that the video footage is synchronized with the experiment. The video is recorded at 240 frames per second, with a

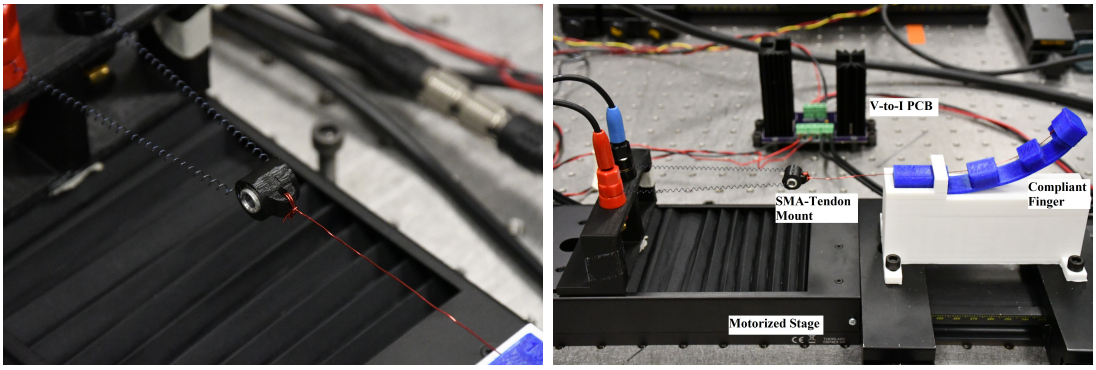

(a) SMA to tendon connection (b) Experimental components labelled

Fig. 5.2 Integration test experimental setup

resolution of 1920×1080 pixels. The high-speed video is then used with a Matlab motion tracking script to output the trajectory of the finger links and SMA coil.

5.3 Experimental Results

The initial tension from the SMA before actuating leaves the end effector at a position of (101.97 mm, 38.76 mmm) and orientation of $\Theta = 57°$, which corresponds to a tendon pull of 11.1 mm for the finger. Therefore the initial displacement for the SMA in martensite is $\delta_M = 90 - 11.1 = 78.9$ mm, which matches closely with position A in Figure 5.1(b). The SMA is thermally activated by conducting 1.7 A of current for 3 seconds, beginning at initial time $t = 0$. Video footage shows that the SMA begins contracting almost immediately upon conduction of current. Time lapse images of the experiment are provided in Figure 5.5, and a trajectory of the

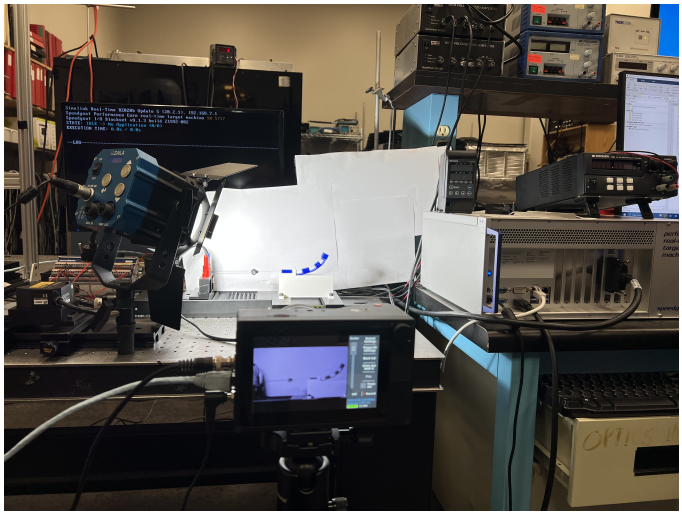

Fig. 5.3 High-speed camera view of experimental setup

finger mechanism is shown in Figure 5.4(a). The SMA coil continues to actuate the finger until $t = 3.25$ seconds (0.25 seconds after the current has been shut off), where the stiffness of the joints balance with the SMA actuator. A summary of the experimental results is provided in Table 5.3.

Motion tracking of the SMA-to-tendon mount allows for accurate measurement of the SMA stroke during the experiment, shown in Figure 5.4(b). The SMA coil

Table 5.3 Summary of integration test results

Parameter	Value
Actuation Stroke	33.39 mm
Bias Distance	15.17 mm
Activation Time	3.25 s
Cooling Time	8.10 s
(Q_x, Q_y)	(8.27 mm, 13.02 mm)
Θ	248.52°

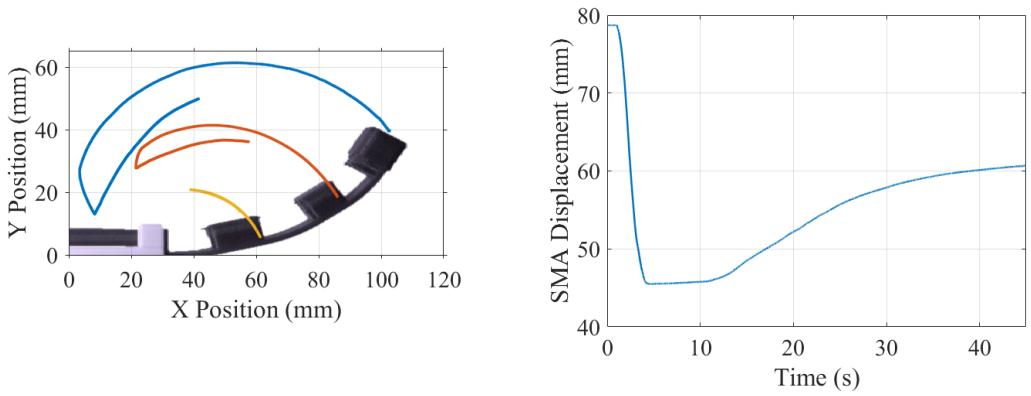

(a) Trajectory of finger in XY plane (b) Actuator displacement over time

Fig. 5.4 Motion tracking of finger and SMA during the integration test

pulls the mechanism from an initial martensite displacement of $\delta_M = 78.9$ mm to a final austenite displacement of $\delta_A = 45.51$ mm, resulting in an actuation stroke of $\delta_{stroke} = 33.39$ mm. This matches closely with the predicted stroke from equilibrium points A to B shown in Figure 5.1(b). The initial 11 mm displacement combined with the 33 mm actuation stroke results in a total linear displacement of 44.39 mm for the compliant finger, which is slightly over the designed close stroke of 43.79 mm for this finger design. The results show that the finger mechanism reaches an end effector position of (8.27 mm, 13.02 mm) with respect to the base frame, with an orientation of $\Theta = 248.52°$. This has some slight position error with the designed end effector coordinates of (15 mm, 6mm, 270°).

After actuation, the mechanism is held in the grip position for several seconds.

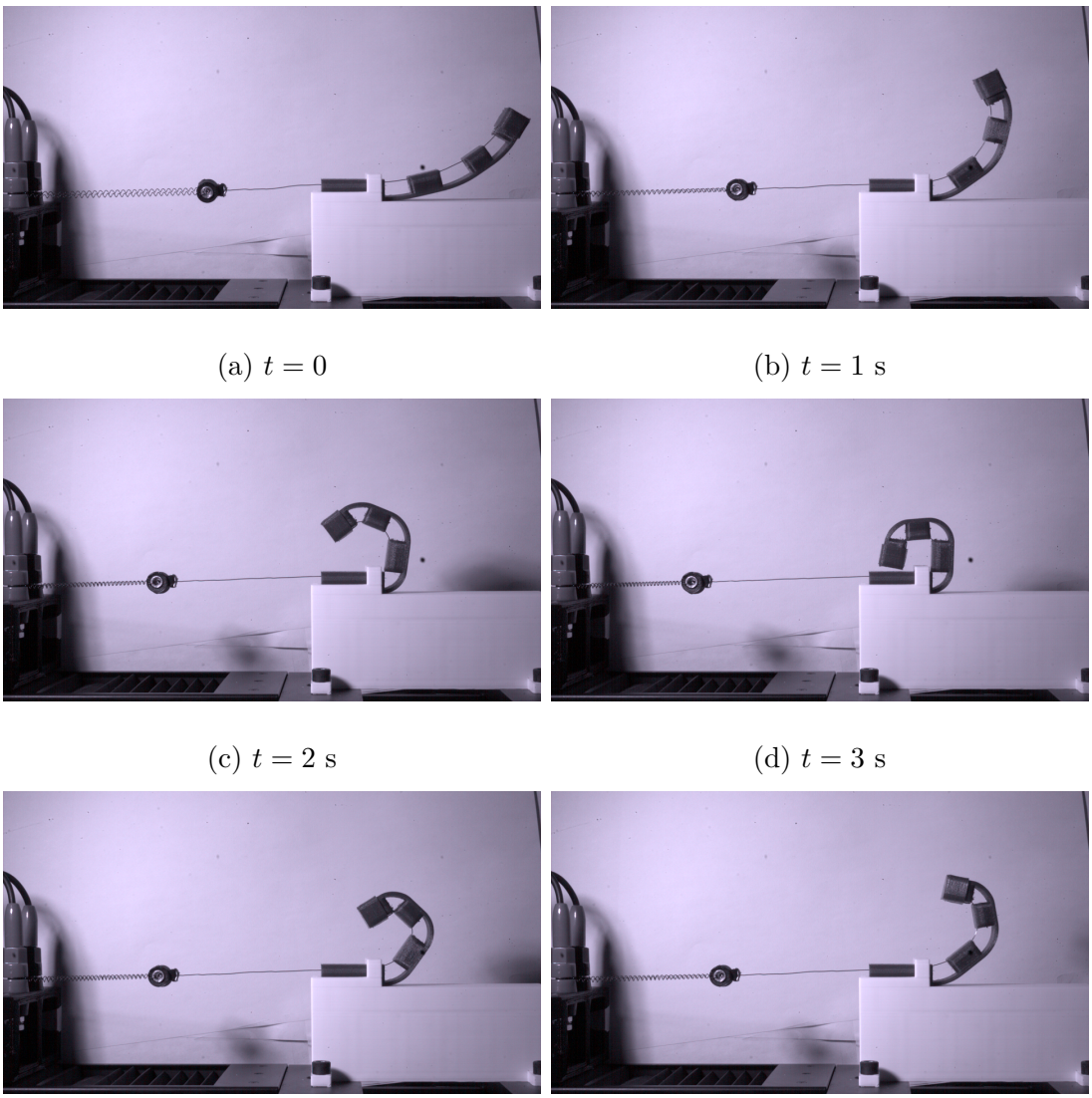

(a) $t = 0$ (b) $t = 1$ s

(c) $t = 2$ s (d) $t = 3$ s

(e) $t = 21.8$ s (f) $t = 42$ s

Fig. 5.5 Time lapse images of the SMA coil actuating the finger

As shown in the motion tracking for the SMA in Figure 5.4(b), there is a very slight bias motion after actuation as the joint forces pull against the SMA. The compliant mechanism is held like this for about 7 seconds, before the joint forces become dominant at $t = 11.10$ seconds and the rate of bias motion increases. This indicates that the SMA takes about 8 seconds after current conduction to cool from convective heat transfer enough for the phase change from austenite to martensite to begin. The biasing motion begins at an approximately linear rate, with a maximum bias speed of 0.74 mm/s. This linear region occurs for about 15 seconds before levelling off asymptotically. The decrease in bias speed indicates the system is approaching an equilibrium point between the force-displacement profiles of the martensite coil and antagonist structure.

The compliant joints bias the SMA from a displacement of $\delta = 45.51$ mm to $\delta = 60.68$mm, indicating a bias distance of 15.17 mm. The relatively short bias distance indicate that the force-displacement profile of the finger is not dominant over the martensite coil for a large region. This asymmetry in the finger F-D profile is likely due to energy loss in the compliant joints, as shown in Figure 5.1(a). The measured bias distance does not completely reset the mechanism after the actuation stroke, but it does exceed the predicted bias distance at point C in Figure 5.1(b).

The experimental results showed a total heating-cooling period of 11.35 seconds. The 8 second cooling time is an indication that the temperature of the SMA greatly

exceeded the austenite finish temperature of the material. This passive cooling by convection can be expedited by shaping the current input or introducing temperature feedback, to minimize temperature saturation. This would allow for a much faster transition to the return phase.

The results of the integration test match very closely with the predictions from the dynamics simulations and the hysteresis matching. The video footage shows that the flexure joints still have some room for greater bending, which indicates that the end effector is held in equilibrium due to the joint stiffness rather than from physical contact. This confirms the results from the Chapter 2 experiments, where it was shown that this flexure design method enables stiffness matching for a known actuator. This also validates the SMA coil design and characterization, as the hysteresis matching correctly predicted that the SMA austenite force would drop to 13 N at a displacement of 45.5 mm.

6 Conclusions and Future Work

In this work, the engineering design process to match a compliant antagonist structure to an SMA coil actuator was presented in order to create a robotic finger. The use of flexible joints allows for the structure of the mechanism to bias the SMA actuators, eliminating the need for external bias assemblies. This is accomplished by design and characterization of both the actuator and the structure to achieve equilibrium at the desired SMA stroke lengths. This principle is applied to the design, manufacturing, and testing of a compliant finger gripper with an SMA coil acting as an artificial muscle.

Through use of a static wrench analysis on the pseudo-rigid body model, a relationship between flexure geometry and pseudo-rigid joint torques was established. This allowed for calculation of the flexure geometry required to match the desired actuator load to the mechanism pose. The stiffness based design of the beam flexures were verified through linear displacement tests.

Characterization of the actuator and compliant structure allowed for a hysteresis

matched final design. By measuring the F-D relationships of the SMA coil in austenite and martensite phases, the finger was re-designed to establish equilibrium points at desired positions in the actuation cycle. The derivation of a dynamic model for both the actuator and mechanism also allowed for better prediction of integrated behaviour.

The experimental results in Chapter 5 showed the successful integration of an SMA coil actuator with the 3D-printed compliant robotic finger. The SMA austenite force balances with the flexible joint stiffnesses such that the mechanism reaches equilibrium near the designed-for grip pose. Upon cooling to martensite, the stored elastic energy in the antagonist joints are able to partially bias the SMA coil. Due to energy loss in the joints, the bias distance does not completely recover the actuation stroke.

6.1 Future Work

As seen in the integrated tests, the entire actuation stroke is not recovered by the antagonists. This is likely due to energy loss in the flexure material, which in this work was a commercial thermoplastic polyurethane 3D printer filament. The antagonist bias distance can be improved by selecting a different material for the compliant structure, ideally one with better elastic energy storage or less hysteresis behaviour.

Another path for future work is temperature control of the SMA. As shown in the dynamic simulations, the temperature of the SMA is likely greatly exceeding the austenite finish temperature. This thermal saturation increases the time it takes for the coil to cool down to martensite. This limits the actuation frequency of the SMA. It may be possible to use the characterization data and dynamics simulations to better shape the input for quick heating to the austenite finish temperature and holding it there, or to introduce temperature sensors for feedback control.

The mechanism in this work is a single finger, but this can easily be expanded into a multi-digit gripper. The compliant antagonist design method presented in Chapter 2 can be applied to multiple digits with different load and pose requirements to produce the design of a more complex gripper. This can be an underactuated mechanism, only requiring one SMA coil per digit. Refinement of the design could also allow for better integration of the SMAs and compliant antagonists to better replicate human muscle characteristics. It would also be interesting to introduce haptic sensors, possibly with conductive pads on the digit end-effectors to determine contact conditions. This could contribute to the development of a more anthropomorphic prosthetic hand, with SMAs acting as artificial muscle, with similar behaviour to that of a human hand.

A Complete List of Publications

Conference Papers

[1] **A. Tangestanian**, R. Orszulik "Compliant Robotic Finger Design for One-Way Linear Actuators," *IEEE/ASME International Conference on Advanced Intelligent Mechatronics*, pp 132-137. DOI : 10.1109/AIM52237.2022.9863264 Sapporo, Japan. July 11-15, 2022.

Conference Abstracts

[1] **A. Tangestanian**, R. Orszulik "Mechanical Design of a 3D-Printed Robotic Finger with Compliant Joints," *Canadian Society of Mechanical Engineering Congress*. Edmonton, Canada. June 6-8, 2022.

Bibliography

[1] Flexinol, *Technical Characteristics of Flexinol Actuator Wires*, Dynalloy Incorporated, https://www.dynalloy.com/pdfs/TCF1140.pdf, revision j ed., 2022, Commercial product specifications.

[2] An, S.-M., Ryu, J., Cho, M., and Cho, K.-J., "Engineering design framework for a shape memory alloy coil spring actuator using a static two-state model," *Smart Materials and Structures*, Vol. 21, No. 5, April 2012, pp. 055009.

[3] Jani, J., Leary, M., Subic, A., and Gibson, M., "A review of shape memory alloy research, applications and opportunities," *Materials & Design*, Vol. 56, 04 2014, pp. 1078–1113.

[4] Price, A. D., Jnifene, A., and Naguib, H. E., "Design and control of a shape memory alloy based dexterous robot hand," *Smart Materials and Structures*, Vol. 16, No. 4, jul 2007, pp. 1401–1414.

[5] Farias, V., Solis, L., Melendez, L., Garcia, C., and Velazquez, R., "A four-fingered robot hand with shape memory alloys," *AFRICON 2009*, 2009, pp. 1–6.

[6] Andrianesis, K., Koveos, Y., Nikolakopoulos, G., and Tzes, A., *Shape memory alloys*, chap. Experimental Study of a Shape Memory Alloy Actuation System for a Novel Prosthetic Hand, IntechOpen, Oct. 2010, pp. 81–106.

[7] Soriano-Heras, E., Blaya-Haro, F., Molino, C., and de Agustín del Burgo, J. M., "Rapid prototyping prosthetic hand acting by a low-cost shape-memory-alloy actuator," *Journal of Artificial Organs*, Vol. 21, No. 2, 2018, pp. 238–246.

[8] Deng, E. and Tadesse, Y., "A Soft 3D-Printed Robotic Hand Actuated by Coiled SMA," *Actuators*, Vol. 10, No. 1, 2021, pp. 1–24.

[9] Tanaka, K. and Nagaki, S., "A thermomechanical description of materials with internal variables in the process of phase transitions," *Ingenieur-Archiv*, Vol. 51, No. 5, 1982, pp. 287–299.

[10] Liang, C. and Rogers, C. A., "One-Dimensional Thermomechanical Constitutive Relations for Shape Memory Materials," *Journal of Intelligent Material Systems and Structures*, Vol. 8, No. 4, April 1997, pp. 285–302.

[11] Koh, J.-S., "Design Of Shape Memory Alloy Coil Spring Actuator For Improving Performance In Cyclic Actuation," *Materials*, Vol. 11, No. 232, 2018.

[12] Cortez-Vega, R., Chairez, I., Luviano-Juárez, A., and Feliu-Batlle, V., "A hybrid dynamic model of shape memory alloy spring actuators," *Measurement*, Vol. 114, 2018, pp. 340–353.

[13] Kolyvas, E. and Tzes, A., "Model based design of antagonistic shape memory alloy spring devices," *Journal of Intelligent Material Systems and Structures*, Vol. 29, No. 12, 2018, pp. 2619–2640.

[14] Ma, J., Huang, H., and Huang, J., "Characteristics Analysis And Testing Of SMA Spring Actuator," *Advances in Materials Science and Engineering*, 2013.

[15] Price, A., Edgerton, A., Cocaud, C., Naguib, H., and Jnifene, A., "A study on the thermomechanical properties of shape memory alloys-based actuators used in artificial muscles," *Journal of Intelligent Material Systems and Structures*, Vol. 18, No. 1, 2007.

[16] Uehara, T., *Shape memory alloys*, chap. Molecular dynamics simulation of shape-memory behavior, IntechOpen, Rijeka, 2010.

[17] Lobo, P., Almeida, J., and Guerreiro, L., "Shape memory alloys behaviour: a review," *Procedia Engineering*, Vol. 114, 2015, pp. 776–783, ICSI 2015 The 1st International Conference on Structural Integrity Funchal, Madeira, Portugal 1st to 4th September, 2015.

[18] Van Humbeeck, J., "Shape memory alloys: a material and a technology," *Advanced Engineering Materials*, Vol. 3, No. 11, 2001, pp. 837–850.

[19] Hartl, D. J. and Lagoudas, D. C., "Aerospace applications of shape memory alloys," *Proceedings of the Institution of Mechanical Engineers, Part G: Journal of Aerospace Engineering*, Vol. 221, No. 4, 2007, pp. 535–552.

[20] Ölander, A., "An electrochemical investigation of solid cadmium-gold alloys," *J. Am. Chem. Soc.*, Vol. 54, No. 10, Oct. 1932, pp. 3819–3833.

[21] Kauffman, G. B. and Iaac, M., "The story of nitinol: the serendipitous discovery of the memory metal and its applications," *The Chemical Educator*, Vol. 2, No. 2, 1997, pp. 1–21.

[22] Schetky, L. M., "Shape-memory alloys," *Scientific American*, Vol. 241, No. 5, 1979, pp. 74–83.

[23] Kopa, R., "Efficiency of energy conversion in nitinol," *Proceedings of the NITINOL Heat Engine Conference*, edited by D. M. Goldstein and L. J. Mc-

Namara, Vol. 9, U.S Department of Energy and U.S Naval Surface Weapons Center, Silver Spring, Maryland, Sept. 1978, pp. 1–56.

[24] Wang, F. E., "The thermobile nitinol engine," *SAE Transactions*, Vol. 94, 1985, pp. 577–585.

[25] Sandoval, D. J., "Nitinol belt engine," *Proceedings of the NITINOL Heat Engine Conference*, edited by D. M. Goldstein and L. J. McNamara, Vol. 3, U.S Department of Energy and U.S Naval Surface Weapons Center, Silver Spring, Maryland, Sept. 1978, pp. 1–8.

[26] Kauffman, G. B. and Mayo, I., "The thermobile (tm): a nitinol-based scientific toy," *Journal of Chemical Education*, Vol. 75, No. 3, March 1998, pp. 313.

[27] Dixon, J., "Introduction and foreword," *Proceedings of the NITINOL Heat Engine Conference*, edited by D. M. Goldstein and L. J. McNamara, Vol. 0, U.S Department of Energy and U.S Naval Surface Weapons Center, Silver Spring, Maryland, Sept. 1978, pp. 1–4.

[28] Machado, L. G. and Savi, M. A., "Medical Applications of Shape Memory Alloys," *Brazilian Journal of Medical and Biological Research*, Vol. 36, June 2003, pp. 683–691.

[29] Hiltz, J. A., "Shape Memory Polymers. Literature Review," techreport DRDC-ATLANTIC-TM-2002-127, Defence R and D Canada, Aug. 2002.

[30] Kim, I. S., *Dynamics Modelling And Control System Design For Shape Memory Alloy Actuators*, Master's thesis, York University, 2014.

[31] Song, G., Ma, N., and Li, H.-N., "Applications of shape memory alloys in civil structures," *Engineering Structures*, Vol. 28, No. 9, 2006, pp. 1266–1274.

[32] Matsunaga, T., Totsu, K., Esashi, M., and Haga, Y., "Tactile display using shape memory alloy micro-coil actuator and magnetic latch mechanism," *Displays*, Vol. 34, No. 2, 2013, pp. 89–94.

[33] Mohamed Ali, M. S., Bycraft, B., Bsoul, A., and Takahata, K., "Radio-controlled microactuator based on shape-memory-alloy spiral-coil inductor," *Journal of Microelectromechanical Systems*, Vol. 22, 04 2013, pp. 331–338.

[34] Yousefi-Koma, A., Pouriayevali, H., and Jokar, M., "Design And Fabrication Of A Novel SMA Spring Actuated 2DOF Orientating Mechanism," *3rd International Conference on Robotics and Mechatronics*, 2017.

[35] Alcaide, J. O., Pearson, L., and Rentschler, M. E., "Design, modeling and control of a SMA-actuated biomimetic robot with novel functional skin," *2017*

IEEE International Conference on Robotics and Automation (ICRA), 2017, pp. 4338–4345.

[36] Kim, S., Hawkes, E., Choy, K., Joldaz, M., Foleyz, J., and Wood, R., "Micro artificial muscle fiber using NiTi spring for soft robotics," *2009 IEEE/RSJ International Conference on Intelligent Robots and Systems, IROS 2009*, Nov. 2009, pp. 2228–2234.

[37] Wang, Z., Zu, X., Fu, P., Dai, J., Zhu, S., and Wang, L., "Two-way shape memory effect of TiNi alloy coil extension springs," *Materials Science and Engineering A: Structural Materials Properties Microstructure and Processing*, Vol. 360, Nov. 2003, pp. 126–131.

[38] Noh, M., Kim, S.-W., An, S., Koh, J.-S., and Cho, K.-J., "Flea-inspired catapult mechanism for miniature jumping robots," *IEEE Transactions on Robotics*, Vol. 28, No. 5, 2012.

[39] Kim, H., Han, Y., Lee, D., Ha, J., and Cho, K., "Sensorless displacement estimation of a shape memory alloy coil spring actuator using inductance," *Smart Materials and Structures*, Vol. 22, No. 2, Dec. 2012.

[40] Heidari, B., Kadkhodaei, M., Barati, M., and Karimzadeh, F., "Fabrication and modeling of shape memory alloy springs," *Smart Materials and Structures*, Vol. 25, No. 12, Nov. 2016, pp. 125003.

[41] Naggar, A. and Youssef, M., "Shape Memory Alloy Heat Activation: State of the Art Review," *AIMS Materials Science*, Vol. 7, No. 6, 2020, pp. 836–858.

[42] Sun, Q. P. and Hwang, K. C., "Micromechanics modelling for the constitutive behavior of polycrystalline shape memory alloys. I. Derivation of general relations," *Journal of the Mechanics and Physics of Solids*, Vol. 41, No. 1, Jan. 1993, pp. 1–17.

[43] Grandi, D., Maraldi, M., and Molari, L., "A macroscale phase-field model for shape memory alloys with non-isothermal effects: Influence of strain rate and environmental conditions on the mechanical response," *Acta Materialia*, Vol. 60, No. 1, Jan. 2012, pp. 179–191.

[44] Bundhoo, V., *Design and evaluation of a shape memory alloy-based tendon driven actuation system for biomimetic artificial fingers*, Master's thesis, University of Victoria, 2009.

[45] Koh, J.-S., Lee, D.-Y., and Cho, K.-J., "Design Of The Shape Memory Alloy Coil Spring Actuator For The Soft Deformable Wheel Robot," *9th International Conference on Ubiquitous Robots and Ambient Intelligence (URAI)*, 2012.

[46] Sreekumar, M., Nagarajan, T., Singaperumal, M., Zoppi, M., and Molfino, R., "Critical review of current trends in shape memory alloy actuators for intelligent robots," *The Industrial Robot*, Vol. 34, No. 4, 2007, pp. 285–294.

[47] Copaci, D., Blanco, D., and Moreno, L., "Flexible shape-memory alloy-based actuator: mechanical design optimization according to application," *Actuators*, Vol. 8, No. 63, July 2019.

[48] Hughes, D. and Wen, J. T., "Preisach modeling of piezoceramic and shape memory alloy hysteresis," *Smart Materials and Structures*, Vol. 6, No. 3, June 1997, pp. 287–300.

[49] Tobushi, H., Takata, K., Shimeno, Y., Nowacki, W. K., and Gadaj, S. P., "Influence of strain rate on superelastic behaviour of TiNi shape memory alloy," *Proceedings of the Institution of Mechanical Engineers, Part L: Journal of Materials: Design and Applications*, Vol. 213, No. 2, April 1999, pp. 93–102.

[50] Lagoudas, D. C., Mayes, J. J., and Khan, M. M., "Simplified shape memory alloy (SMA) material model for vibration isolation," *Smart Structures and Materials 2001: Modeling, Signal Processing, and Control in Smart Structures*, edited by V. S. Rao, Vol. 4326, International Society for Optics and Photonics, SPIE, 2001, pp. 452–461.

[51] Seelecke, S. and Muller, I., "Shape memory alloy actuators in smart structures: Modeling and simulation," *Applied Mechanics Reviews*, Vol. 57, No. 1, jan 2004, pp. 23–46.

[52] Nakayama, H., Zhao, Y., Taya, M., Chen, W., Urushiyama, Y., and Suzuki, S., "Strain-rate effects on TiNi and TiNiCu shape memory alloys," *Proceedings of SPIE - The International Society for Optical Engineering*, Vol. 5761, 05 2005.

[53] Teh, Y. and Featherstone, R., "An Architecture for Fast and Accurate Control of Shape Memory Alloy Actuators," *The International Journal of Robotics Research*, Vol. 27, No. 5, May 2008, pp. 595–611.

[54] Yoo, Y. I. and Lee, J. J., "Two-way Shape Memory Effect of NiTi under Compressive Loading Cycles," *Physics Procedia*, Vol. 22, 2011, pp. 449–454, 2011 International Conference on Physics Science and Technology (ICPST 2011).

[55] Sittner, P., Heller, L., Pilch, J., Curfs, C., Alonso, T., and Favier, D., "Young's Modulus of Austenite and Martensite Phases in Superelastic NiTi Wires," *Journal of Materials Engineering and Performance*, Vol. 23, No. 7, April 2014, pp. 2303–2314.

[56] Velmurugan, C., Senthilkumar, V., Dinesh, S., and Arulkirubakaran, D., "Review on phase transformation behavior of NiTi shape memory alloys," *Materials Today: Proceedings*, Vol. 5, No. 6, Part 2, 2018, pp. 14597–14606, International Conference on Advanced Functional Materials 2017 (ICAFM'17), 03.05.2017 – 05.05.2017.

[57] Teh, Y. and Featherstone, R., "A new control system for fast motion control of sma actuator wires," *Shape Memory And Related Technologies (SMART 2004)*, Vol. 1, University of Singapore, 01 2004, pp. 1–13.

[58] Guo, Z., Yu, H., and Wee, L.-B., "Design of a novel compliant differential Shape Memory Alloy actuator," *2013 IEEE/RSJ International Conference on Intelligent Robots and Systems*, 2013, pp. 4925–4930.

[59] Ranjith Pillai, R., Murali, G., and Gopal, M., "Modeling and simulation of a shape memory alloy spring actuated flexible parallel manipulator," *Procedia Computer Science*, Vol. 133, 2018, pp. 895–904, International Conference on Robotics and Smart Manufacturing (RoSMa2018).

[60] Lopes, L., Cunha, M., Basílio Sobrinho, J., Souto, C., Ries, A., Bezerra, J. I., and Macêdo, E., "Electronic instrumentation for shape memory alloy actuators," 12 2020.

[61] Olender, A., *Strain Rate Effects on the Behavior of Shape Memory Alloys*, mathesis, Massachusetts Institute of Technology, June 2013.

[62] Tai, N. T., Kha, N. B., and Ahn, K. K., "Predictive position and force control for shape memory alloy cylinders," *Journal of Mechanical Science and Technology*, Vol. 24, No. 8, Aug. 2010, pp. 1717–1728.

[63] Coral, W., Rossi, C., Colorado, J., Lemus, D., and Barrientos, A., "Sma-based muscle-like actuation in biologically inspired robots: a state of the art review," *Smart Actuation and Sensing Systems*, edited by G. Berselli, R. Vertechy, and G. Vassura, chap. 3, IntechOpen, Rijeka, 2012.

[64] Rosario, M. V., Sutton, G. P., Patek, S. N., and Sawicki, G. S., "Muscle–spring dynamics in time-limited, elastic movements," *Proceedings of the Royal Society B: Biological Sciences*, Vol. 283, No. 1838, sep 2016, pp. 20161561.

[65] Trimmer, B., Takesian, A., Sweet, B., Rogers, C., Hake, D., and Rogers, D., "Caterpillar locomotion: A new model for soft-bodied climbing and burrowing robots," *Proceedings of the 7th International Symposium on Technology and the Mine Problem*, 04 2006.

[66] Koh, J.-S. and Cho, K.-J., "Omega-shaped inchworm-inspired crawling robot with large-index-and-pitch (lip) sma spring actuators," *IEEE/ASME Transactions On Mechatronics*, Vol. 18, No. 2, 2013.

[67] Koh, J.-S., Yang, E., Jung, G.-P., Jung, S.-P., Son, J. H., Lee, S.-I., Jablonski, P. G., Wood, R. J., Kim, H.-Y., and Cho, K.-J., "Jumping on water: Surface tension–dominated jumping of water striders and robotic insects," *Science*, Vol. 349, No. 6247, 2015, pp. 517–521.

[68] Nakano, Y., Fujie, M., and Hosada, Y., "Hitachi's robot hand," *Robotics Age*, Vol. 6, No. 7, July 1984, pp. 18–20.

[69] De Laurentis, K. J. and Mavroidis, C., "Mechanical design of a shape memory alloy actuated prosthetic hand." *Technology and health care : official journal of the European Society for Engineering and Medicine*, Vol. 10, 2002, pp. 91–106.

[70] Belter, J. T. and Dollar, A., "Performance characteristics of anthropomorphic prosthetic hands," *2011 IEEE International Conference on Rehabilitation Robotics*, 2011, pp. 1–7.

[71] Kyberd, P. J., Clawson, A., and Jones, B., "The use of underactuation in prosthetic grasping," *Mechanical Sciences*, Vol. 2, No. 1, 2011, pp. 27–32.

[72] Belter, J. T., Segil, J. L., Dollar, A. M., and Weir, R. F., "Mechanical design and performance specifications of anthropomorphic prosthetic hands: a review," *Journal of Rehabilitation Research and Development*, Vol. 50, No. 5, 2013, pp. 599+.

[73] Basumatary, H. and Hazarika, S. M., "State of the Art in Bionic Hands," *IEEE Transactions on Human-Machine Systems*, Vol. 50, No. 2, 2020, pp. 116–130.

[74] Kaplanoglu, E., "Design of shape memory alloy-based and tendon-driven actuated fingers towards a hybrid anthropomorphic prosthetic hand," *International Journal of Advanced Robotic Systems*, Vol. 9, No. 3, 2012.

[75] Lee, J. H., Okamoto, S., and Matsubara, S., "Development of multi-fingered prosthetic hand using shape memory alloy type artificial muscle," *Proceedings of the International MultiConference of Engineers and Computer Scientists IMECS2012*, Vol. 2, March 2012.

[76] Silva, A. F. C., dos Santos, A. J. V., Souto, C. d. R., de Araújo, C. J., and da Silva, S. A., "Artificial Biometric Finger Driven by Shape-Memory Alloy Wires," *Artificial Organs*, Vol. 37, No. 11, 2013, pp. 965–972.

[77] Simone, F., Borreggine, S., Rizzello, G., Palmisano, V., Naso, D., and Selecke, S., "Modeling and Identification of a Shape Memory Alloy Robotic Finger Actuator," 06 2019.

[78] Howell, L. L., *Compliant Mechanisms*, John Wiley and Sons Inc., 2001.

[79] Lobontiu, N., *Compliant mechanisms design of flexure hinges*, CRC Press, 2003.

[80] Linß, S., Henning, S., and Zentner, L., *Kinematics Analysis and Applications*, chap. Modeling and design of flexure hinge-based compliant mechanisms, In-TechOpen, 04 2019.

[81] Ling, M., Howell, L. L., Cao, J., and Chen, G., "Kinetostatic and dynamic modeling of flexure-based compliant mechanisms: a survey," *Appl. Mech. Rev*, Vol. 72, No. 3, Jan. 2020.

[82] Gul, J., Sajid, M., Rehman, M., Siddiqui, G. Shah, I., Kim, K., Lee, J., and Choi, K., "3D printing for soft robotics – a review," *Science and Technology of Advanced Materials*, Vol. 19, No. 1, 2018, pp. 243–262.

[83] Šalinić, S. and Nikolić, A., "A new pseudo-rigid-body model approach for modeling the quasi-static response of planar flexure-hinge mechanisms," *Mechanism and Machine Theory*, Vol. 124, 2018, pp. 150 – 161.

[84] Meng, Q., *A design method for flexure-based compliant mechanisms on the basis of stiffness and stress characteristics*, Ph.D. thesis, University of Bologna, 2012.

[85] Pei, X., Yu, J., Zong, G., and Bi, S., "Design of compliant straight-line mechanisms using flexural joints," *Chinese Journal of Mechanical Engineering*, Vol. 27, No. 1, 2014, pp. 146–153.

[86] Zhu, Z., Zhou, X., Wang, R., and Liu, Q., "A simple compliance modeling method for flexure hinges," *Science China Technological Sciences*, Vol. 58, No. 1, 2015, pp. 56–63.

[87] Ivanov, I. and Corves, B., "Stiffness-oriented design of a flexure hinge-based parallel manipulator," *Mechanics Based Design of Structures and Machines*, Vol. 42, No. 3, 2014, pp. 326–342.

[88] Ling, M., Cao, J., and Pehrson, N., "Kinetostatic and dynamic analyses of planar compliant mechanisms via a two-port dynamic stiffness model," *Precision Engineering*, Vol. 57, 2019, pp. 149 – 161.

[89] Mengacci, R., Zambella, G., Grioli, G., Caporale, D., Catalano, M. G., and Bicchi, A., "An Open-Source ROS-Gazebo Toolbox for Simulating Robots With Compliant Actuators," *Frontiers in Robotics and AI*, Vol. 8, 2021, pp. 246.

[90] Su, H.-J., "A Pseudorigid-Body 3R Model for Determining Large Deflection of Cantilever Beams Subject to Tip Loads," *Journal of Mechanisms and Robotics*, Vol. 1, No. 2, 01 2009, 021008.

[91] Lotti, F. and Vassura, G., "A novel approach to mechanical design of articulated fingers for robotic hands," *2002 IEEE/RSJ International Conference on Intelligent Robots and Systems (IROS)*, Vol. 2, Feb. 2002, pp. 1687–1692.

[92] Mutlu, R., Alici, G., Panhuis, M., and Spinks, G. M., "3D Printed Flexure Hinges for Soft Monolithic Prosthetic Fingers," *Soft Robotics*, Vol. 3, No. 3, 2016, pp. 120–133.

[93] Liu, C.-H., Chiu, C.-H., Chen, T.-L., Pai, T.-Y., Chen, Y., and Hsu, M.-C., "A Soft Robotic Gripper Module with 3D Printed Compliant Fingers for Grasping Fruits," *2018 IEEE/ASME International Conference on Advanced Intelligent Mechatronics (AIM)*, 2018, pp. 736–741.

[94] El-Sheikh, M. A., "Fibonacci-Compliant Finger Design," *The International Journal of Artificial Organs*, Vol. 39, No. 9, 2016, pp. 491–496, PMID: 27768205.

[95] Zhang, Y., Zhan, Q., Li, R., and Bao, X., "Design, Fabrication and Experiments of an Anthropomorphic Finger with Combined Compliant Joints," *Journal of Bionic Engineering*, Vol. 17, No. 6, 2020, pp. 1152–1162.

[96] Mohammadi, A., Lavranos, J., Zhou, H., Mutlu, R., Alici, G., Tan, Y., Chong, P., and Oetomo, D., "A practical 3d-printed soft robotic prosthetic hand with multi-articulating capabilities," *PLoS One*, Vol. 15, No. 5, May 2020.

[97] Grossard, M., Martin, J., and Huard, B., "Force-sensing actuator with a compliant flexure-type joint for a robotic manipulator," *Actuators*, Vol. 4, No. 4, 2015, pp. 281–300.

[98] Garcia, L., Naves, M., and Brouwer, D. M., "3D-printed flexure-based finger joints for anthropomorphic hands," *2018 IEEE/RSJ International Conference on Intelligent Robots and Systems (IROS)*, 2018, pp. 1437–1442.

[99] Zhou, H., Tawk, C., and Alici, G., "A 3D Printed Soft Prosthetic Hand with Embedded Actuation and Soft Sensing Capabilities for Directly and Seamlessly Switching Between Various Hand Gestures," *2021 IEEE/ASME International Conference on Advanced Intelligent Mechatronics (AIM)*, 2021, pp. 75–80.

[100] Duffy, J., *Statics and Kinematics with Applications to Robotics*, chap. A Displacement Analysis of Planar Robot Manipulators, Cambridge University Press, 1996, pp. 24–27.

[101] Waldron, K. and Schmiedeler, J., *Springer Handbook of Robotics*, chap. Kinematics, Springer Berlin Heidelberg, 2008, pp. 9–33.

[102] Ultimaker, *Technical data sheet 95A*, Ultimaker, Nov. 2018, Version 4.002.

[103] Muller, I., "A Model for a Body With Shape-Memory," *Archive for Rational Mechanics and Analysis*, Vol. 70, No. 1, mar 1979, pp. 61–77.

[104] Fischer, F. D. and Tanaka, K., "A micromechanical model for the kinetics of martensitic transformation," *International Journal of Solids and Structures*, Vol. 29, No. 14-15, 1992, pp. 1723–1728.

[105] Li, J. and Harada, H., "Modeling of an SMA actuator based on the Liang and Rogers model," *International Journal of Applied Electromagnetics and Mechanics*, Vol. 43, No. 4, 2013, pp. 323–335.

[106] L. Miková and S. Medvecká-Beňová and M. Kelemen and F. Trebuňa and I. Virgala, "Application of Shape Memory Alloy (SMA) as Actuator," *Metalurgija*, Vol. 54, No. 1, 2015, pp. 169–172.

[107] Kim, S.-W., Lee, J.-G., An, S., Cho, M., and Cho, K.-J., "A large-stroke shape memory alloy spring actuator using double-coil configuration," *Smart Materials and Structures*, Vol. 24, No. 9, Aug. 2015, pp. 095014.

[108] Khan, H., Manfredi, L., Huan, Y., Velsink, F., and Cuschieri, A., "Analysis Of Performance And Energy Efficiency Of Thin Shape Memory Alloy Wire-based Actuators," *ACTUATOR*, Vol. 15, June 2016, pp. 321–325.

[109] Islam, A. B. M. R. and Karadoğan, E., "Sensitivity and Uncertainty Analysis of One-Dimensional Tanaka and Liang-Rogers Shape Memory Alloy Constitutive Models," *Materials*, Vol. 12, No. 10, May 2019.

[110] Featherstone, R. and Orin, D., *Springer Handbook of Robotics*, chap. Dynamics, Springer Berlin Heidelberg, 2008, pp. 35–65.